TECHNISCHE UNIVERSITÄT MÜNCHEN

MAX-PLANCK-INSTITUT
FÜR
ASTROPHYSIK

Neutrinos from the Formation, Cooling and Black Hole Collapse of Neutron Stars

Lorenz Hüdepohl

Vollständiger Abdruck der an die Fakultät für Physik der Technischen Universität München zur Erlangung des akademischen Grades eines

Doktors der Naturwissenschaften (Dr. rer. nat.)

genehmigten Dissertation.

Vorsitzende:		Univ.-Prof. Dr. Laura Fabbietti
Prüfer der Dissertation:	1.	Priv.-Doz. Dr. Hans-Thomas Janka
	2.	Univ.-Prof. Dr. Alejandro Ibarra

Die Dissertation wurde am 29.10.2013 bei der Technischen Universität München eingereicht und durch die Fakultät für Physik am 03.02.2014 angenommen.

Contents

1 Introduction

Neutron stars are born when massive stars die. This thesis is about the first ten seconds in the life of newborn neutron stars and the signals we can hope to receive from them in the form of neutrinos.

During the regular star's life before, it has burnt more and more of its initial hydrogen to helium, carbon, neon, oxygen and silicon until it finally has to resort to produce iron group elements. These elements constitute the maximum of the nuclear binding energy per baryon and no further energy can be released by combining them into even heavier nuclei.

That iron group "ash" of the nuclear burning accumulates in a dense core of about a solar mass of matter compressed into a sphere of roughly 1000km in radius and is mostly supported against its own gravity by electron degeneracy pressure. However, there is only so much mass this pressure is able to support. There exists a limit, the famous Chandrasekhar mass, above which gravity starts to dominate and the inner iron core abruptly starts to collapse within fractions of a second. This is initiated by an increasing rate of electron captures as the central density rises, robbing the core of degeneracy pressure, as well as photo dissociation of heavy nuclei which consumes thermal energy.

As the matter is compressed to higher and higher densities, copious amounts of electron neutrinos are generated as more and more electrons are captured by heavy nuclei and protons to form neutron rich nuclei and neutrons. At some point, for densities exceeding $10^{11-12}\,\mathrm{g/cm^3}$, however, the matter becomes opaque even for neutrinos with their minuscule interaction cross sections and thus this energy sink is closed. The collapse then proceeds adiabatically, carrying the neutrinos with it.

Finally, as the densities approach those found in atomic nuclei, also the short-ranged, repulsive nuclear forces become relevant. This additional pressure contribution results in an abrupt stiffening of the equation of state, abruptly halting the collapse. Simultaneously, the remaining heavy nuclei are decomposed into individual nucleons in very close proximity and a burst of electron neutrinos with tremendous power is emitted – signalling that in this moment a (proto) neutron star was born.

Inertia results in a slight overcompression above the new equilibrium configuration and for a brief moment the compact object in the centre even expands outwards. Meanwhile matter from the outside is still radially falling into the centre with supersonic velocities – a shock wave forms. As the infalling matter passes this front, it gets decelerated and compressed, and is fully decomposed into neutrons, protons, and α-particles. Then, in a comparably slow, subsonic flow it settles onto the proto neutron star. Meanwhile, the tremendous amounts of neutrinos trapped in the dense interior of the proto neutron star slowly diffuse out and radiate from its surface. On their way out, they can deposit some of their energy in the thick accretion layer above. It is this effect, the delayed neutrino heating mechanism, that is thought to be responsible to finally explode the outer hull of the star.

It becomes evident that core-collapse supernovae are a wonderful physics playground. Every one of the four known forces is a vitally important ingredient that has to be considered in this scenario. The electromagnetic forces determine the behaviour of the ionized plasma of the star. Hours to days later, these will also be responsible for the optically visible signal in the astronomers' telescopes, when the explosion reaches the surface of the star. Gravity is both the merciless driver of the collapse and the energy source for the vast amount of energy radiated by neutrinos, as the huge binding energy in the formation of the compact remnant gets released. The weak force governs the creation and interaction of the neutrinos with the matter and each other. And finally, the strong force enters in the form of the nuclear physics that describes the equation of state of matter in the proto neutron star, which has densities comparable and exceeding those of individual atomic nuclei.

This basic picture of the gravitational core-collapse was refined over almost a century. Already shortly after the discovery of the neutron by Chadwick (1932), it was suggested by Baade and Zwicky (1934) that supernovae are connected to the formation of a neutron star out of the remains of a dying ordinary star. Decades later, observations by Hewish et al. (1968) could indeed identify a pulsating radio source – a "pulsar" – in the Crab nebula, that had previously been identified as the site of the supernova of the year 1054.

Colgate and White (1966) highlighted the important role of neutrinos in the core-collapse scenario and were the first to propose that energy deposition by neutrinos is the driver behind the explosion. Calculations by Wilson (1982) showed that this scenario might work, albeit not in a prompt fashion. The neutrino irradiation took some couple of hundred milliseconds of continued accretion onto the proto neutron star until the conditions for a run-away ejection of the outer hull were found. However, for that mechanism to work it was necessary to assume a very efficient energy transport by so-called neutron-finger convection within the proto neutron star in order to boost the neutrino luminosities sufficiently.

Then, in 1987 a star in the Large Magellanic Cloud, in our direct galactic neighbourhood, exploded in a spectacular supernova. Not only was this a unique opportunity for optical astronomers, but the largest neutrino detectors operating at the time could even detect a number of events corresponding to the expected intense neutrino burst from the supernova. The Kamiokande-II experiment in Japan detected eleven, the Irvine–Michigan–Brookhaven detector in the US eight, and the Baksan Neutrino Observatory in Russia detected five neutrino events, all within a burst lasting less than 13 seconds[1].

---

[1] The Mont Blanc liquid scintillator experiment also detected a burst of five neutrino events about five hours earlier, which would be puzzling for the standard core-collapse picture, that

This firmly established a connection between neutrinos and core-collapse events. It is expected that a supernova within our galaxy would be registered as tens of thousands of events in current neutrino detectors. Detailed simulations of core-collapse supernovae with up-to-date microphysics, however, show that the standard scenario described here is not guaranteed to succeed, even that it consistently fails to work for the majority of cases if spherical symmetry is imposed (except for the very low-mass end of progenitors that end up with very thin outer hulls and which collapse already when their core consist of oxygen, neon, and magnesium, so called "ONeMg"-core stars).

In his famous review paper, Bethe (1990) noted that there are regions of convective instability not only in the proto neutron star, but also in the outer accretion layer, which would result in large aspheric perturbations. It is thought that the multidimensional flows in the accretion layer are indeed crucial for boosting the efficiency of this mechanism: by allowing matter to stay longer in the region between the shock wave and the proto neutron star where it experiences a net energy gain by neutrino interactions. The convection within the neutron star in contrast was not found to occur in the particularly efficient form of the neutron-fingers, and the gain from the weaker forms actually found in simulations was not enough to account for the explosion on its own. Efforts are currently under way to tackle the full problem for the first time with truly three dimensional simulations including an accurate neutrino treatment and some successes were already found in similarly sophisticated axially-symmetric ("2D") simulations in the past.

Tremendous work has been invested to include all of the many ingredients necessary to simulate core-collapse supernovae. In some areas, such as the behaviour of matter in the high density regime and the associated neutrino interactions, we are forced to resort to experimentally poorly constrained models (see e.g. Lattimer, 2006; Lattimer and Prakash, 2007; Steiner et al., 2013), which are given to us from nuclear theorists e.g. in the form of equation of state tables.

The neutrinos can both be completely trapped in the centre of the remnant, or freely streaming after passing the accretion layer – therefore methods of radiative transfer using the Boltzmann equation have to be used to model their propagation. This is similar to the methods used to describe the propagation of light in optically dense media.

Unfortunately, all these complications make this problem computationally rather demanding, and while the first few attempts to model a few cases also in 3D are ongoing, there is no hope that this will become a routine, desktop calculation in the foreseeable future. Also, while the explosion is certainly a fascinating subject in itself, there is a subsequent phenomenon that is equally interesting and which is more the focus of this thesis: the cooling of the hot, newly formed proto neutron star.

Over a timespan of some ten seconds, this hot object of a few solar masses contained within some tens of kilometres radiates away its excess heat and lepton

---

is generally thought to be unconnected to SN1987A (Arnett et al., 1989) number in the form of neutrinos. This irradiation from the centre is so energetic and persistent that it is able to lift matter from the neutron star's surface and accelerate it in what is called the neutrino driven wind. This gas further contributes to the matter the previous explosion has ejected into the interstellar medium. Both the emitted neutrino signal and the chemical composition of this wind material is affected by the properties of the neutron star and the high density physics necessary to describe it. Depending on the composition and hydrodynamical outflow conditions, this wind is thought to be a potential site for the r-process nucleosynthesis of heavy elements.

It is not feasible to simulate this long cooling phase for even a few models in a manageable period of time in multidimensional simulations. Therefore, in this thesis we have to restrain us to spherically symmetric simulations. However, from theory, multidimensional simulations of the early stage as well as spherically symmetric simulations of the whole cooling phase, it is now firmly established that there exists a convectively unstable region within the proto neutron star's core. While this region might not be the crucial ingredient for driving the explosion, it will certainly influence the efficiency of energy transport and thus the cooling behaviour to a large extent. The way out of this dilemma is a trick from stellar evolution, where additional energy and lepton fluxes are introduced to mimic the mixing of matter by convection, a scheme that is called mixing-length theory. Such a scheme was implemented for this thesis into the supernova simulation code of the Garching group.

Organization of the Thesis

In Chapter 2 we give a short overview about the numerical scheme used and the physical equations necessary for the simulation and introduce the mixing length scheme that was added for the proto neutron star cooling simulations. The remainder of this thesis is organized into three main and one small additional chapter. Chapters 3 to 5 are the main part of this thesis, and each starts with a small introduction into the topic at hand.

In Chapter 3, we evolve a number of progenitors through their gravitational collapse and subsequent accretion phase, looking at the resulting neutrino signal with and without the new mixing length scheme and for different high density equation of state models.

Chapter 4 is similar in principle, but continues the accretion phase for a longer time and looks at the neutrino signal for a few selected, very compact progenitor stars up to the point where their proto neutron stars cross the threshold of instability for black hole formation and collapse.

Then finally in Chapter 5, a few of the proto neutrons stars from Chapter 3 are artificially exploded in order to study the signal of exposed proto neutron stars as would be found after an actual explosion. We will look at the influence of convection and details of the neutrino nucleon interaction on that signal and the composition of the neutrino driven wind.

Lastly, we will shortly describe the result of a small side project that was done in collaboration with Alexander Bartl and Achim Schwenk from the Technical University of Darmstadt in Chapter 6. It concerns the quenching of the axial coupling constant of neutron star matter that enters our neutrino-nucleon cross section and the influence this might have on the neutrino signal.

Is it possible to learn something about neutrino particle physics by studying these events, such as absolute masses, or at least the relative hierarchy of the masses? Can black hole forming core-collapse events be detected in future megaton detectors? Can we learn something about the high density physics governing the neutron star from the neutrino emission of such a cooling remnant? Is r-process nucleosynthesis viable in the neutrino driven wind? We hope that with this thesis we can make at least a small contribution in the quest to answer some of these questions.

2 Numerical Implementation

Overview

The simulations were performed with the VERTEX[1] supernova code of the Garching group.

Its hydrodynamical module is a conservative, time-explicit implementation of the piecewise parabolic method of Colella and Woodward (1984), third order accurate in space and second order in time, based the famous PROMETHEUS code (Fryxell et al. 1989, and partially also Fryxell et al. 2000, which describes the FLASH code, whose hydrodynamics module is based on PROMETHEUS). A number of changes necessary to do supernova physics were implemented by Keil (1997) and Kifonidis et al. (2003).

The neutrino radiative transfer is done with a Boltzmann solver scheme, where an iteration of solutions to moment-equations and a simplified Boltzmann equation is used to find a solution for the full transfer problem. The scheme is not only energy-dependent but also allows for energy-exchanging reactions of neutrinos ("energy-bin-coupling"). It is described extensively in Rampp and Janka (2002), with later additions in Buras et al. (2006b) and Müller (2009).

The implicit neutrino transfer is coupled to the hydrodynamics module via lepton-number-, energy-, and momentum source-terms in an operator split way. While the code is Newtonian in principle, the influence of the effectively deeper potential well in GR is modelled via a post-Newtonian, Tolman-Oppenheimer-Volkoff (TOV) like potential (Marek et al., 2006). Also, important gravitational red-shift and time-dilation effects are taken into-account in the neutrino transfer module, which itself is solving the relativistic equations of transfer accurate to $O(v/c)$.

The individual neutrino reactions used in this study and references for the specific implementation and formulation can be found in Table 2.1. Of particular importance are the neutrino-nucleon opacities, where nucleon correlations at high densities (here modelled according to Burrows and Sawyer 1998, 1999) can significantly reduce the opacity compared to the classical treatment of Bruenn (1985), Mezzacappa and Bruenn (1993b).

Next to this standard setup of the Garching group, we also make use of a mixing-length approach to model the multi-dimensional effects of convection within the proto neutron star in the otherwise spherically symmetric simulations. Similar to usual approaches in stellar evolution, convection is modelled as additional energy

---

[1] **V**ariable **E**ddington factor **R**adiative **T**ransfer for Supernova **EX**plosions

(and lepton-number, composition) fluxes which would arise due to multidimensional convective motions that cannot be modelled in spherically symmetric simulations.

2.1 Hydrodynamical equations

The fundamental equations for the hydrodynamical part of the code are the compressible Euler equations for fluids in spherical symmetry. Basic quantities of these are the baryon density ρ, the matter's radial velocity v, its internal energy density e (and total specific energy density $\epsilon = e + \frac{1}{2}v^2$), and pressure p.

With these, the Euler equations for non-relativistic hydrodynamics in spherical symmetry, i.e. the continuity, energy and momentum equation, are in that order,

$$\frac{\partial}{\partial t}\rho + \frac{1}{r^2}\frac{\partial}{\partial r}\left(r^2 \rho v\right) = 0, \tag{2.1a}$$

$$\frac{\partial}{\partial t}(\rho\epsilon) + \frac{1}{r^2}\frac{\partial}{\partial r}\left(r^2(\rho\epsilon + p)v\right) = -\rho v \frac{\partial}{\partial r}\Phi + Q_{\mathrm{E}} + vQ_{\mathrm{M}}, \tag{2.1b}$$

$$\frac{\partial}{\partial t}(\rho v) + \frac{1}{r^2}\frac{\partial}{\partial r}\left(r^2 \rho v^2\right) + \frac{\partial}{\partial r}p = -\rho\frac{\partial}{\partial r}\Phi + Q_{\mathrm{M}}, \tag{2.1c}$$

where Q_{M} and Q_{E} respectively are the source terms for momentum and energy, for example due to neutrino interactions. Lastly, Φ is the gravitational potential, for the Newtonian case it is the solution of Poisson's equation, in spherical symmetry it is

$$\frac{1}{r^2}\frac{\partial}{\partial r}\left(r^2\frac{\partial\Phi}{\partial r}\right) = 4\pi G\rho. \tag{2.2}$$

As mentioned before, in VERTEX the Newtonian potential is actually replaced with an effective potential modelled after the TOV equation for a spherical matter distribution in general relativity, see Marek et al. (2006) for details on how this is done. This allows to use the (comparatively) simple Newtonian hydrodynamics code but still account for the main effects of the stronger GR potential well. As we will see in Chapter 4, this is a remarkably good approximation and even valid for configurations near the black hole formation threshold. Of course, only the gravitational well is modelled with this method, the dynamics are still Newtonian.

Next to that, additional conservation equations have to be solved to track the evolution of the chemical composition of the matter. For the chemical species i one defines its number fraction Y_i as the ratio of this species' number density n_i over the total baryon number density,

$$Y_i = \frac{n_i}{n_B}. \tag{2.3}$$

A special case is the net electron fraction Y_e: Electron-positron pairs can be thermally created, and so the conserved quantity there is the difference in the number of these two species,

$$Y_e = \frac{n_{e^-} - n_{e^+}}{n_B}. \tag{2.4}$$

In the absence of neutrinos, this is identical to the fraction of (electron flavor) lepton number over baryon number, Y_L. With neutrinos, the net electron neutrino number density also contributes,

$$Y_L = Y_e + Y_\nu = Y_e + \frac{n_{\nu_e} - n_{\bar{\nu}_e}}{n_B} = \frac{n_L}{n_B}, \tag{2.5}$$

however, the evolution of the neutrinos is done in the radiative transfer section. For all other Y_i, an additional continuity equation,

$$\frac{\partial}{\partial t}(\rho Y_i) + \frac{\partial}{\partial i}(\rho Y_i v_i) = Q_{N_i}, \tag{2.6}$$

has to be solved, with possible source terms Q_{N_i}. These arise either due to nuclear reactions, transforming one nuclear species into another, or as the result of the neutrino transfer calculations. There, weak reactions can change both the fraction of electrons and transform protons into neutrons and vice-versa by β-reactions.

2.2 Equation of State

The matter pressure p in the Euler equations has to provided as a function of the thermodynamic state to integrate the system. In the most general case, it is a function of the local internal energy density e, the matter density ρ and the composition Y_i. For the neutrino transfer part, next to that we also need the chemical potentials of electrons, neutrons, and protons.

For densities sufficiently below nuclear density, the matter can be fully described as a mixture of ideal gases of nuclei, possibly degenerate and/or relativistic electrons and positrons, and photons, plus Coulomb lattice effects. The equation of state (EoS) in this regime is implemented as a set of subroutines to calculate the necessary quantities as needed (Janka, 1999).

In the hot and dense environment of a stellar core, nuclear reactions take place and have to be modelled. For supernova simulations an approximate description of nuclear reactions is usually sufficient, indeed for all simulations in this thesis the most important reactions are set to happen instantaneously at threshold temperatures (see. Rampp and Janka, 2002, Appendix B).

At sufficiently high temperatures, the reactions will come into nuclear statistical equilibrium (NSE) and the number densities will be purely a function of the local temperature, density and electron fraction. For the timescales involved in our simulations, we can assume that above a threshold temperature of $T_{\mathrm{NSE}} = 0.5\,\mathrm{MeV}/k_{\mathrm{B}} \approx 5.8 \cdot 10^9\,\mathrm{K}$ the composition is given by the equilibrium distribution.

For densities approaching and exceeding the density of nuclei, the necessary physics to describe the resulting matter gets much more demanding – in this regime we have to resort to tabulated nuclear physics results. These tables have to be combined with the low-density equation of state, for this we define a threshold density ρ_{HD} above which the high-density prescription is used, set to values from

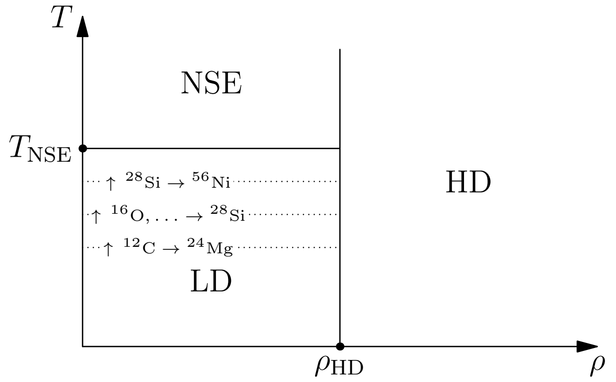

Figure 2.1: The (ρ, T) partition used for the various equation of state regimes necessary for the simulations. In the HD region the tabulated proto neutron star equations of state are used, and depending on the temperature the low density regime is split into a region where the composition is calculated from nuclear statistical equilibrium, or where an approximate burning treatment is employed.

about 10^7g/cm^3 during the gravitational collapse to 10^{11}g/cm^3 in the subsequent evolution of the formed proto neutron star. Confer to Figure 2.1 for a visualization of the equation of state and nuclear burning setup.

As one nuclear physics model, we use the table by Shen et al. (1998a,b) – the "Shen" EoS – in the updated form of "EOS1" of Shen et al. (2011). It is based on a relativistic mean field model to model neutron star matter as a mixture of neutrons, protons, alpha particles, and a single representative heavy nucleus (with varying properties). As a second model, we take the tables of Lattimer and Swesty (1991 and Lattimer et al., 1985), there in two variants as "LS180" and "LS220". They too describe the high density matter as a mixture of n, p, α, and a heavy representative nucleus but are based on a compressible liquid drop model. Their model comes in three different versions for the nuclear compressibility parameter K, a measure of the "stiffness" of symmetric nuclear matter. It is the density dependence of the per baryon free energy f_B (see Lattimer and Swesty, 1991), evaluated at nuclear saturation density $n_s = 0.155\text{fm}^{-3}$,

$$\mathsf{K} = \frac{1}{9} n_s^2 \frac{\partial^2 f_B}{\partial n^2} \bigg|_{n=n_s, Y_e=\frac{1}{2}, T\to 0} . \tag{2.7}$$

Of these three we use the $\mathsf{K} = 180\,\text{MeV}$ and $220\,\text{MeV}$ versions , the former as it was used extensively in the literature, but for most of the simulations in this thesis we make use of the latter. This is mostly motivated due to the recent solid measurements of $\sim 2\text{M}_\odot$ neutron stars (Demorest et al., 2010; Antoniadis et al., 2013) that are incompatible with the resulting maximum neutron star attainable with the LS180. For reference, the corresponding value of K for the Shen EoS is even higher, 281 MeV.

For the proto neutron star cooling, another quantity is also of relevance, the so-called symmetry energy, defined as

$$\mathsf{J} = \frac{1}{8}\frac{\partial^2 f_B}{\partial Y_e^2}\bigg|_{n=n_s, Y_e=\frac{1}{2}, T\to 0}. \tag{2.8}$$

It is 28.61 MeV for the LS180 and LS220, and 36.89 MeV for the Shen EoS.

2.3 Neutrino radiative transfer

Next to the stellar gas, copious amounts of neutrinos will be created in a supernova. Their transport through the medium and their interaction with it (and themselves!) is complicated by the fact, that their interaction cross sections have a strong energy dependence.

They are completely "trapped" in the inside of the dense proto neutron star core and behave essentially like another fluid component, only able to escape by very slow diffusion processes. Far out, in less dense matter, they can stream freely and are completely decoupled from the ordinary matter. All regimes in between these two extreme cases have to be modelled for the supernova case.

The method to accomplish this is the theory of radiative transfer, the same method used to model photons escaping ordinary stars. On the one hand, neutrino transfer is considerably simpler than photon transfer, as there are no line structures arising from complicated atomic transition levels. On the other hand, the interaction cross sections – especially in the high density regime – can turn out to be quite complicated, and computationally expensive. Also, there are six different flavors of neutrinos, all of which are abundantly created and have to be modelled each. Next to that, for the neutrino densities involved, neutrino-neutrino pair interactions start to play an important role.

In VERTEX, the six different neutrino flavors are modelled by only three groups, two for the electron and anti-electron neutrinos and an additional group for a mean, representative neutrino species "ν_x" modelling all four neutrinos of the heavy lepton generations $(\nu_\mu, \bar{\nu}_\mu, \nu_\tau, \bar{\nu}_\tau)$.

The reason why one can do this, is that a star consist only of the stable matter of the first generation, and therefore all heavy lepton neutrinos will interact only via neutral currents with the medium, and in exactly the same way (the energies involved are much to small to generate appreciable amounts of μ-leptons). Strictly speaking, this is not entirely true, an effect called weak magnetism causes a slight difference in the cross sections between neutrinos and anti-neutrinos, due to a CP violating interference between the weak magnetic moment and the axial vector current of nucleons (Horowitz, 2002). This is implemented for electron neutrinos and anti-neutrinos, but only the averaged effect is applied to the ν_x. In a comparison of VERTEX and the AGILE-BOLTZTRAN code of the Oak Ridge-Basel group (Liebendörfer et al., 2005), that did go through the effort to split up the heavy lepton neutrinos and anti-neutrinos, this simplification was not found to have a big impact.

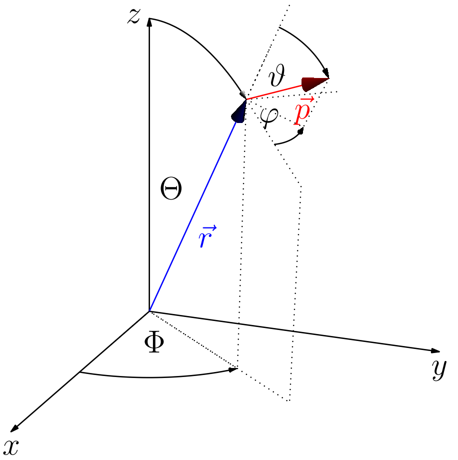

Figure 2.2: The doubly spherical coordinate system, for the space vector $\vec{r}$ and the neutrino momentum $\vec{p}$ at each point in space. In spherical symmetry only the radius r, the neutrino energy $\varepsilon = |\vec{p}|c$, and the cylindrically symmetric neutrino distribution along the angle ϑ at each point remain.

However, in very long cooling simulations such as are done in Chapter 5, the slight difference in the diffusion time for ν_μ and $\bar{\nu}_\mu$ might lead to the build-up of a fraction of muons from the thermal tails of their distribution functions inside the cooling proto neutron star, which we neglect in all our simulations.

The two electron flavor neutrinos, however, definitively have an additional, strong reaction channel via charged currents on either neutrons or protons, and therefore have to be modelled separately.

The governing equation for radiative transfer is the Boltzmann Equation, that models the evolution of the seven dimensional particle distribution function $f(\vec{x}, \vec{p}, t)$, with which the number of particles $\mathrm{d}N$ in a given region of space and momentum is given by $\mathrm{d}N = f(\vec{x}, \vec{p})\mathrm{d}^3x\,\mathrm{d}^3p$.

For stars, a natural representation of space are spherical coordinates (r, Θ, Φ), in momentum space the neutrinos are equally represented by their energy ε, and two angles (ϑ, φ), indicating the angle relative to the local radial direction, confer to Figure 2.2. In spherical symmetry, the seven dimensional problem in $(r, \Theta, \Phi, \varepsilon, \vartheta, \varphi, t)$ reduces to a four dimensional problem in $(r, \varepsilon, \vartheta, t)$. Two spatial dimensions disappear, along with the φ of the momentum dimensions. However, even in spherical symmetry there remains an angular neutrino distribution in ϑ at each radial point, the spatial spherical symmetry mandates only that this angular distribution is then cylindrically symmetric around the radial direction. Thus even seemingly one-dimensional, spherically symmetric simulations have to evolve three dimensional fields in order to solve the radiative transfer equations.

Traditionally, the quantity used for radiative transfer is the so called specific intensity $\mathcal{I}$ which is related to the particle distribution function by

$$\mathcal{I} = \frac{\varepsilon^3}{h^3c^2}f. \tag{2.9}$$

The code uses the neutrino quantities in the comoving-coordinates of the fluid at each zone, and solves the transfer equation to $\mathcal{O}(\beta)$, where β is the local fluid velocity divided by the speed of light. Setting $\mu = \cos\vartheta$, the transfer equation for one particular neutrino species to $\mathcal{O}(\beta)$ is (Rampp and Janka, 2002)

$$\begin{aligned}\left(\frac{1}{c}\frac{\partial}{\partial t} + \beta\frac{\partial}{\partial r}\right)\mathcal{I} + \mu\frac{\partial}{\partial r}\mathcal{I} + \frac{1-\mu^2}{r}\frac{\partial}{\partial \mu}\mathcal{I}& \\ + \frac{\partial}{\partial \mu}\left[(1-\mu^2)\left(\mu\left(\frac{\beta}{r} - \frac{\partial \beta}{\partial r}\right) - \frac{1}{c}\frac{\partial \beta}{\partial t}\right)\mathcal{I}\right]& \\ - \frac{\partial}{\partial \varepsilon}\left[\varepsilon\left((1-\mu^2)\frac{\beta}{r} + \mu^2\frac{\partial \beta}{\partial r} + \mu\frac{1}{c}\frac{\partial \beta}{\partial t}\right)\mathcal{I}\right]& \\ + \left((3-\mu^2)\frac{\beta}{r} + (1+\mu^2)\frac{\partial \beta}{\partial r} + \mu\frac{2}{c}\frac{\partial \beta}{\partial t}\right)\mathcal{I} &= C[\mathcal{I}]. \end{aligned} \tag{2.10}$$

All the interesting physics and all of the complications in solving this equation are hidden in the so-called “collision integral” $C[\mathcal{I}]$. It is the source term for the specific intensity, prescribing how the neutrinos are created, redistributed, and annihilated in phase-space. Not only does this contain complicated, and computationally expensive terms due to neutrino and high-density physics, but contains in itself integrals of the current and other neutrino species’ specific intensity over the neutrino energy space. This makes (2.10) a non-linear integro-partial-differential equation.

The solution strategy of our code is to take succesive moments $\int \mathrm{d}\mu\mu^n$ over the neutrino angle-cosine, which creates a system of moment equations with the μ dimension integrated out. If we define the moments of $\mathcal{I}$ as

$$\{J, H, K, L, \dots\}(r, t, \varepsilon) = \frac{1}{2}\int_{-1}^{+1} \mu^{\{0,1,2,3,\dots\}}\mathcal{I}(r, t, \varepsilon, \mu)d\mu, \tag{2.11}$$

the first two moment equations of (2.10) are

$$\begin{aligned}\left(\frac{1}{c}\frac{\partial}{\partial t} + \beta\frac{\partial}{\partial r}\right)J + \frac{1}{r^2}\frac{\partial}{\partial r}(r^2H)& \\ - \frac{\partial}{\partial \varepsilon}\left[\varepsilon\left(\frac{\beta}{r}(J-K) + \frac{\partial \beta}{\partial r}K + \frac{1}{c}\frac{\partial \beta}{\partial t}H\right)\right]& \\ + \frac{\beta}{r}(3J-K) + \frac{\partial \beta}{\partial r}(J+K) + \frac{2}{c}\frac{\partial \beta}{\partial t}H &= C^{(0)}, \end{aligned} \tag{2.12}$$

$$\left(\frac{1}{c}\frac{\partial}{\partial t}+\beta\frac{\partial}{\partial r}\right)H+\frac{1}{r^2}\frac{\partial}{\partial r}(r^2K)+\frac{K-J}{r}$$
$$-\frac{\partial}{\partial\varepsilon}\left[\varepsilon\left(\frac{\beta}{r}(H-L)+\frac{\partial\beta}{\partial r}L+\frac{1}{c}\frac{\partial\beta}{\partial t}K\right)\right]$$
$$+\left(\frac{\partial\beta}{\partial r}+\frac{\beta}{r}\right)H+\frac{1}{c}\frac{\partial\beta}{\partial t}(J+K)=C^{(1)}. \quad (2.13)$$

Here, the quantities $C^{(n)}$ are the corresponding moments over the collision integral,

$$C^{(n)}=\frac{1}{2}\int_{-1}^{+1}\mu^n(\eta-\chi\mathcal{I})d\mu. \quad (2.14)$$

The first few moments can directly by identified with physical properties of the neutrino radiation field. J is proportional to the energy distribution of the neutrino energy density and H to the energy distribution of the neutrino energy flux – that is, the energy distribution of all effectively out-streaming neutrinos. Most often this is encountered in the form of the neutrino luminosity, which unfortunately is also denoted by L, the radiated neutrino energy flux through the sphere with radius r enclosing the coordinate centre,

$$L(r,t)=4\pi r^2\int_0^\infty \mathrm{d}\varepsilon\, H(r,t,\varepsilon). \quad (2.15)$$

In honour of Hans Bethe and for his contribution to supernova research it has become customary in the last few years to define the energy of

$$10^{51}\mathrm{erg}=1\,\mathrm{B}, \quad (2.16)$$

one "Bethe", a typical energy scale appearing in supernova processes, and luminosities are thus also usually given in terms of B/s.

Next to the energy moments, one sometimes also encounters the corresponding neutrino number distributions, defined as

$$\{\mathcal{J},\mathcal{H},\mathcal{K},\mathcal{L},\dots\}(r,t,\varepsilon)=\frac{1}{2}\int_{-1}^{+1}\mu^{\{0,1,2,3,\dots\}}\varepsilon^{-1}\mathcal{I}(r,t,\varepsilon,\mu)d\mu. \quad (2.17)$$

Again, the first few have direct physical meaning, $\mathcal{J}$ is proportional to the neutrino number density, $\mathcal{H}$ to the neutrino number flux. The analogous quantity to the luminosity is the neutrino number flux,

$$\dot{N}=4\pi r^2\int_0^\infty \mathrm{d}\,\varepsilon\mathcal{H}(r,t,\varepsilon). \quad (2.18)$$

There exist simple Lorentz transformation rules in order to evaluate these quantities also in other frames of reference than comoving with the local fluid velocity, for example a resting observer's frame. These and a detailed derivation for arbitrary moments are given in Appendix A.

Table 2.1: Included neutrino interactions, the numerical implementation is described in detail in Rampp and Janka (2002), Buras et al. (2003a) and Buras et al. (2006b). The symbol ν represents any neutrino or anti-neutrino, A represents heavy nuclei, N stands for any nucleon, that is both neutrons or protons.

Reaction			References
$\nu\, e^{\pm}$	$\rightleftharpoons$	$\nu\, e^{\pm}$	Mezzacappa and Bruenn (1993a), Cernohorsky (1994)
$\nu\, A$	$\rightleftharpoons$	$\nu\, A$	Horowitz (1997), Bruenn and Mezzacappa (1997)
$\nu\, N$	$\rightleftharpoons$	$\nu\, N$	Bruenn (1985), Mezzacappa and Bruenn (1993b), Burrows and Sawyer (1998), Horowitz (2002), Carter and Prakash (2002), Reddy et al. (1999)
$\nu_e\, n$	$\rightleftharpoons$	$e^-\, p$	–"–, Burrows and Sawyer (1999)
$\bar{\nu}_e\, p$	$\rightleftharpoons$	$e^+\, n$	–"–, Burrows and Sawyer (1999)
$\nu_e\, A'$	$\rightleftharpoons$	$e^-\, A$	Bruenn (1985), Mezzacappa and Bruenn (1993b), Langanke et al. (2003)
$\nu\, \bar{\nu}$	$\rightleftharpoons$	$e^-\, e^+$	Bruenn (1985), Pons et al. (1998)
$\nu\bar{\nu}\, NN$	$\rightleftharpoons$	NN	Hannestad and Raffelt (1998)
νA	$\rightleftharpoons$	νA^*	Langanke et al. (2008)
$\nu_{\mu,\tau}\bar{\nu}_{\mu,\tau}$	$\rightleftharpoons$	$\nu_e\bar{\nu}_e$	Buras et al. (2003a)
$\overset{(-)}{\nu}_{\mu,\tau}\,\overset{(-)}{\nu}_e$	$\rightleftharpoons$	$\overset{(-)}{\nu}_{\mu,\tau}\,\overset{(-)}{\nu}_e$	Buras et al. (2003a)

One can include more and more of these moment equations, however, the resulting system will never be closed, as the equations will inevitably include higher and higher moments of $\mathcal{I}$. The way out is to truncate the system – here after the first two equations – and introduce a closure relation between the next moments and the first two, J and H, usually by defining the Eddington factors,

$$f_K = \frac{K}{J}, \tag{2.19}$$

$$f_L = \frac{L}{J}. \tag{2.20}$$

If these would be known, the system of the two moment equations above could be closed. To achieve this, the Eddington factors are in turn determined by solving a simplified Boltzmann equation, where the collision term is evaluated with moments of the initial, given neutrino intensity $\mathcal{I}$. This is then iterated, the Eddington factors are fed into the system of moment equations and the resulting moments are used for the collision term in the Boltzmann equation, until a converging solution is found. All in all, the whole procedure is then equivalent to solving the full Boltzmann problem.

The individual neutrino interaction processes implemented in the code for the collision terms can be found in Table 2.1. After a transport step, the back-reaction to the hydrodynamics module is achieved via the aforementioned source terms, they can be calculated out of the collision moments of the various neutrino species

i as

$$Q_{\mathrm{E}} = -4\pi \int_0^\infty \mathrm{d}\varepsilon \sum_i C^{(0)}_{\nu_i}(\varepsilon), \tag{2.21}$$

$$Q_{\mathrm{M}} = -\frac{4\pi}{c} \int_0^\infty \mathrm{d}\varepsilon \sum_i C^{(1)}_{\nu_i}(\varepsilon), \tag{2.22}$$

$$Q_{\mathrm{N}} = -4\pi m_{\mathrm{B}} \int_0^\infty \mathrm{d}\varepsilon\, \varepsilon^{-1} \Big(C^{(0)}_{\nu_e}(\varepsilon) - C^{(0)}_{\bar{\nu}_e}(\varepsilon) \Big). \tag{2.23}$$

Here, m_{B} is the baryon mass used in defining our matter density ρ.

A very detailed description and the explicit discretization of the numerical scheme can be found in Rampp and Janka (2002). Our numerical grid encompasses 21 fixed, roughly logarithmically spaced bins from 0.4 to 380 MeV in neutrino energy space. The spatial and angular dimension is periodically refined to account for the changing stratification, with typically $\mathcal{O}(300 - 800)$ angular and radial zones for the neutrino transport and $\mathcal{O}(800 - 1200)$ radial zones for the hydrodynamical quantities.

The solution of the neutrino transfer part is quite computationally expensive, to allow for a sufficiently large time-step and in order to tame the stiff source terms in the neutrino opacities, it is done with an implicit scheme. The neutrino transfer part and the hydrodynamics module are coupled together only via the source terms and are evaluated in an operator split way: an implicit neutrino transfer time step is computed and then a number of hydro steps are done, applying the calculated source terms in their equations.

It is advantageous to do several, comparably cheap hydrodynamical steps for each transport step, as the time stepping of our explicit scheme is strongly limited by the Courant-Friedrichs-Lewy condition, which constrains the length of an explicit time step to at most the duration the fastest waves of the underlying equations need to traverse a grid cell. In our case these are sound waves and in the proto neutron star the speed of sound can easily get $\mathcal{O}(c/2)$.

2.4 Mixing length convection treatment

Spherically symmetric models have the fundamental drawback that they cannot accurately represent the inherently multidimensional effect of convection. The origin of convection is the potential instability when a small displacement of a fluid element out of its neighbourhood into another thermodynamic configuration results in an amplification of this displacement. This can happen if its own thermodynamic state does not fully equilibrate with the new surroundings on the timescale of the movement.

In the context of supernova simulations, an enhanced neutrino luminosity as a result of convection in the proto neutron star as a means for enabling a robust explosion mechanism was first suggested by Wilson and Mayle (1988). They suggested that in the proto neutron star's core a convective mechanism similar to what happens in Earth's oceans could take place. There, hot and salty water stratified above a layer of colder, less salty water experiences an instability due to the different timescales of salt diffusion and heat-exchange. If an element of the hot layer is displaced into the cold layer, it turns out that it will loose its excess heat faster than its salt concentration, and the now cooled water will continue to sink due to its increased density compared to the less salty cold water around it.

In the proto neutron star, the roles of salt concentration was to be the neutron fraction, and it was thought that neutrino reactions off all flavors would more quickly bring the material into temperature equilibrium than into composition equilibrium, which would only be mediated by the difference in neutrino electron and anti-electron density.

However, further analysis (Bruenn and Dineva, 1996; Bruenn et al., 2004) revealed that these conditions were not fulfilled, in fact the composition is changed faster than energy. However, other forms of instability in the proto neutron star are present and were also seen in actual multidimensional simulations (Herant et al., 1994; Fryer and Warren, 2002; Buras et al., 2003b) - just not in the very efficient form of the neutron fingers envisioned by Wilson and Mayle (1988), whose work nevertheless demonstrated what effect an efficient convective mixing inside the proto neutron star can have on the neutrino signal and energy release.

In the following motivation we closely follow Wilson and Mayle (1988). Three different regimes have to be compared, the conditions in the lower layer (pressure, p_0, entropy s_0, and electron fraction Y_{e0}), in the layer above this, (p_1, s_1, Y_{e1}), and the conditions that are the result of a fluid element movement, (p_m, s_m, Y_{em}), see Figure 2.3. In general, convection occurs if the movement results in a change in density $\Delta\rho = \rho(p_m, s_m, Y_{em}) - \rho(p_0, s_0, Y_{e0})$ over the travelled length Δr which is less than that given by the corresponding density gradient present in the stratification of the surrounding material, that is if

$$\frac{\Delta\rho}{\Delta r} < \frac{\mathrm{d}\rho}{\mathrm{d}r}, \tag{2.24}$$

$$\text{or } C_{\text{convection}} := \frac{\mathrm{d}\rho}{\mathrm{d}r} - \frac{\Delta\rho}{\Delta r} > 0. \tag{2.25}$$

Then, the new density of the blob is lower than its surrounding material, it will rise even further - the stratification was unstable against a small movement of the blob. In spherical symmetry, however, this can never happen, as different fluid elements can never pass each other. Therefore, 1D simulations very often form hydrodynamic configurations that would be unstable to multidimensional perturbations.

Depending on the ratios of the timescales of the microscopic, thermodynamic processes and the macroscopic movement involved, there are different kinds of convection scenarios.

The classical situation where a fluid element moves adiabatically but adapts to the surrounding pressure and composition is called Schwarzschild convection. There, the timescale for energy exchange is large compared to the timescales of pressure (mediated by soundwaves) and composition equilibration (mediated by

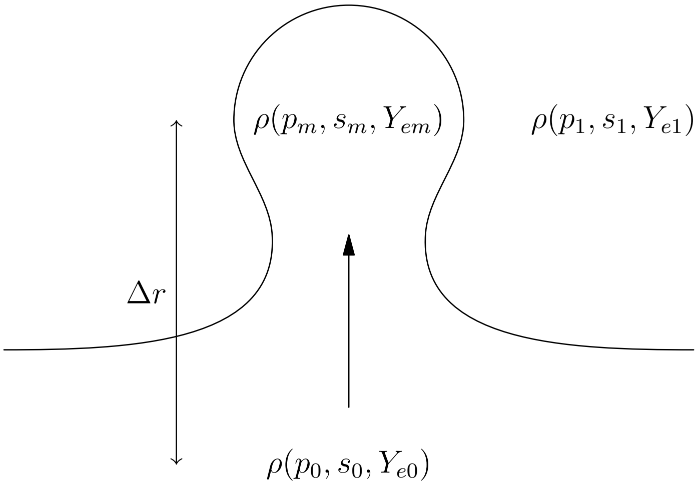

Figure 2.3: A schematic picture of the three regimes important for convective processes, the two layers below (0) and above (1) and the conditions in the blob after some movement (m) over the typical length of a fluctuation Δr. The values in (m) will potentially only partially adjust themselves to the values outside over the timescale of the movement. If the blobs new density $\rho(p_m, s_m, Y_{em})$ is smaller than the outside density $\rho(p_1, s_1, Y_{e1})$, the blob will continue to rise and start a convective motion.

diffusion, nuclear reactions or, in our case, neutrinos), thus $p_m \rightarrow p_1$ and $Y_{em} \rightarrow Y_{e1}$, while $s_m = s_0$ stays unchanged. The resulting change in density for the element is then

$$\Delta\rho = \rho(p_m, s_0, Y_{em}) - \rho(p_0, s_0, Y_{e0}) \tag{2.26}$$

$$\simeq \left(\frac{\partial\rho}{\partial p}\right)_{s,Y_e}(p_1 - p_0) + \left(\frac{\partial\rho}{\partial Y_e}\right)_{p,s}(Y_{e1} - Y_{e0}), \tag{2.27}$$

and therefore

$$\frac{\Delta\rho}{\Delta r} \simeq \left(\frac{\partial\rho}{\partial p}\right)_{s,Y_e}\frac{\mathrm{d}p}{\mathrm{d}r} + \left(\frac{\partial\rho}{\partial Y_e}\right)_{p,s}\frac{\mathrm{d}Y_e}{\mathrm{d}r} \tag{2.28}$$

$$= \frac{\mathrm{d}\rho}{\mathrm{d}r} - \left(\frac{\partial\rho}{\partial s}\right)_{p,Y_e}\frac{\mathrm{d}s}{\mathrm{d}r}. \tag{2.29}$$

If we substitute this in the instability criterion of Eq. (2.24) we end up with the condition for Schwarzschild convection as

$$C_{\text{schwarzschild}} = \left(\frac{\partial\rho}{\partial s}\right)_{p,Y_e}\frac{\mathrm{d}s}{\mathrm{d}r} > 0. \tag{2.30}$$

This can be simplified further, as density is for almost all equations of state decreasing with increasing temperature and as

$$\left(\frac{\partial\rho}{\partial s}\right)_{p,Y_e} = \frac{T}{c_p}\left(\frac{\partial\rho}{\partial T}\right)_{p,Y_e} < 0, \tag{2.31}$$

with $c_p > 0$ the heat capacity at constant pressure, one has

$$\frac{\mathrm{d}s}{\mathrm{d}r} < 0 \tag{2.32}$$

as the criterion for instability against Schwarzschild-type convection.

Other types of convection scenarios include the aforementioned salt-finger instability, with $(p_m, T_m, Y_{em}) \to (p_1, T_1, Y_{e0})$, resulting in

$$C_{\text{finger}} = \left(\frac{\partial \rho}{\partial Y_e}\right)_{p,T} \frac{\mathrm{d}Y_e}{\mathrm{d}r} > 0, \tag{2.33}$$

and Ledoux-convection where the blob moves both adiabatically and without changing its composition, that is $(p_m, s_m, Y_{em}) \to (p_1, s_0, Y_{e0})$. There, the condition for instability consequently involves two thermodynamic derivatives, namely

$$C_{\text{ledoux}} = \left(\frac{\partial \rho}{\partial s}\right)_{p,Y_e} \frac{\mathrm{d}s}{\mathrm{d}r} + \left(\frac{\partial \rho}{\partial Y_e}\right)_{p,s} \frac{\mathrm{d}Y_e}{\mathrm{d}r} > 0. \tag{2.34}$$

Here, the situation is not as simple as in the Schwarzschild convection, as the second thermodynamic derivative in Eq. (2.34) can assume both positive and negative values (see Roberts et al. 2012b for a discussion on how this is related to the symmetry energy of nuclear matter). It will thus be sensitive to the high density equation of state model used.

For practical purposes, we can rewrite Eq. (2.34) into a form where only total derivatives of the quantities that are directly used in the code are necessary (see Appendix B for a detailed derivation),

$$C_{\text{ledoux}} = \frac{\mathrm{d}\rho}{\mathrm{d}r} - \frac{1}{c_s^2}\frac{\mathrm{d}p}{\mathrm{d}r}. \tag{2.35}$$

A direct, physical measure for the growth rate of a convective instability (for the linearised equations) is given by the so-called Brunt–Väisälä frequency ω_{BV}.

$$\omega_{\text{BV}} = \operatorname{sign}(C)\sqrt{-\frac{g}{\rho}|C|} \tag{2.36}$$

where $g < 0$ is the local gravitational acceleration, $g = -\partial\Phi/\partial r$. With this definition, ω_{BV} is positive for convectively unstable stratifications and denotes a linearised growth rate (if negative, it would correspond to a oscillation frequency for material that was forced out of the stable stratification).

2.4.1 Mixing length scheme

A widely used technique in stellar evolution is to model the multidimensional effects of convection in computationally tractable 1D simulations by adding artificial energy and composition fluxes. These are constructed in such a way as to drive the convectively unstable gradients into stable ones.

For this, it is assumed that the convective blobs travel for some characteristic length scale, the eponymous "mixing-length" – the free parameter of the model. After that, they dissolve and deposit the material from below in their new surroundings. Furthermore, this process is to happen instantaneously and is modelled by a purely local modification of energy and composition fluxes. It is usually assumed that the characteristic length scale is related to the pressure scale height, we therefore set it to

$$\Delta r = \alpha \cdot \frac{p}{\mathrm{d}p/\mathrm{d}r}, \tag{2.37}$$

where we set $\alpha = \mathcal{O}(1)$ as the free parameter of the model. After travelling Δr upwards, the difference in density of the surrounding medium to the fluid density is precisely

$$\Delta\rho = \Delta r \cdot C_{\text{convection}}, \tag{2.38}$$

where $C_{\text{convection}}$ is the appropriate kind of convection of the previous section for which the conditions are fulfilled. In our case we will assume Ledoux convection to take place.

Energy conservation implies that the fluid element will attain a velocity v_{mix} due to the released potential energy,

$$\frac{1}{2}\rho v_{\text{mix}}^2 = g\Delta\rho\Delta r. \tag{2.39}$$

where g is the local gravitational acceleration, and thus

$$v_{\text{mix}} = \sqrt{2g\frac{\Delta\rho}{\rho}\Delta r}. \tag{2.40}$$

With this, we are now able to derive the necessary fluxes for the scheme. Over Δr, a fluid element will transport a lepton number of $\mathrm{d}Y_e/\mathrm{d}r \cdot \Delta r$, as we assumed in the Ledoux case that the lepton number would not be changed for the moving fluid element on its way. This results in an electron fraction flux of

$$F_{\text{e}}^{\text{mix}} = \rho v_{\text{mix}} \Delta r \cdot \frac{\mathrm{d}Y_e}{\mathrm{d}r}, \tag{2.41}$$

and similar fluxes are also applied for each of the other chemical species. For the energy flux, there is also a contribution from $p\,dV$ work that is released when the dense blob is uncompressed on its way up - next to the internal energy ϵ that is directly transported with the flowing matter. The appropriate thermodynamic potential is thus the specific enthalpy, $h = \epsilon + p/\rho$. In Ledoux convection we assumed adiabatic expansion, from the total difference $\mathrm{d}h/\mathrm{d}r \cdot \Delta r$ from the given background stratification we therefore have to subtract the change in h due to adiabatic expansion,

$$\Delta h_{\text{ad}} = \left(\frac{\partial h}{\partial p}\right)_{s,Y_e} \frac{\mathrm{d}p}{\mathrm{d}r} \cdot \Delta r. \tag{2.42}$$

This gives for the total energy flux due to the convective mixing

$$F^{\text{mix}}_{\text{energy}} = \rho v_{\text{mix}} \Delta r \cdot \left(\frac{\mathrm{d}h}{\mathrm{d}r} - \frac{\Delta h_{\text{ad}}}{\Delta r} \right). \tag{2.43}$$

Using $\mathrm{d}h = T\,\mathrm{d}s + 1/\rho\,\mathrm{d}p$ and the explicit form for h this can be expressed in gradients of the internal energy ϵ, which is the quantity directly available in the code, to

$$F^{\text{mix}}_{\text{energy}} = \rho v_{\text{mix}} \Delta r \cdot \left(\frac{\mathrm{d}\epsilon}{\mathrm{d}r} + p \frac{\mathrm{d}(1/\rho)}{\mathrm{d}r} \right). \tag{2.44}$$

Numerical experiments revealed that the results are very insensitive to the precise value of the free parameter α, no discernible differences where visible between $\alpha = 1$ or 10.

There was one implicit simplification throughout this section, namely that the convective motions only transport net electron number density and not the - strongly coupled - net electron neutrino number density. This is obviously a simplification, as moving matter in the dense proto neutron star will carry the trapped neutrinos along. However, in practice the difference turns out to be minimal (B. Müller, personal communication) and the treatment with $Y_{\text{lep}} \approx Y_e$ is computationally much simpler to implement, the necessary changes then only affect the hydrodynamical part of the program. Next to that, additional considerations would be necessary to account for the very fact that the neutrinos are not everywhere trapped to the same degree, and even decouple completely at some point.

This necessitates that regions of convective instability and the region of decoupling of the various neutrinos – the so called “neutrinospheres” – do not overlap. Fortunately, as we will find in the forthcoming chapters, this is found in actual simulations.

3 Collapse and Accretion

At the end of the nuclear fusion ladder, a star that was formed with an initial mass of $\gtrsim 8\mathrm{M}_\odot$ produces iron group elements in its central region. This final "ash" of fusion reactions accumulates there. Above a critical mass limit, the Chandrasekhar-Mass, electron degeneracy pressure – the dominant pressure contribution at the high densities in a star's core – is no longer able to support the iron core's own increasing gravitational pull and a dynamical collapse sets in. Additionally, dissociation of heavy nuclei into α-particles and nucleons and electron captures on nuclei rob the core of even more thermal and degeneracy pressure support by consuming energy in the dissociation and converting electrons into electron neutrinos that quickly escape the star.

Meanwhile, the gravitational binding energy of the iron core is mostly released as neutrinos, which can initially escape the star's core unhindered. As the densities get higher ($\gtrsim 10^{11}\mathrm{g/cm}^3$), though, the material becomes opaque even for the weakly interacting neutrinos. They get effectively trapped in the material, and with this energy sink gone the subsequent collapse proceeds adiabatically.

As the core proceeds to higher and higher densities, it gets a second chance to avoid the imminent and irreversible fate of a black hole, when the material is compressed to densities that approach those found inside an atomic nucleus. At these conditions, the heavy nuclei are so near each other that they begin to feel themselves also via the strong force. The heavy nuclei then dissolve into individual nucleons in very close proximity, a (proto) neutron star (PNS) is born. Now the increasingly repulsive nuclear forces provide – for the moment – enough additional pressure support to abruptly stop the collapse. Inertia compresses the core even somewhat above the new equilibrium density, for a short, intense moment it expands again and launches a shock-wave against the still in-falling hull of the star. At first, it was thought that this was the actual mechanism to explode the rest of the star. However, in detailed simulations it is found that the energy contained in the outward moving part of this initial, prompt shock was quickly consumed by the dissociation of the infalling heavy nuclei into individual nucleons. After a short peak in the contained kinetic energy of $\sim 10^{49}$ erg, all the material attains negative velocities again, after less than a millisecond. The outward moving shock-wave turns into an accretion shock. Its radial position will still move outwards to a maximum of some $\sim 100\mathrm{km}$, as the advected material behind it needs some time to cool and release its thermal energy.

All the while, the rest of the star still accretes onto the newborn proto neutron star and releases its binding energy in an intense source of neutrinos. Next to that, the trapped neutrinos from within the proto neutron star's core slowly diffuse out of the optically-thick centre on a comparably long diffusion time-scale.

It is thought that this vast amount of energetic neutrinos can then deposit just enough energy in the dense material behind the shock-wave to heat the material there enough to stop the infall, accelerate it outwards and unbind the outer remains of the star. Hours later, this revived shock wave will then reach the edge of the remaining star and only then will it become visible also optically as an astronomical supernova. Just a small percentage of the energy the neutrinos carry with them ($\mathcal{O}(10^{52-53})$ erg) have to be deposited in the material behind the accretion shock for this to work.

The problem with this scenario, the delayed neutrino heating mechanism, is that it robustly fails to work in the most detailed supernova simulations if done in spherical symmetry, except for the very low-mass end of stars.

It is thought that multidimensional flows of the material behind the shock and above the proto neutron star play a crucial role to enhance the amount of energy the neutrinos can deposit there. Indeed, in axially symmetric ("2D") simulations, some successful explosions could be found (e.g. in Marek and Janka, 2009), and current efforts are under way to investigate the behaviour in fully three-dimensional simulations that also include a sufficiently detailed neutrino radiative transfer scheme.

In this chapter and this thesis in general, the focus will however not be to investigate the conditions and intricacies of the explosion mechanism. Instead, in this section we want to investigate the neutrino signal emanating during the pre-explosion phase, where material is accreeting onto a newly-born proto neutron star. Spherical symmetry will certainly be a good approximation for the first 100ms after core-bounce, then convective overturn in the layer between the shock and the proto neutron stars surface will start to develop. This would break spherical symmetry and lead to an asymmetric accretion onto the proto neutron star. Still, up to the time of an eventual explosion, material is still accreted through the shock with the same rate as in spherically symmetric simulations, the material from the outside has a supersonic infall velocity and thus cannot react to the changed conditions behind the shock.

Therefore, spherical symmetry might still be a reasonable approximation during the period between 100ms and the onset of the conditions beneficial for an explosion. When an explosion stars to set in, however, it will of course loose its justification completely. The typical explosion time for the delayed neutrino mechanism is quite uncertain, the diminishing neutrino luminosities make it however increasingly unlikely that it is much later than 0.5s after core bounce. This was also the time frame for the length of the simulations in this chapter, taken as an upper limit – it is probably safe to say that the effects of an explosion will become important before this point.

For some stars, however, the delayed neutrino mechanism might just not do it, in that case the accretion phase will go on until the proto neutron star will become massive enough to form a black hole. This scenario is explored in Chapter 4.

Multidimensional effect also play a role within the proto neutron stars core, as has been outlined in Section 2.4, and will be treated accordingly. After Mayle and Wilson (1988) and Wilson and Mayle (1988, 1993) invoked strong convective mixing within the proto neutron star in order to trigger successful explosions in 1D via “neutron fingers” (cf. Section 2.4), a number of studies have been done to investigate the effect of convection in more detail.

Analytical considerations by Bruenn and Dineva (1996) and in more detail in a preprint by Bruenn et al. (2004) found unfavourable conditions for neutron fingers, but instead instability against Ledoux and doubly-diffusive type convection.

Müller and Janka (1994) and later Janka and Müller (1996) and Keil et al. (1996) performed 2D simulations of the outer layers of a proto neutron star in a core collapse environment, with a prescribed neutrino luminosity at the inner boundary and a parametrized, prescription for the neutrino transfer. Within that setup, they found that a convective region develops below and near the neutrinospheres, which led to an enhancement, up to factors of 2, of the neutrino luminosity and faster deleptonization time scales compared to 1D simulations. With these conditions, they saw enhanced neutrino mean energies and luminosities and smaller proto neutron stars.

However, Buras et al. (2006b) found in their 2D simulations with a sophisticated neutrino transport and simulating the whole proto neutron star, that the convective zone within the proto neutron star was well below the neutrinospheres, and that the effect of convection was – conversely – a somewhat thermally enlarged proto neutron star, with a correspondingly reduced mean energy. The larger radiating surface due the larger neutron star could not compensate this effect, the neutrino luminosities were found to be smaller than in corresponding spherically symmetric simulations. Only later, the enhanced energy transport via convection within the deeper layers of the proto neutron stars led to an enhancement of the heavy lepton neutrino luminosities, who are created further in at higher densities than the electron flavor species.

The accretion signal of spherically symmetric simulations (without any convection treatment) was most recently analysed by O’Connor and Ott (2013), who used a comparably approximative neutrino transfer scheme in order to study the pre-explosion accretion neutrino signal for a very wide range of progenitor models.

They claimed that one might infer some constraints on the high density equation of state out of the neutrino signal. Partly, a motivation for the study in this chapter was to check whether these still hold when applying the much more sophisticated and detailed neutrino treatment outlined in Section 2.3. The early signal of the first few 100ms of the accretion phase is interesting also, as it could possibly allow one to determine the neutrino mass hierarchy, confer to Serpico et al. (2012), in which a number of the models produced for this chapter with the LS180 equation of state were used. The effect exploited there depends on the universal behaviour of the first few 50-100ms, which had to be checked for other high density equation of states and progenitors. Next to that, the aim was also to prepare a number of suitably evolved initial models for the proto neutron star cooling models used in Chapter 5.

3.1 Models

The presupernova progenitors are a selection of 10 models from the Woosley et al. (2002) series over a main sequence mass range of 11.2 to 40 solar masses, with the addition of model s15s7b2 from Woosley and Weaver (1995) which is well studied in the literature.

For the high-density equation of state of nuclear matter, we use the tables of Lattimer and Swesty (1991 and Lattimer et al., 1985) in the $\mathsf{K} = 220\,\mathrm{MeV}$ version as well as the one from Shen et al. (1998a,b). As a test, we also show some models with the $\mathsf{K} = 180\mathrm{MeV}$ version, which was used extensively in previous studies.

Next to that, for most of these models we also did runs where the mixing-length scheme was applied in the proto neutron star as an approximation to the convection that would take place there in multi-D simulations. Models without the mixing-length scheme are labelled "eos-progenitor", with a "c" appended for those with the scheme active. The scheme introduces artificial energy and lepton fluxes within the proto neutron star (and to a very small extent also above it up to the shock radius) to mimic the multi dimensional effect of convective overturn in the unstable stratification that resulting from neutrino cooling, see Section 2.4. Although a mixing length description is not directly applicable to the dynamic accretion flow above the proto neutron star's surface, the scheme was still also applied there as it had little influence on the stratification outside of the proto neutron star itself and we could thus avoid choosing an arbitrary point up to which the convective fluxes were to be applied.

For the most and least massive progenitor (s11.2 and s40.0), we also ran a number of additional simulations. In one set we took the tabulated progenitor's pressure instead of its temperature as initial variable to setup our models (s11.2pre, s40.0pre). Next to that we made additional runs with a changed setup of the high-density / low-density equation of state partition and electron capture treatment (s11.2ec), explored in Section 3.2.1.

Due to problem with our neutrino opacities, for a selected number of progenitors we also did simulations with a different, improved treatment of the effect of the nucleon potentials on the neutrino opacities, see Section 3.4.6.

We evolved all models to a time $0.5s$ after the moment of core-bounce, defined as the moment the matter right behind the accretion shock first reaches an entropy of $3k_B$ per baryon.

3.2 Collapse

The baryonic mass enclosed by the shock formation radius at core bounce is only weakly dependent on the initial profile, it is more so a function of the high density equation of state and their composition and their influence on the deleptonization during collapse, (see also Marek, 2007, for more details). In Figure 3.1 this effect is shown for our model set, for an even larger set of progenitors using the LS180

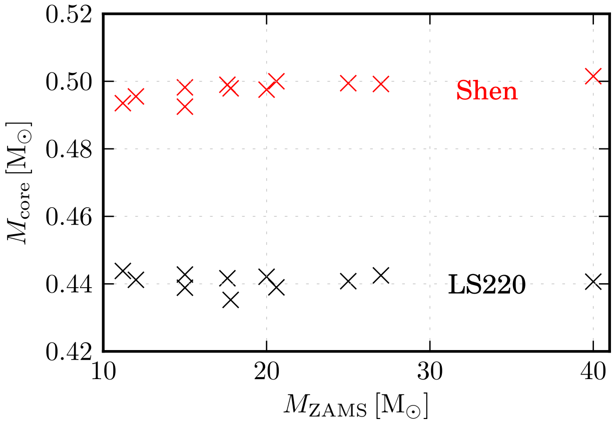

Figure 3.1: Enclosed mass by the radius of shock formation at the moment of core-bounce, which is predominantly a function of the high density EoS only.

Table 3.1: A selection of quantities at the moment of core-bounce, the compactness parameter $\zeta_{2.5}$, the radius (r_{sh}) and enclosed mass (M_{sh}) of the shock at the moment of core-bounce, and the collapse duration t_{col}. Note that the mixing-length treatment is not applied until a proto neutron star is formed, the collapse of the mixing-length models is therefore identical to the models shown here. Models “pre” use the progenitor pressure as input variable.

Model		LS220			Shen		
	$\zeta_{2.5}$ [1]	r_{sh} [km]	M_{sh} [M$_\odot$]	t_{col} [s]	r_{sh} [km]	M_{sh} [M$_\odot$]	t_{col} [s]
s11.2	0.01	11.43	0.444	0.170	12.04	0.494	0.137
s11.2ec	−”−	11.24	0.451	0.126	12.05	0.493	0.127
s11.2pre	−”−	11.43	0.444	0.169	12.10	0.488	0.166
s12.0	0.02	11.36	0.441	0.187	12.06	0.496	0.144
s15.0	0.15	11.19	0.443	0.304	12.02	0.498	0.211
s15s7b2	0.09	11.34	0.439	0.221	12.08	0.493	0.168
s17.6	0.17	11.18	0.442	0.285	12.04	0.499	0.199
s17.8	0.21	11.24	0.435	0.279	12.03	0.498	0.190
s20.0	0.13	11.20	0.442	0.257	12.06	0.498	0.188
s20.6	0.28	11.15	0.439	0.413	12.05	0.500	0.255
s25.0	0.32	11.17	0.441	0.455	12.06	0.499	0.276
s27.0	0.23	11.18	0.443	0.345	12.03	0.499	0.227
s40.0	0.26	11.15	0.441	0.409	12.09	0.502	0.254
s40.0pre	−”−	11.18	0.447	0.317	12.13	0.497	0.309

and Shen high density EoS see also Figures 6 and 7 of Janka et al. (2012) we could contribute while working on this chapter.

A list of all models and their configuration at core-bounce can be found in Table 3.1, where we show the radius of the shock, its enclosed mass, and the compactness parameter of the progenitor following the definition of O'Connor and Ott (2013),

$$\zeta_M = \frac{M}{r(M_{\mathrm{enc}} = M)} \Big/ \frac{1 M_\odot}{1000\mathrm{km}}. \tag{3.1}$$

Even though the collapse physics is understood very well, small differences in the setup can lead to a very different collapse duration. As can be seen in the table, the choice of a different high density equation of state has a big impact on the collapse duration, although they should give identical behaviour for the low-densities that are involved - the central density approaches high densities only in a very short phase at the end of collapse.

One can only infer that one or both of the high density equations of state reproduce the low-density limit only poorly, despite the fact that that the physics there is completely known. (Recall that in our simulations we also use a dedicated low-density equation of state for a Boltzmann gas plus radiation, typically for densities lower than $\sim 10^7 - 10^8\,\mathrm{g/cm^3}$ during collapse)

Another factor is the choice of input variables to use from the progenitor models by Woosley et al. (2002) in order to start our own simulations. Typically we use density, *temperature*, and composition as tabulated in their models. Due to differences with the equation of state that has been used for their modelling, this is unfortunately not identical to other choices such as density, *pressure*, and composition, which would better reproduce the hydrodynamical state of the stratification. To determine the influence of these inconsistencies, we also ran models where we set the temperature in such a way as to reproduce the initial pressure profile and ran calculations for the two extreme progenitors s11.2 and s40.0 of our set. The collapse duration of models ls220-s11.2 and ls220-s11.2-pre is almost identical, whereas model ls220-s40.0-pre has a more than 20% faster collapse than its counterpart where the temperature was used as initial variable.

These discrepancies are of course very unsatisfactory and leave us with the decision of which variables to reproduce better, it would be desirable to have a closer match of the high density models to the low density limit and avoid this mishap.

All models employing the Shen equation of state consistently show a much shorter collapse time than their corresponding LS220 models. As the collapse time is dominated by low density behaviour, this surprising effect must be due to different low-density limits of the two high density EoS. With (ρ, p, X_i) as input values, the collapse time-scale is much more similar to the LS220 case.

It seems to be desirable to use our low-density equation of state - which is in rather good agreement with the tabulated thermodynamic quantities of the progenitor data given to us - up to much larger densities than in our previous simulations.

3.2.1 Influence of electron capture details

The collapse is initiated by increasingly rapid electron captures on nuclei and protons. Unfortunately, due to the way our electron-capture rates on nuclei were implemented in the past (only in the high density, NSE region) we used the high density EoS tables during the gravitational collapse down to densities of $\sim 10^7 - 10^8\,\mathrm{g/cm^3}$, and the time till collapse was in that way influenced by the their rather poor low-density limits.

The reason behind this was, that we only model the composition of the star as a set of α-Nuclei, the corresponding daughter nuclei needed for electron captures are therefore not available. In NSE, electron captures could be computed with the present composition and the resulting change in Y_e was used the update the fraction of all nuclei according to the new equilibrium composition.

To judge the influence of the low density physics on the collapse time, we also did two test simulations, ls220-s11.2ec and shen-s11.2ec, where the high density equation of state was used during collapse also only for densities above $10^{11}\mathrm{g/cm^3}$. Again, pressure was used as input quantity instead of temperature. To augment our low density EoS for NSE conditions, an additional 23-species NSE composition table was used in the extended low density regime for temperatures above 0.5MeV – the same setup we usually use post-bounce in our simulations.

The region enclosed by $T = 0.5\mathrm{MeV}$ is slightly different than the regime of $\rho \gtrsim 10^7 - 10^8\mathrm{g/cm^3}$, where the high density equation of state was used previously, see also the discussion in Marek (2007). Therefore, we simply calculated the rate of electron captures everywhere in the model, with the rates according to Langanke et al. (2003). Their electron capture prescription is calculated as a mean rate for a large ensemble of nuclei (also assumed to be in NSE) and is thus not directly applicable to individual nuclei anyway.

Outside the NSE regime, we therefore ignore any change in composition but track only the change in Y_e, resulting in a slight charge violation. As the relevant input quantities for the electron capture rates are only (ρ, T, Y_e) and not the detailed composition, the electron capture rates are therefore not affected by that. Also, most matter taking part in the collapse is in fact in NSE already or quickly heated up sufficiently enough, we find that the charge conservation violation is never more than a $\sim 1\%$ deviation of the nuclear charge number to electron number. The violation vanishes completely as soon as the matter enters the dedicated NSE region, where the composition is again adjusted consistently to the advected Y_e.

With this improved setup the collapse time scale is now only very weakly dependent on the high density equation of state, looking into the models in detail we find that the remaining difference is in fact a result of the very last milliseconds of collapse where the densities in the core start to rise significantly into the high density regime.

Compared to the standard treatment the collapse is shorter than it was before, with $\sim$ 126ms compared to the $\sim$ 170ms of the models ls220-s11.2pre and shen-s11.2pre.

This all might seem pedantic, but it must be emphasized that any change in the collapse duration is reflected in a change of the time evolution of the mass accretion rate after core-bounce. As the neutrino signal is a composite of a core and accretion part, the first of which if mostly fixed relative to the moment of core-bounce, the relative shift of a different collapse time will influence the resulting neutrino signal due to the different accretion rate. This might be especially relevant for multidimensional simulations, where the relative time evolution of the mass accretion rate, influenced e.g. by the infall of a shell of the onion structure of the progenitor through the accretion shock, might make the difference between an exploding and non exploding model.

3.3 Proto Neutron Star Convection

A spherically symmetric composition and density stratification is stable against small perturbations if the Ledoux criterion,

$$C_{\mathrm{led}} = \left(\frac{\partial\rho}{\partial s}\right)_{Y,p} \frac{\mathrm{d}s}{\mathrm{d}r} + \left(\frac{\partial\rho}{\partial Y}\right)_{s,p} \frac{\mathrm{d}Y}{\mathrm{d}r} = \frac{\mathrm{d}\rho}{\mathrm{d}r} - \frac{1}{c_s^2}\frac{\mathrm{d}p}{\mathrm{d}r} < 0 \qquad (3.2)$$

is met, where c_s is the speed of sound in the medium. If not, fluid elements from the bottom of the unstable region will rise up and elements from the top will sink down. In a mixing-length description, this multidimensional effect is modelled via additional energy and composition/lepton number fluxes that drive the profile into a configuration with $C_{\mathrm{led}} \lesssim 0$, for details of our scheme, see Section 2.4.

3.3.1 Comparison with a Multidimensional Model

In order to evaluate the soundness of such an admittedly rather simple treatment of multi dimensional convection, we compare the resulting neutrino luminosities and the shock-radius with results from an axissymmetric ("2D") simulation, kindly provided to us by Florian Hanke, cf. Figure 3.2.

As it is difficult to locate the convectively unstable regions in a simulation where we employ the mixing length scheme - the scheme by construction drives any unstable regions to a stable configuration - we take one of our simulations without the mixing length scheme for the comparison in the upper panel of Figure 3.2, on the lower panels, also the simulations with the mixing length scheme are shown.

Two distinct unstable regions can be discerned. Shortly after bounce the proton neutron star experiences a short-lived "prompt" convection, and only later the negative entropy gradient due to neutrino cooling in the outer layers of the proto neutron star results in what usually is called the proto neutron star convection.

The precise extent of the unstable region is dependent on the high density equation of state, in the Shen models it develops a bit earlier ($\sim$ 50 ms after bounce) than in the LS220 models ($\sim$ 70 ms).

It can be seen that the proto neutron star convection in the 2D model – marked in that plot by genuine lateral motions – is not too far off of the region where the pure 1D model displays convective instability. The 2D model naturally also shows heavy lateral activity above the proto neutron star - it eventually even explodes - which of course cannot be modelled with our ansatz, which is meant only to give a more accurate description of the proto neutron star convection itself, not the flow in the accretion layer above it. There, mixing length is certainly not a good prescription any more, as that theory is based on a quasi-hydrostatic background configuration, an assumption that is not valid in the fast accretion flow in the post-shock region. Even tough, we still apply the mixing length scheme throughout the whole post-shock region, this is done mostly for simplicity of implementation than for physical influence, as it hardly affects the stratification of the heating layer in our simulations. That way we do not have to choose an arbitrary boundary up to which to apply the mixing length scheme to encompass all of the proto neutron star convection.

The proto neutron star's radius (defined as the density contour of $10^{11}\mathrm{g/cm^3}$) is larger in the multidimensional simulation, as energy is transported outwards to lower densities by the convective motions, where it can act as additional pressure support. With the mixing length ansatz we find neutron star radii that are much more similar to the 2D simulation. Directly connected to this is the better match of the heavy lepton neutrino luminosity of the convective run compared to the multidimensional case, as the main source of those neutrinos is the proto neutron star itself. The electron flavor luminosities are more strongly produced also by the accretion flow, which quickly gets non-spherical in multidimensional simulations - therefore the mixing length scheme can only improve the part of the luminosity originating from the core, as can be seen by the poorer match to the multidimensional values.

In Figure 3.3, we show profiles of temperature, entropy and electron fraction for a standard 1D model, a 1D model with the mixing length scheme and angle-averaged profiles of the 2D models, for two different snapshots in time. We use the matter density as a radial coordinate in this figure, as firstly the proto neutron stars in the three simulations have a different radius and secondly density and temperature are the most relevant quantities for the neutrino opacities. One can see both that the pure 1D model exhibits very different gradients than the multidimensional model and that the simulation with the mixing length scheme is able to approximate the true gradients.

In Figure 3.4, profiles of the neutrino luminosity and number flux are shown for one particular moment in time. It is visible how the scheme increases the electron neutrino luminosity behind the unstable region, corresponding to the increased lepton number transport from the mixing length fluxes, as we saw from the left panel of Figure 3.3. At the same time, this reduces the anti-electron neutrino production: Due to the increased electron degeneracy the positron fraction necessary for charged current reactions is quenched and the increased electron neutrino density results in final-state blocking for $\nu_e\bar{\nu}_e$ creation in neutral current reactions.

At lower densities, stronger deviation from the mixing-length and truly multidimensional model appear, due to the strong lateral motions in the accretion layer.

However, the primary aim of our mixing length scheme is to better reproduce the proto neutron star convection for the cooling simulations we will attempt in Chapter 5. There, the accretion layer has been blown away by the explosion and lateral motions are indeed only found within the proto neutron star convection zone.

3.3.2 Comparison with Standard 1D models

For the two extreme cases in our set of progenitors, we look at the differential effect of the convection treatment in a bit more detail, now by comparing with the respective spherical symmetric simulations without the mixing length scheme.

Proto Neutron Star and Shock Radii

In the upper panels of Figure 3.5, it is visible that the convection treatment reduces the size of the neutron star (and consequently the shock radius) right after bounce, whereas 100 to 200ms later it actually increases its radius, as mentioned in the previous section. Janka et al. (2012) give an analytical expression for the shock radius as a function of mass accretion rate $\dot{M}$, neutron star radius r_{pns}, and the electron flavor neutrino luminosity L_ν and mean square neutrino energy $\left\langle \varepsilon_\nu^2 \right\rangle$ as

$$r_{\mathrm{sh}} \propto \frac{\left(L_\nu \left\langle \varepsilon_\nu^2 \right\rangle\right)^{4/9} r_{\mathrm{pns}}^{16/9}}{\dot{M}^{2/3} M_{\mathrm{pns}}^{1/3}}, \tag{3.3}$$

which is in nice agreement with the observed radii of our hydrodynamical models, for the late, quasi-static phase. With this, we can see that the difference in shock radius between normal and convective models is predominantly due to the different proto neutron star's radii, with only minor corrections due to the counter-acting effects of the higher luminosities and lower mean energies. (The mass accretion rate and proto neutron star mass are of course identical between models with the same progenitor, at least up to deviations within at most an advection time-scale of the post-shock layer)

Effect on Neutrino Signal

In the lower panels of Figure 3.5 the effect of the convection treatment on the neutrino signal is shown. The electron neutrino luminosity seems largely unaffected, generally increased to a very low extent. The anti-electron neutrino luminosity is somewhat suppressed compared to the non-mixing simulations at early times when the mass accretion rate is still higher. Later it is more similar and even slightly above the unmixed case again. The largest effect is visible in the heavy lepton flavors, the luminosity is noticeably enhanced due to the convection treatment - as all neutrinospheres are well outside the convective region, this is a result of the larger photosphere due to the larger proton neutron stars of the convective models and not immediately related to the energy transport by the convection

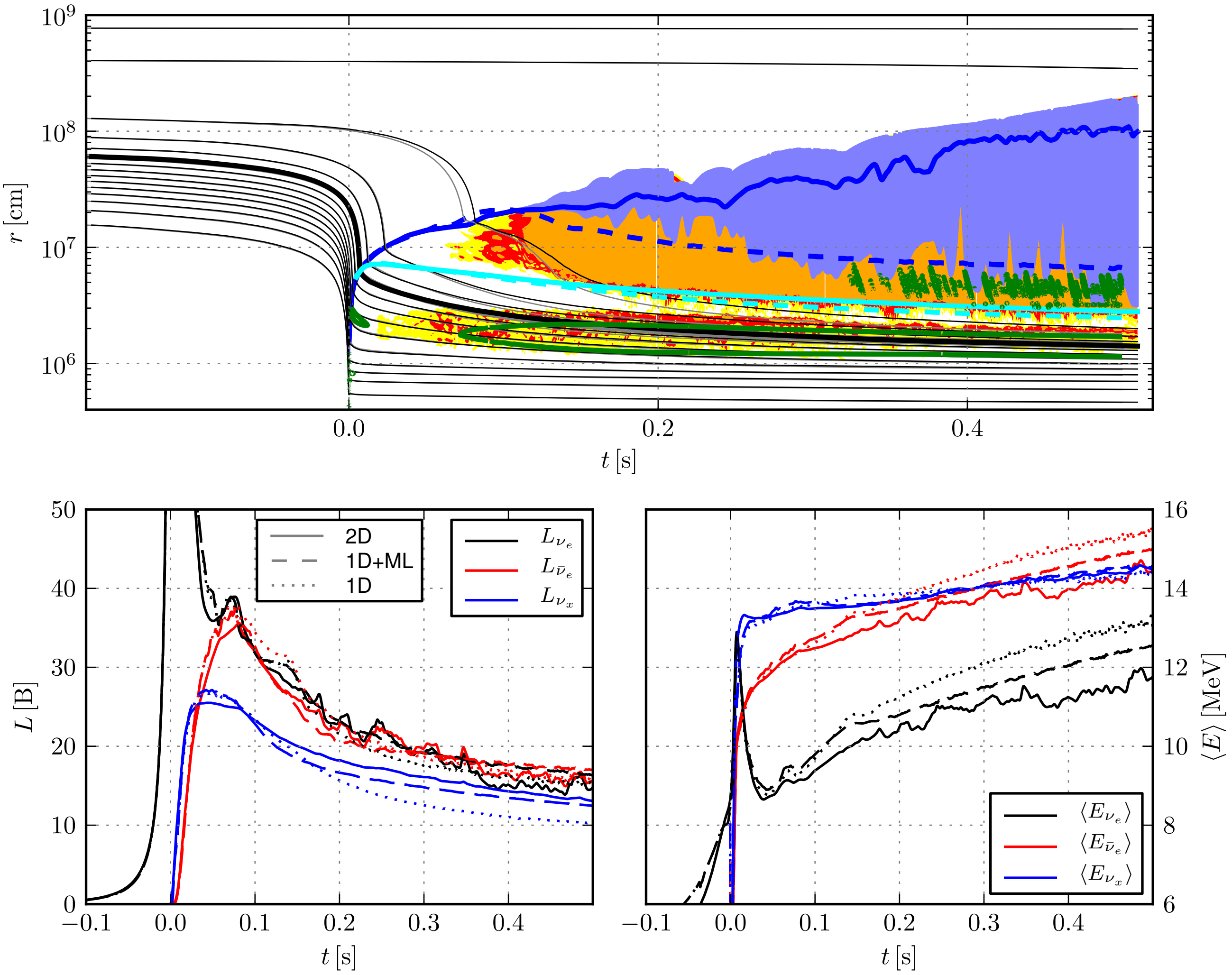

Figure 3.2: On the *upper* panel one can see mass shells of a 1D (grey) and 2D model (black) of an 11.2 solar mass star. The blue solid line is the mean value of the shock radius of the 2D simulations, the region between the minimal and maximal shock region is filled in blue, the blue dashed line is the shock radius of the 1D model. The cyan line marks the neutron star radius, solid for 2D, dashed for the 1D model. Contoured in yellow, red, and orange are regions of the 2D model with lateral velocities larger than 1000, 2000, and 3000 km/s, respectively, as an indicator for the regions of convective activity. The area enclosed by the solid green line is the region where the 1D models shows convectively unstable gradients and where the mixing length scheme would be active. The *lower left* and *lower right* panel show the luminosity and (angle averaged) mean energy of the 2D model (solid), the 1D model with (dashed), and the model without (dotted) the mixing length scheme.

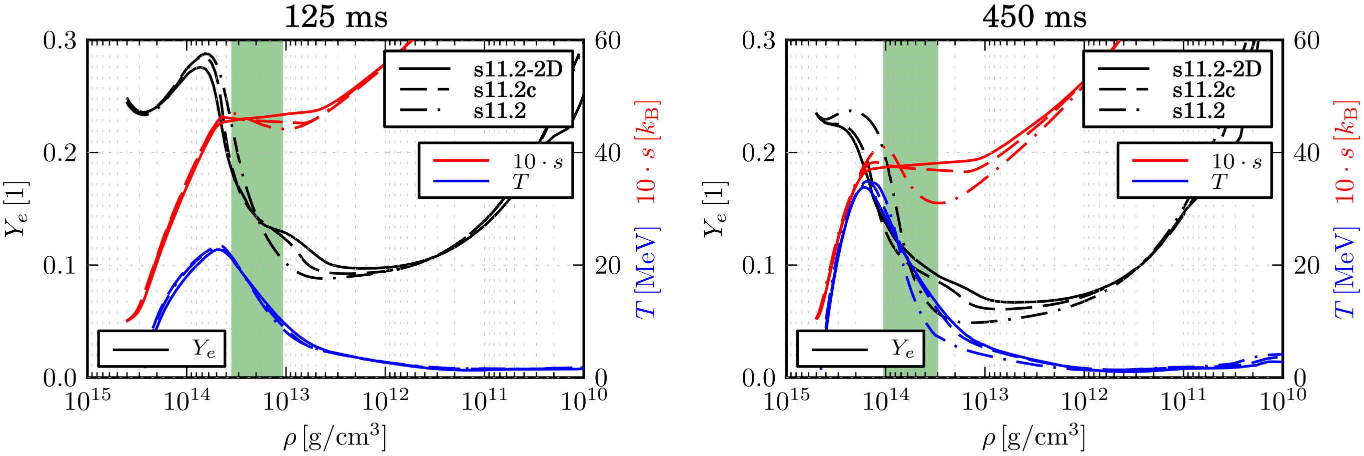

Figure 3.3: Profiles of the electron fraction, entropy, and medium temperature, for a 2D, 1D convective and normal model, all with the LS220 EoS, using the density as a radial coordinate. The 2D curves of entropy and electron fraction are simple mass weighted angular averages, the temperature was calculated by mass-averaging the energy and calculating the temperature via the equation of state, using additionally the averaged electron fraction and a mean density as remaining state variables. Shown are two snapshots at 125 (*left*) and 450ms (*right*) post bounce. The region of convective instability for the standard 1D model ls220-s11.2 is marked in green.

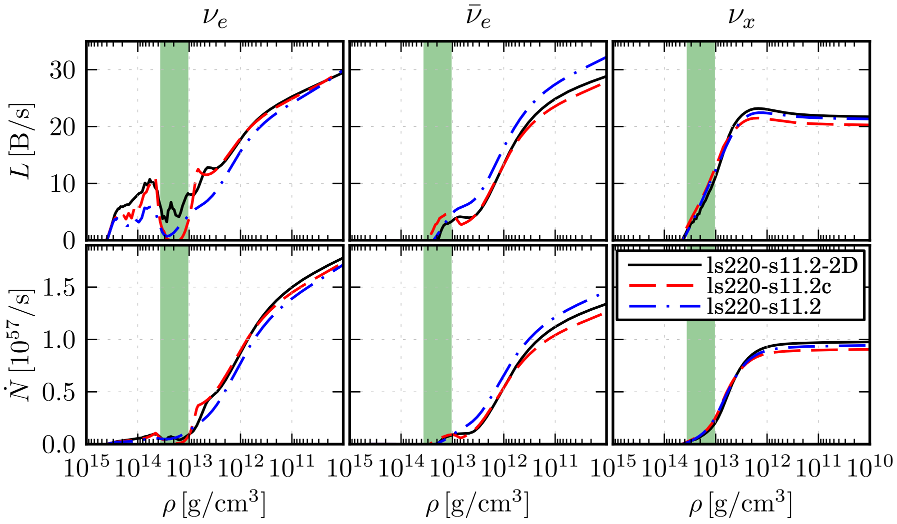

Figure 3.4: Profiles of an axially symmetric and two spherically models with and without the mixing length scheme, 125ms after core bounce. Shown are the neutrino luminosity (*upper panels*) and the neutrino number flux (*lower panels*), for each of the three different neutrino species. Marked in green is the region of convective instability for the nonconvective 1D model.

itself. Their mean energies (Eq. 3.4) in contrast are almost unchanged and only slightly reduced at late times in the convective models whereas they are clearly enhanced for both the electron neutrino species. Despite initially higher mean energies at the edge of the convection region where thermal energy from the hotter region below is transported upwards, the neutrinos still end up with lower mean energies when they decouple. As they are still in thermal equilibrium with the matter outside of the convective region, their mean energies are then determined by the temperature of matter further out at lower densities. There, the larger proto neutron star radii in the convective models result in slightly colder matter from the accretion flow - resulting in lower mean energy neutrinos – albeit of course with a higher luminosity. This effect has already been observed by Buras et al. (2006a) in truly multidimensional (2D) simulations. Recall also Figure 3.3 for the changed hydrodynamical profiles due to the convective fluxes for the ls220-s11.2 case.

3.3.3 Full Model Set

In Figure 3.6, we show the radius of the shock and the proto neutron star, as well as the mass accretion rate of the infalling matter from the progenitor for all our models with convection treatment. The evolution of the shock radius varies with the progenitor owing to different mass accretion rates due to a different density stratification in the infalling layers. A number of models show a typical up- and down-rising of the shock which can be identified with the passing of a layer of the onion-shell burning structure from the progenitor, an accompanied drop in the mass accretion rate can be observed in the lowermost panel of Figure 3.6 resulting in the shock expansion and contraction, cf. Eq. (3.3).

The neutron star radii show a much smaller variation, as the collapsing iron core of which it was formed initially always has a similar mass on the order of the Chandrasekhar mass M_{ch}, and the radius of a neutron star is only very weakly dependent on the mass around M_{ch}. At the end of the simulations, all models using the LS220 have a neutron star radius of $25-27$km, whereas the stiffer Shen EoS result in radii of ~ 31km, in Tables 3.2 and 3.3 the last values at 500ms after core bounce of the proto neutron star configuration and neutrino signal are given for all models.

3.4 Neutrino Signal

For an overview of the resulting neutrino signal from all models consult Figure 3.7, where we show luminosities and mean energies. We define the mean energies as total neutrino energy density J over number density $\mathcal{J}$, or in terms of the neutrino intensity $\mathcal{I}$ as

$$\langle \varepsilon^1 \rangle = \frac{\int J \, d\varepsilon}{\int \mathcal{J} \, d\varepsilon} = \frac{\int_0^\infty d\varepsilon \int_{-1}^1 d\mu \, \mathcal{I}(\varepsilon, \mu)}{\int_0^\infty d\varepsilon \int_{-1}^1 d\mu \, \varepsilon^{-1} \mathcal{I}(\varepsilon, \mu)}. \tag{3.4}$$

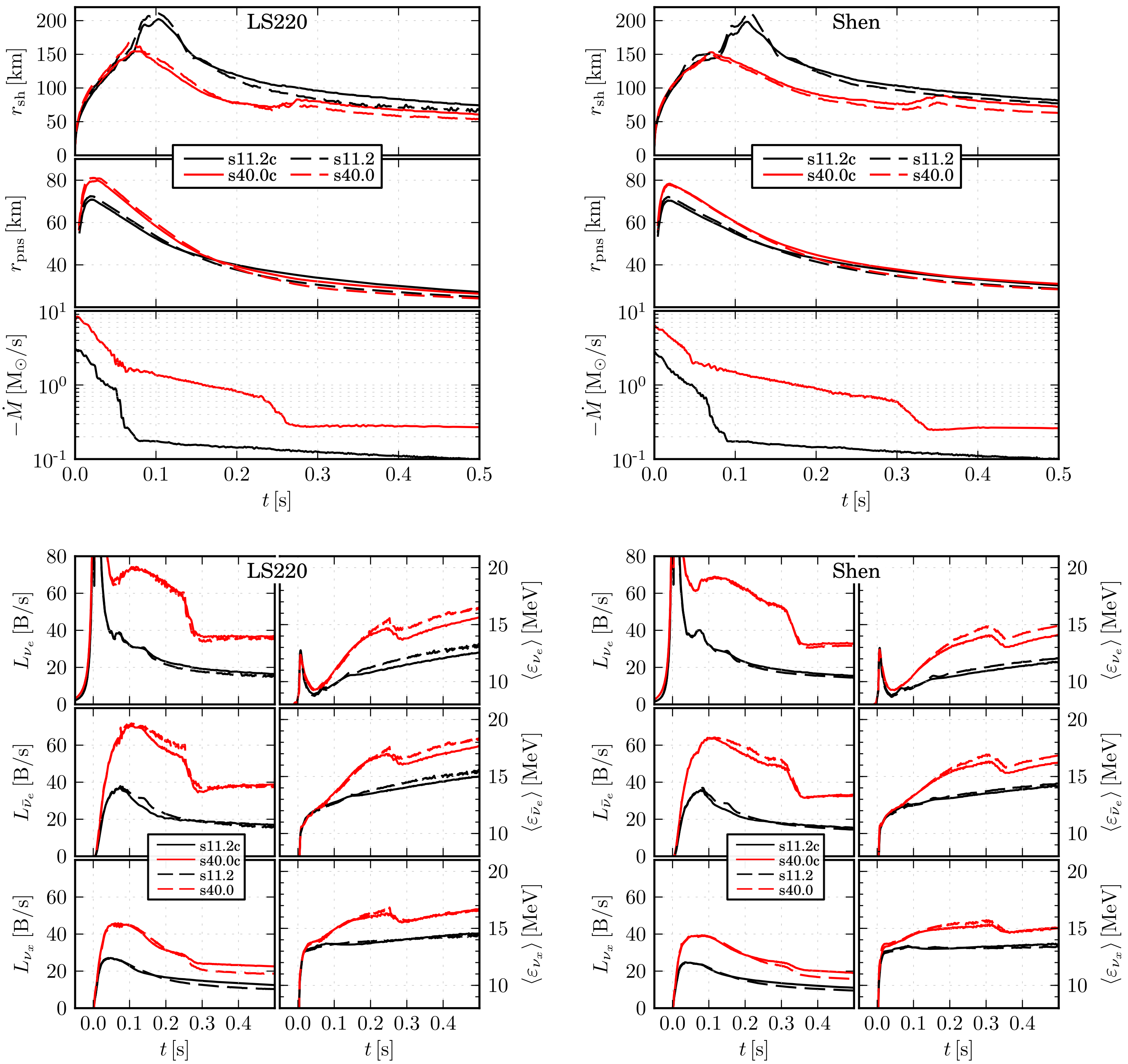

Figure 3.5: Comparison of models s11.2 and s40.0 with and without the mixing length scheme active. The upper panels show the dynamical evolution of the proto neutron star and shock radius, the lower panels show the resulting neutrino signal evaluated at 500km and transformed to a resting observer's frame, including the (small) effect of gravitational redshift.

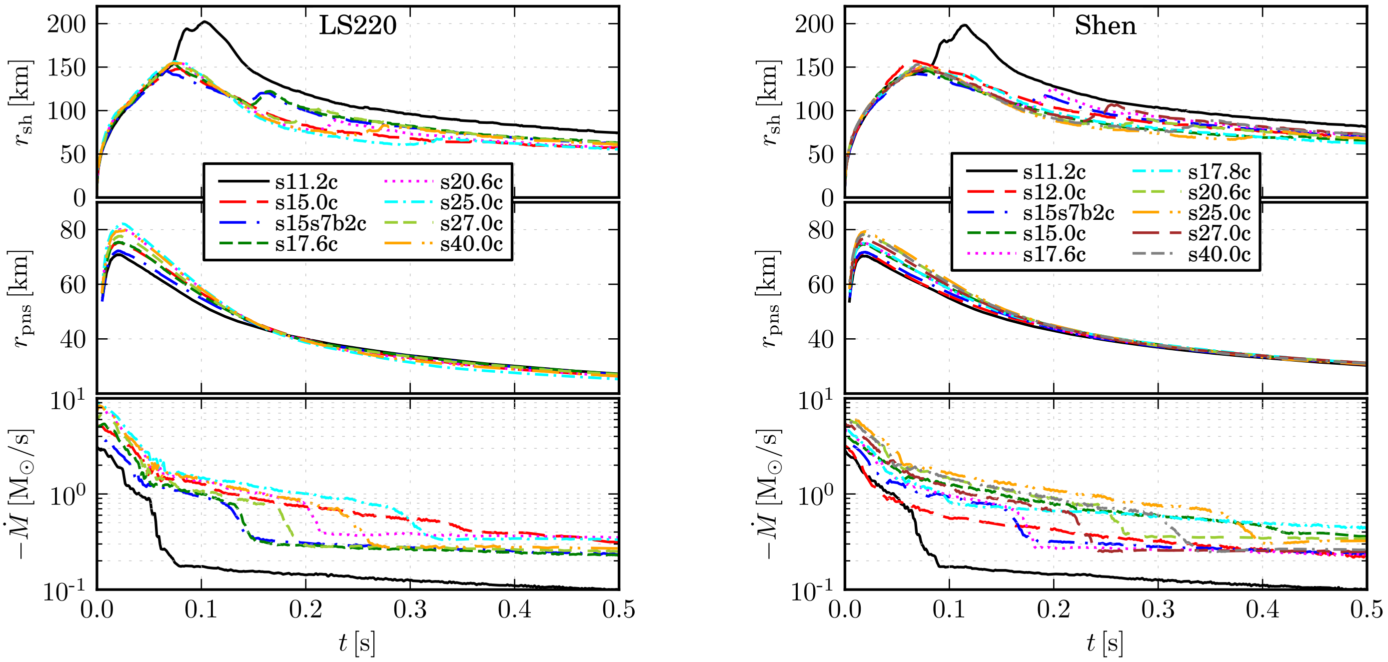

Figure 3.6: Shock radius, proto neutron star radius, and the mass accretion rate evaluated at 500km, from top to bottom. Note the correspondence of the expansion of the shock radius with a drop in the mass accretion rate

3.4.1 Luminosity Minimum before Neutronization Burst

A curious feature seen in most simulations of sufficient sophistication is a short-lived local maximum of the electron neutrino luminosity before the actual moment of core bounce and the prominent high energy deleptonization burst. It is actually rather difficult to discern in plots showing the whole time evolution, as it last only a couple of milliseconds. In a suitable closeup in Figure 3.8 it can be seen that this pre-bounce maximum is originating from a semi-transparent region of $\sim 10^{11}\mathrm{g/cm^3}$ in density at $\sim 100\mathrm{km}$. This emission is then quenched during the final phase of the stellar collapse, when the increasingly negative velocity results in 1) a considerable redshift and 2) makes it at the same time more difficult for the semi-trapped neutrinos to diffuse outwards against the matter flow. This might explain why this feature is very different or absent in simulations omitting velocity-dependent terms (e.g. the results of O'Connor and Ott, 2013). After bounce when the velocities have stalled one can observe the usual shock breakout burst.

3.4.2 Core and Accretion Luminosity

The two energy sources for neutrinos are the contraction of the proto neutron star and the energy that is released by the accretion flow on its way down into the

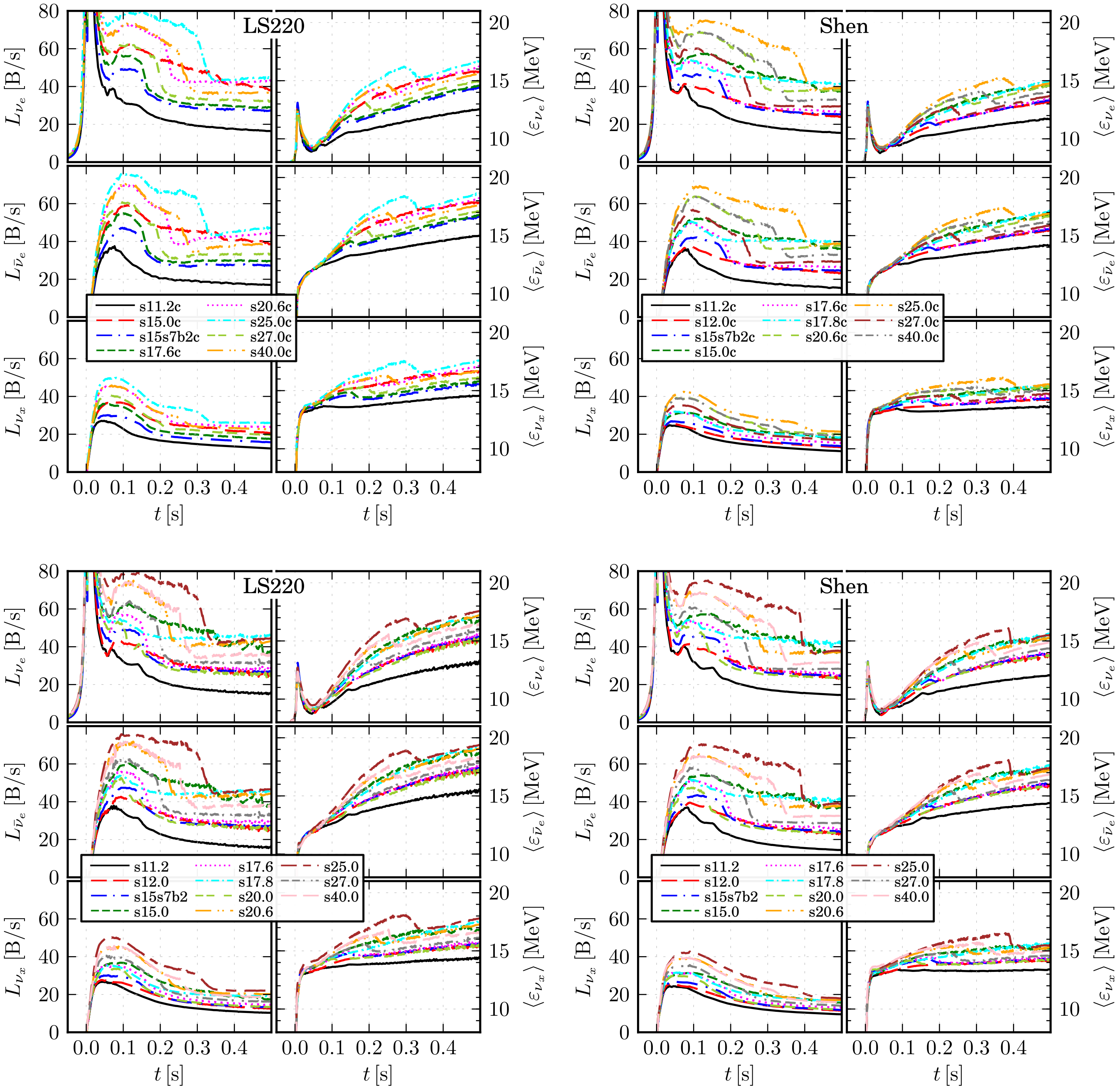

Figure 3.7: Neutrino quantities for all models, the set with the LS220 EoS on the *left*, the Shen EoS set on the *right*. Convective models are shown in the *upper*, the non-convective in the *lower* panels. Note the very generic signal of the $\bar{\nu}_e$ and ν_x mean energies in the first 100ms, which is also visible in the luminosities - except for an overall scale factor per progenitor.

Table 3.2: Proto neutron star radii and masses, and the neutrino signal, mean energies, pinching parameters and number flux, at the end of the simulations, 0.5s after core bounce. Note that the number flux of the heavy lepton neutrinos is a representative flux for one of the four subtypes.

Model	LS220										
	r_{pns}	M_{pns}	$\langle\varepsilon\rangle_{\nu_e}$	$\langle\varepsilon\rangle_{\bar{\nu}_e}$	$\langle\varepsilon\rangle_{\nu_x}$	p_{ν_e}	$p_{\bar{\nu}_e}$	p_{ν_x}	$\dot{N}_{\nu_e}$	$\dot{N}_{\bar{\nu}_e}$	$\dot{N}_{\nu_x}$
	[km]	[$M_\odot$]	[MeV]			[1]			[10^{57}/s]		
s11.2	24.8	1.357	13.0	15.3	14.3	0.98	0.95	0.99	0.71	0.63	0.44
s11.2c	27.2	1.356	12.6	15.0	14.6	0.97	0.94	0.98	0.81	0.71	0.53
s12.0	24.5	1.480	15.2	17.3	15.4	0.95	0.93	0.98	1.05	0.94	0.51
s15.0	23.8	1.768	16.8	18.7	16.8	0.99	0.98	1.05	1.40	1.28	0.65
s15.0c	26.3	1.768	15.8	17.8	16.6	0.95	0.93	0.98	1.50	1.34	0.77
s15s7b2	24.4	1.525	15.4	17.4	15.6	0.96	0.94	0.99	1.09	0.97	0.53
s15s7b2c	27.0	1.524	14.4	16.6	15.5	0.96	0.93	0.98	1.18	1.02	0.63
s17.6	24.6	1.640	15.5	17.5	15.7	0.96	0.94	0.99	1.14	1.04	0.58
s17.6c	27.1	1.640	14.6	16.8	15.7	0.96	0.94	0.98	1.24	1.11	0.69
s17.8	24.3	1.703	17.2	19.2	17.6	0.98	0.97	1.06	1.67	1.49	0.68
s20.0	24.7	1.561	15.1	17.1	15.4	1.02	0.99	1.05	1.13	1.03	0.59
s20.6	24.0	1.907	17.2	19.1	17.3	0.99	0.98	1.05	1.56	1.45	0.73
s20.6c	26.3	1.906	16.2	18.2	17.1	0.94	0.92	0.98	1.65	1.52	0.87
s25.0	23.0	2.032	17.6	19.4	17.8	0.99	0.98	1.05	1.58	1.50	0.77
s25.0c	25.3	2.032	16.7	18.6	17.6	0.94	0.93	0.98	1.68	1.58	0.92
s27.0	24.5	1.753	16.0	17.9	16.1	0.96	0.94	0.99	1.24	1.16	0.63
s27.0c	27.0	1.752	15.0	17.1	16.1	0.96	0.93	0.98	1.35	1.21	0.76
s40.0	24.1	1.904	16.4	18.3	16.6	0.95	0.93	0.98	1.35	1.28	0.70
s40.0c	26.3	1.903	15.6	17.7	16.7	0.95	0.93	0.98	1.47	1.37	0.84

potential well. While the contraction and cooling of the proto neutron star is a slow process that happens on a timescale of a few seconds and is governed by high density matter and neutrino physics, the accretion flow shows a short-timescale, progenitor structure dependent variation and is due to emission at the proto neutron star's surface at comparably low density. For analytical considerations it might be nice to have an idea about the distribution of the neutrino luminosity between these two energy sources.

Matter that is accreted onto the proto neutron star will deposit energy with a rate that is roughly proportional to

$$E_{\text{acc}} = \frac{G M_{\text{pns}} \dot{M}}{R_{\text{pns}}}. \tag{3.5}$$

The total radiated luminosity is the sum of the luminosity emitted by the cooling

Table 3.3: Same as Table 3.2 for the Shen models.

Model	Shen										
	r_{pns}	M_{pns}	$\langle\varepsilon\rangle_{\nu_e}$	$\langle\varepsilon\rangle_{\bar{\nu}_e}$	$\langle\varepsilon\rangle_{\nu_x}$	p_{ν_e}	$p_{\bar{\nu}_e}$	p_{ν_x}	$\dot{N}_{\nu_e}$	$\dot{N}_{\bar{\nu}_e}$	$\dot{N}_{\nu_x}$
	[km]	[$M_\odot$]	[MeV]			[1]			[10^{57}/s]		
s11.2	28.7	1.354	12.0	14.4	13.4	0.97	0.94	0.98	0.75	0.62	0.44
s11.2c	30.3	1.354	11.7	14.2	13.6	0.97	0.94	0.98	0.82	0.68	0.50
s12.0	28.8	1.475	13.5	15.6	14.1	0.97	0.94	0.99	1.02	0.87	0.50
s12.0c	30.6	1.474	13.2	15.5	14.3	0.96	0.93	0.98	1.13	0.94	0.57
s15.0	29.0	1.744	15.4	17.3	15.3	0.95	0.93	0.99	1.55	1.36	0.65
s15.0c	30.9	1.744	14.6	16.8	15.3	0.95	0.93	0.98	1.60	1.34	0.73
s15s7b2	28.6	1.517	13.9	16.0	14.2	0.96	0.94	0.99	1.09	0.93	0.52
s15s7b2c	30.7	1.516	13.4	15.6	14.4	0.96	0.94	0.98	1.18	0.99	0.60
s17.6	29.0	1.628	13.9	16.0	14.3	0.97	0.94	0.99	1.14	1.00	0.56
s17.6c	31.1	1.628	13.5	15.7	14.6	0.97	0.94	0.98	1.24	1.06	0.66
s17.8	29.2	1.719	15.6	17.6	15.7	0.95	0.93	0.99	1.67	1.44	0.66
s17.8c	31.1	1.719	15.0	17.1	15.5	0.94	0.92	0.98	1.73	1.45	0.74
s20.0	28.7	1.552	13.8	15.9	14.2	0.96	0.94	0.99	1.07	0.92	0.53
s20.6	29.0	1.882	15.3	17.2	15.3	0.95	0.93	0.99	1.52	1.36	0.69
s20.6c	31.2	1.881	14.6	16.7	15.4	0.95	0.93	0.98	1.62	1.42	0.81
s25.0	28.3	2.004	15.6	17.4	15.5	0.95	0.94	0.99	1.52	1.40	0.72
s25.0c	30.7	2.003	14.8	17.0	15.6	0.96	0.93	0.98	1.66	1.44	0.86
s27.0	28.9	1.735	14.4	16.4	14.5	0.96	0.94	0.99	1.22	1.09	0.60
s27.0c	31.2	1.735	13.7	15.9	14.8	0.96	0.94	0.98	1.34	1.15	0.72
s40.0	28.4	1.882	14.9	16.8	15.0	0.96	0.94	0.99	1.33	1.21	0.66
s40.0c	31.0	1.882	14.1	16.2	15.1	0.96	0.94	0.98	1.46	1.28	0.79

proton neutron star's core and the part due to accretion,

$$L_{\mathrm{tot}} = L_{\mathrm{core}} + L_{\mathrm{acc}}. \tag{3.6}$$

We now assume that the luminosity due to heavy lepton neutrinos is a good measure for the "core"-luminosity of all species, as these can escape the proto neutron star more easily than their electron flavor counterparts and are not as abundantly produced in the accreting post-shock layer. We thus make the following ansatz for the total luminosity,

$$L_{\mathrm{tot}} \approx L_{\alpha\zeta} = (4 + 2\alpha)L_{\nu_{\mathrm{x}}} + \zeta \frac{G M_{\mathrm{pns}} \dot{M}}{R_{\mathrm{pns}}}, \tag{3.7}$$

where the coefficient α indicates the amount of luminosity of electron (or anti-electron) neutrino emission from the core relative to those of the muon- and tau-

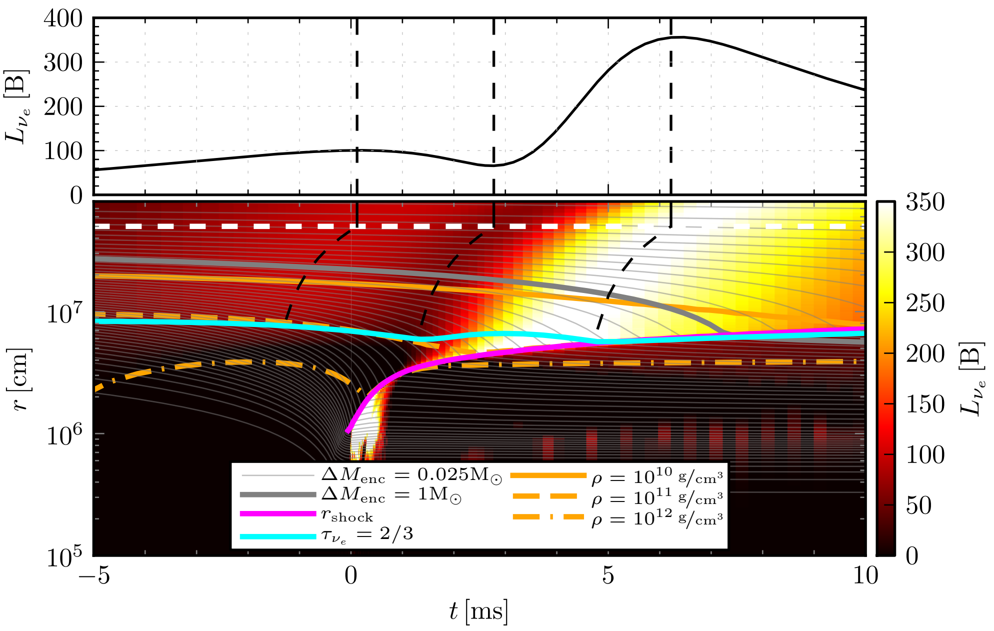

Figure 3.8: The upper panel shows the electron neutrino luminosity evaluated at 500km and transformed to the frame of a resting observer at infinity, for model ls220-s11.2. In the lower panel is a space-time diagram of the luminosity evolution a few milliseconds around the moment of core bounce. Colour coded is the local electron neutrino luminosity value. The lines give the shock radius, the neutrino sphere, certain enclosed mass values and iso-density contours, as indicated in the legend. The black dashed lines are world lines with $r = ct + t_0$, to illustrate the formation of the luminosity time evolution at 500km visible in the upper panel.

neutrinos, and ζ a conversion efficiency for the fraction of released gravitational energy that is converted into neutrino radiation.

Due to the different compactness of the resulting proto neutron star due to the different high-density equations of state, the parameters might be systematically different for models with different EoS. Therefore we do a simple least-squares fit for all models using the same EoS, using all data points for times later than 150ms post-bounce when the dynamical phase is roughly over and the systems is in a quasi-hydrostatic equilibrium as is usually assumed in theoretical models. We find that we can reproduce the total luminosity to a very good degree with our ansatz. Even when we look at the relative residual of only the electron flavor luminosity,

$$\chi = 1 - \frac{L_{e\,\rm fit}}{L_{e\,\rm sim}} = 1 - \frac{2\alpha L_{\nu_x} + \zeta E_{\rm acc}}{L_{\nu_{\rm e}} + L_{\bar{\nu}_{\rm e}}}, \tag{3.8}$$

we see a reasonably good agreement, see Figure 3.9 for a plot of this quantity for all models. We find that these values reproduce the electron flavor luminosities

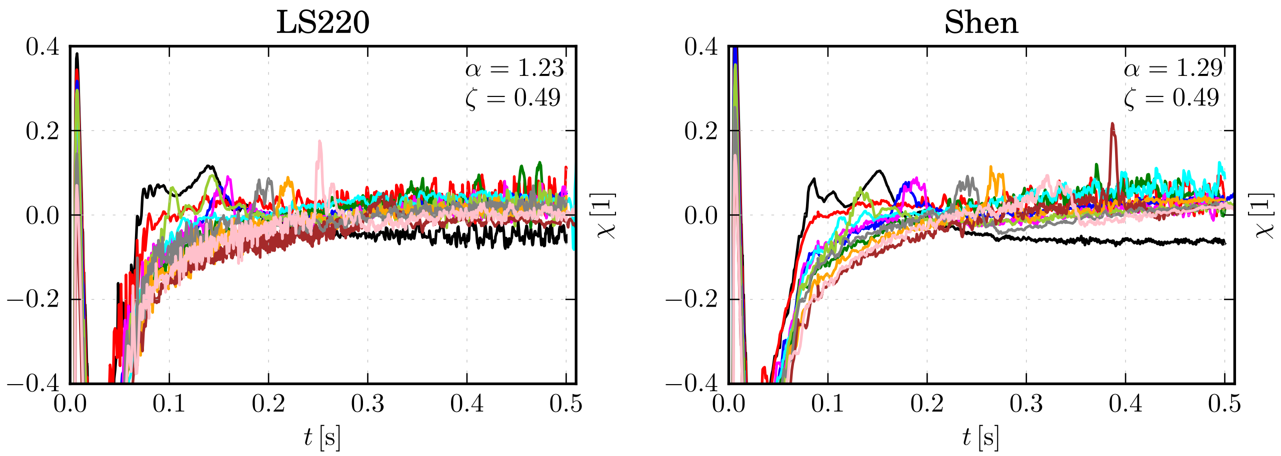

Figure 3.9: The relative residual χ from Equation (3.8), for all models.

always to better than 10% for the LS220 (and Shen) case:

$$\begin{aligned} \alpha &= 1.23\,(1.29), \\ \zeta &= 0.49\,(0.49). \end{aligned} \tag{3.9}$$

3.4.3 Mean Neutrino Energies

It is interesting to look at the rather generic signal of the mean energies of $\bar{\nu}_e$ and ν_x in the first hundred milliseconds after core bounce; in Serpico et al. (2012) this was exploited to show that one could potentially determine the neutrino mass hierarchy due to a different neutrino flavor mixing effect on the rise-time of the neutrino signal on earth, provided this signal could be robustly predicted by simulations. In this work, a set of our models with only the LS180 equation of state and no mixing length scheme was used. We find here that the $\bar{\nu}_e$ and ν_x signal during the first 100ms seems to be rather insensitive to these factors and would thus serve as such a generic template. (Of course, there are now numerous planned and ongoing experiments on earth that will most probably measure the neutrino mass hierarchy before a galactic supernova might occur).

As already stated in Serpico et al. (2012), a generic feature of all models is that the luminosities of the heavy-lepton neutrinos reach their maximum value faster than the anti-electron neutrinos, as the $\nu\nu$ or e^+e^- pair-production processes that could emit $\bar{\nu}_e$ are fermi-blocked due to the copious amounts of ν_e and electrons present during the first $\sim$ 10ms after core bounce. Only later when a sufficient amount of lepton number has been carried away and the temperature of the post-shock matter rises can these processes kick in, resulting in a delayed maximum. The maximal value is then higher than the maximum of the heavy lepton neutrinos, due their additional production by charged current reactions.

Neutrino energy hierarchy

It is known (Keil et al., 2003; Buras et al., 2006b; Marek and Janka, 2009; Marek et al., 2009) that the classical hierarchy of the mean neutrino energies, $\langle\varepsilon_{\nu_e}\rangle < \langle\varepsilon_{\bar{\nu}_e}\rangle < \langle\varepsilon_{\nu_x}\rangle$, can be inverted at late times to $\langle\varepsilon_{\nu_e}\rangle < \langle\varepsilon_{\nu_x}\rangle \lesssim \langle\varepsilon_{\bar{\nu}_e}\rangle$, in simulations with a sufficiently sophisticated set of neutrino opacities. The effect was attributed to the fact that the inclusion of neutrino-pair production and annihilation as well as neutrino nucleon (down-) scattering acts as filter for high energy heavy-lepton neutrinos (see also Raffelt, 2001), resulting in a reduction of their mean energy on their way out of the proto neutron star. Next to that, while the bulk of the heavy lepton neutrinos is coming from deeper inside the proton neutron star and mostly pass through the cooling layer without many interactions, anti-electron neutrinos due to their stronger coupling via the additional charged-current reaction channel are more abundantly produced there, which can overall result in an inversion of the classical ordering.

Our simulations also show this behaviour. In some extreme cases, we even find a doubly-inverted hierarchy with $\langle\varepsilon_{\nu_x}\rangle < \langle\varepsilon_{\nu_e}\rangle < \langle\varepsilon_{\bar{\nu}_e}\rangle$. This is a result of the long accretion phase simulated here, while the bulk of the heavy lepton neutrino flux is unaffected by the accretion layer, the electron flavor neutrinos are abundantly produced there. As the proto neutron star contracts the accreting matter falls deeper into its potential well and gets more compressed, thus hotter, which is visible in the increasing mean electron neutrino energies over time. While this might be unrealistic for exploding models, black-hole forming progenitors will show such a long accretion phase.

See Figure 3.10 for plots of the mean energies, luminosities, and profiles of the energy- and number-density of the neutrino flux and the mean energies of the neutrinos in comparison with the matter temperature, for one selected case (s15s7b2). We define the mean energy of the flux similar to Eq (3.4) as the ratio of neutrino energy flux H over neutrino number flux $\mathcal{H}$, again in terms of the neutrino intensity as

$$\langle\varepsilon\rangle_{\text{flux}} = \frac{H}{\mathcal{H}} = \frac{\int_0^\infty d\varepsilon \int_{-1}^{1} d\mu\, \mu\, \mathcal{I}(\varepsilon,\mu)}{\int_0^\infty d\varepsilon \int_{-1}^{1} d\mu\, \mu\, \varepsilon^{-1}\mathcal{I}(\varepsilon,\mu)}. \tag{3.10}$$

(By looking at this quantity instead of $\langle\varepsilon\rangle$, the purely geometrical influence of the spherical radiating surface is eliminated)

One can see that in a region from $\sim 20 - 30$km, the heavy lepton neutrino number flux saturates at comparatively low radii, while the energy carried by these neutrinos in total as well as their mean energy diminishes, as these neutrinos are down-scattered on nucleons and/or electrons on their way out of the proto neutron star. This is the region of the “filter-effect” described by Raffelt (2001). Compare also the very similar Figure 11 in that work, in which heavy lepton neutrino spectrum formation on hydrostatic backgrounds is analysed in great detail.

The electron flavor fluxes, on the other hand, saturate only much farther out and are still greatly enhanced where the heavy lepton flavor neutrinos are already

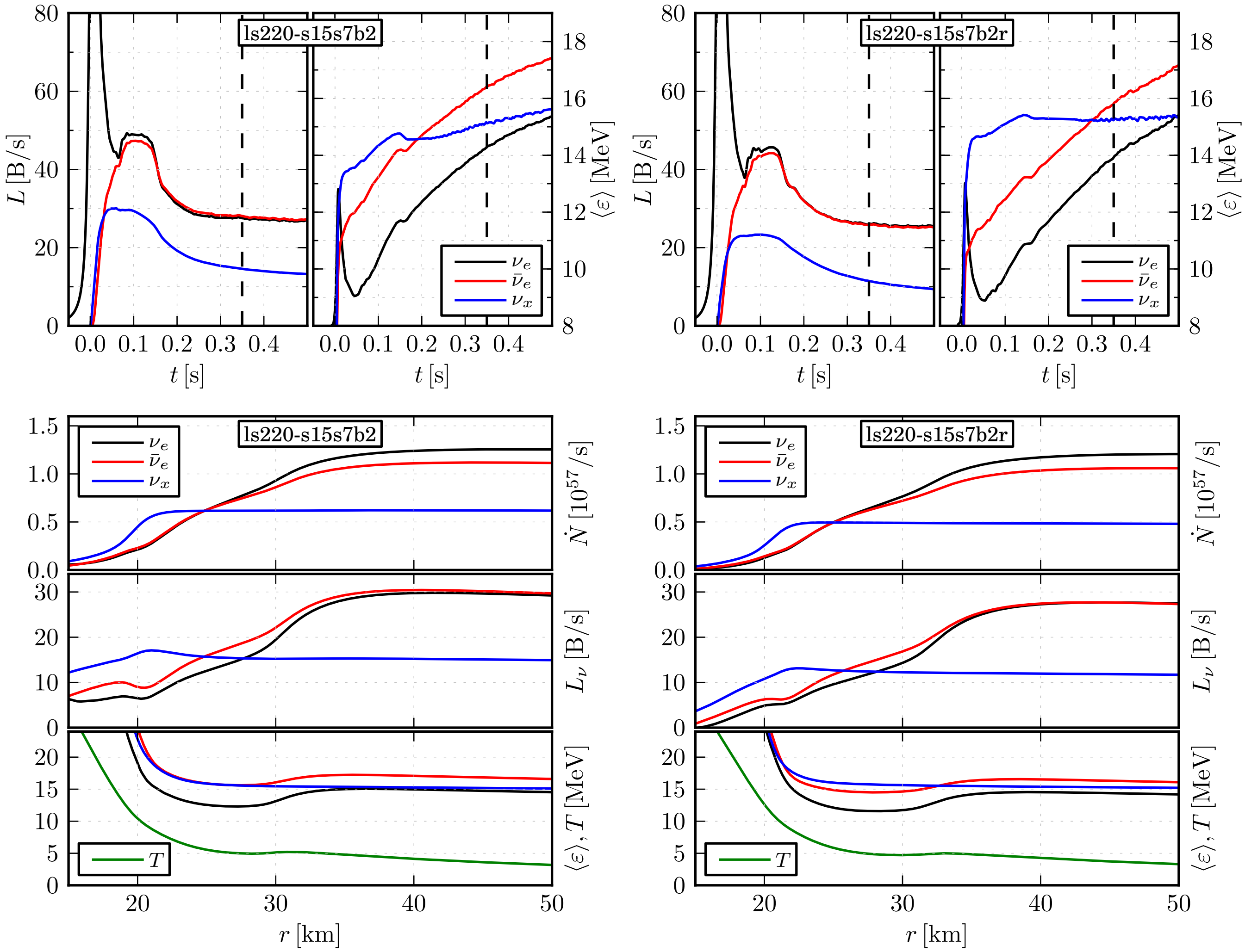

Figure 3.10: The upper panels show the luminosity and mean energies as a function of time, extracted at a radius of 500km. The lower panels show profiles of the neutrino flux number- and energy-density at the times indicated by the dashed lines in the upper panels, where the filter-effect on the heavy-lepton neutrinos and the thermal enhancement of the electron flavor neutrinos can be observed. Model ls220-s15s7b2 on the left panels is simulated with the full opacity set of Table 2.1, while model ls220-s15s7b2r on the right was done with the isoenergetic neutrino-nucleon scattering according to Bruenn (1985) and without $\nu\nu$ pair-processes. In both cases $\langle\varepsilon_{\nu_x}\rangle < \langle\varepsilon_{\bar{\nu}_e}\rangle$ is found at sufficiently late times.

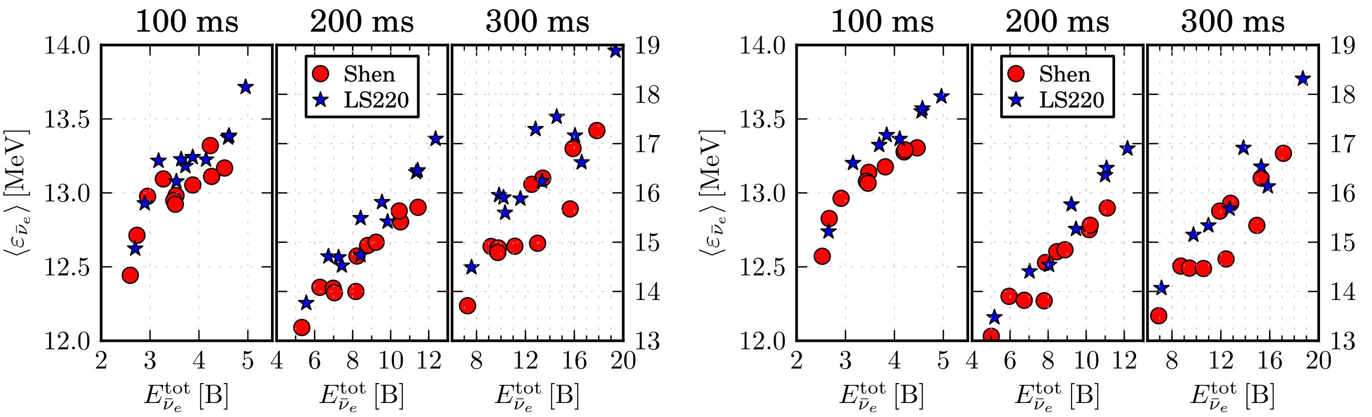

Figure 3.11: A plot analogous to Figure 8 of O'Connor and Ott (2013), showing the instantaneous mean anti-electron neutrino energy as a function of the cumulative emitted anti-electron neutrino energy so far for three different times. The left panel shows models without, the right panel models with the mixing length scheme active. Contrary to O'Connor and Ott (2013), no clear separation between the used EoS can be discerned.

decoupled from the medium, aided also by the temperature inversion typically found in the profiles. There, the hot compressed matter from the accretion flow provides an additional thermal source for electron flavor neutrinos and only there do the mean energies of the anti-electron neutrinos exceed those of the heavy lepton neutrinos again.

Both effects, the downscattering of the heavy lepton neutrinos and the thermal enhancement of the (anti) electron neutrinos, are relevant for the inversion of the mean energies.

In a similar study of the pre-explosion neutrino signal, O'Connor and Ott (2013), who take into account only isoenergetic scattering processes in their transport code, still get the classical hierarchy of $\langle \varepsilon_{\nu_e} \rangle < \langle \varepsilon_{\bar{\nu}_e} \rangle < \langle \varepsilon_{\nu_x} \rangle$. Also, they see a remarkably clear imprint of the high density EoS in the neutrino signal (presented in their Figure 8), when they look at the instantaneous mean anti-electron neutrino energy $\langle \varepsilon_{\bar{\nu}_e} \rangle$ as a function of the cumulative emitted energy by anti-electron neutrinos in total, defined as

$$E^{\mathrm{tot}}_{\bar{\nu}_e}(t) = \int_{-\infty}^{t} L_{\bar{\nu}_e}(t')\, dt'. \tag{3.11}$$

We looked into this as well, however, we are unable to confirm the clear separation they see. In Figure 3.11 the reader can look at these quantities using our model set. Next to that, oscillation effects would mix the spectrum of different flavors on their way to a detector on earth.

3.4.4 Comparison to a reduced set of opacities

As can be seen from Table 2.1, we include neutrino pair processes and nucleon opacities including correlation effects as well as the corresponding neutrino energy exchange by nucleon recoil according to the prescription of Burrows and Sawyer (1999) in our simulations (but see also Section 3.4.6 for remaining deficiencies in the nucleon opacities).

To emphasise the importance of these ingredients, we also ran a couple of simulations with a reduced set of opacities where we omitted these reactions, that is we did not include any neutrino pair processes and used the rates from Bruenn (1985) for isoenergetic neutrino nucleon scattering, results for s15s7b2 and LS220 as high density EoS can be found in the right panels of Figure 3.10

In these simulations, the mean energies of the electron and anti-electron neutrinos are lower than in the full simulations, whereas the heavy lepton neutrino mean energies are enhanced, and the differences are more pronounced in the early phases of the simulations. The luminosities of the heavy lepton neutrinos are inversely affected, the higher mean energies in the reduced simulations come with lower luminosities. This is consistent with previous results of Buras et al. (2006b). The lack of non-isoenergetic scattering processes on nucleons makes cooling of ν_x less efficient compared to the full simulations, and the high energy neutrinos then have a harder time diffusing out of the proto neutron star due to the increased reaction cross sections. Next to that, less heavy lepton neutrinos are produced in the first place due the omission of $\nu\nu$ pair processes (see also Keil et al., 2003). This is also visible in the very late phases, in the full simulations the heavy lepton neutrino mean energy continues to rise, as a portion of their flux is due to the pair production by hot electron flavor neutrinos. In the reduced case, the heavy lepton neutrinos are more strongly decoupled from the electron flavor and thereby the rising medium temperature in the accretion layer.

The electron and anti-electron neutrino luminosities are not compensated in this way, both the mean energies as well as the luminosities of both the electron type neutrino species are lower than seen in the full simulations.

Interestingly, even for this simpler set of neutrino opacities we still find the classical hierarchy of mean energies inverted, albeit at later times than in the simulations with the full opacity set. It is true that the “filter-effect” on the heavy-lepton neutrinos is much less visible in the reduced simulations, as the main energy exchange process via non–isoenergetic nucleon scattering is switched off (see Figure 3.10). However, over time the electron flavor neutrinos follow the temperature of the increasingly hotter accretion layer, while the heavy lepton neutrino mean energy ceases to rise, resulting still in an inversion at sufficiently late times.

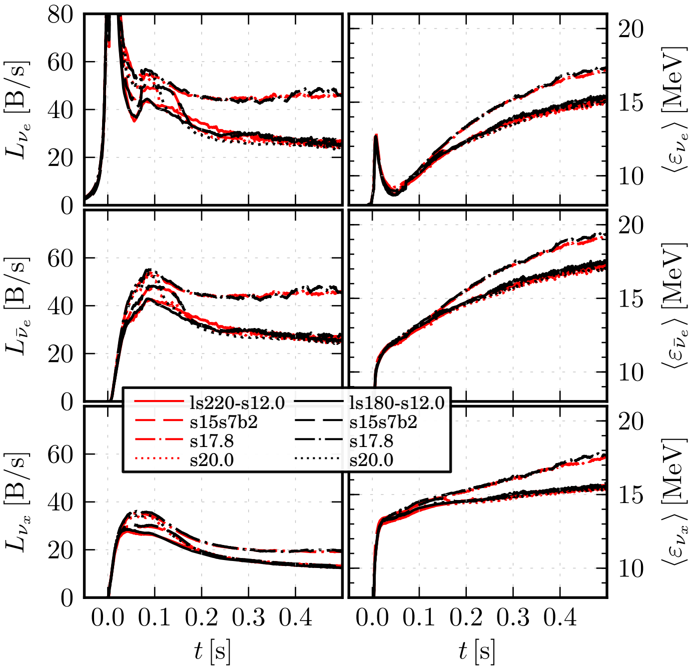

Figure 3.12: Neutrino quantities for models using LS180 (black) and LS220 (red). The different high density behaviour has only little impact on simulations with neutron stars that are far from the stability limit. Only extreme cases with more massive neutron stars are affected by the different high density descriptions.

3.4.5 Influence of Constraints on the Equation of State

The recent solid measurements of $\sim 2.0\,\mathrm{M}_\odot$ neutron stars by Demorest et al. (2010) and Antoniadis et al. (2013) lead to powerful constraints on the (cold) high-density equation of state, ruling out a number of models with low compressibility parameters such as the LS180, which was heavily used in previous work in the literature.

One should be cautious to draw too much conclusions for this as to the validity of equations of state for supernova simulations, since the compact remnant there is very different from a cold neutron star. While a particular equation of state might fail to reproduce the constraints of the cold configuration it could still be a good model for the temperatures involved in supernova simulations – especially for proto neutron stars that are far away from the maximum mass.

To illustrate this, we also simulated a number of models with moderate proto neutron star mass using the LS220 high density EoS also with the previously widely used LS180. As one can see in Figure 3.12, the differences for all models in the luminosities and mean energies are rather small, especially for models with lower neutron star masses.

3.4.6 Missing physics in neutrino opacities

It was noted by Martínez-Pinedo et al. (2012) and Roberts (2012); Roberts et al. (2012a)[1] that the formulation of the neutrino nucleon interaction according to Bruenn (1985) and Burrows and Sawyer (1999) was missing the effect of the nucleon background potential in the dense medium on the reaction kinematics, effectively changing the Q-value of any nucleonic beta reaction in an EoS–dependent way.

This is due to the fact that the energy-momentum equation for (nonrelativstic) nucleons is changed from the free relation in a vacuum,

$$E_i^{\text{free}}(p_i) = \frac{p_i^2}{2m_i} + m_i c^2, \quad i = n, p, \tag{3.12}$$

to the mean-field approximated relation at high densities,

$$E_i^{\text{mf}}(p_i) = \frac{p_i^2}{2m_i^*} + m_i c^2 + U_i, \quad i = n, p, \tag{3.13}$$

with m_i^* the effective nucleon masses and U_i the single-particle interaction potentials of either protons or neutrons, both dependent on the local thermodynamic state. It was precisely the terms U_n and U_p that were neglected in the method and our implementation of the nucleonic opacities according to Burrows and Sawyer (1999), even though their formalism explicitly claimed to include this effect.

All simulations discussed so far suffer from this defect, however, for four selected progenitors covering the range of our model set, s11.2, s25.0, s27.0, s40.0, and for both high density equations of state, we could run our simulations again with new neutrino rate prescriptions which do take these effects into account. As it turns out - at least during the accretion phase and for the two EoS that were employed in this study - an effect on the emitted neutrino signal in the unmixed simulations is present, but not overwhelmingly large, as was expected by Martínez-Pinedo et al. (2012). For the mixing-length simulations, the effect is minimal, the larger neutron stars there shift the neutrinospheres to lower densities and higher temperatures, where the corrections due to the nucleon potentials is comparably smaller.

See Figure 3.13 for mean energies and luminosities of models with and without the corrected opacities.

One has to expect from the results of Martínez-Pinedo et al. (2012) (and we actually confirm that in Section 5.4), that there will be a much larger correction also in our simulations of the post-explosion phase, where matter accretion largely ceases and the neutrino signal from deeper within the core starts to dominate. Also, multidimensional simulations, where accretion can happen in narrow downflows and some portion of the proto neutron star can be exposed even during the accretion phase, might also be at partially influenced by these corrections.

---

[1] Martínez-Pinedo et al. (2012) published their preprint earlier on the arXiv, while Roberts (2012) submitted earlier to the journal.

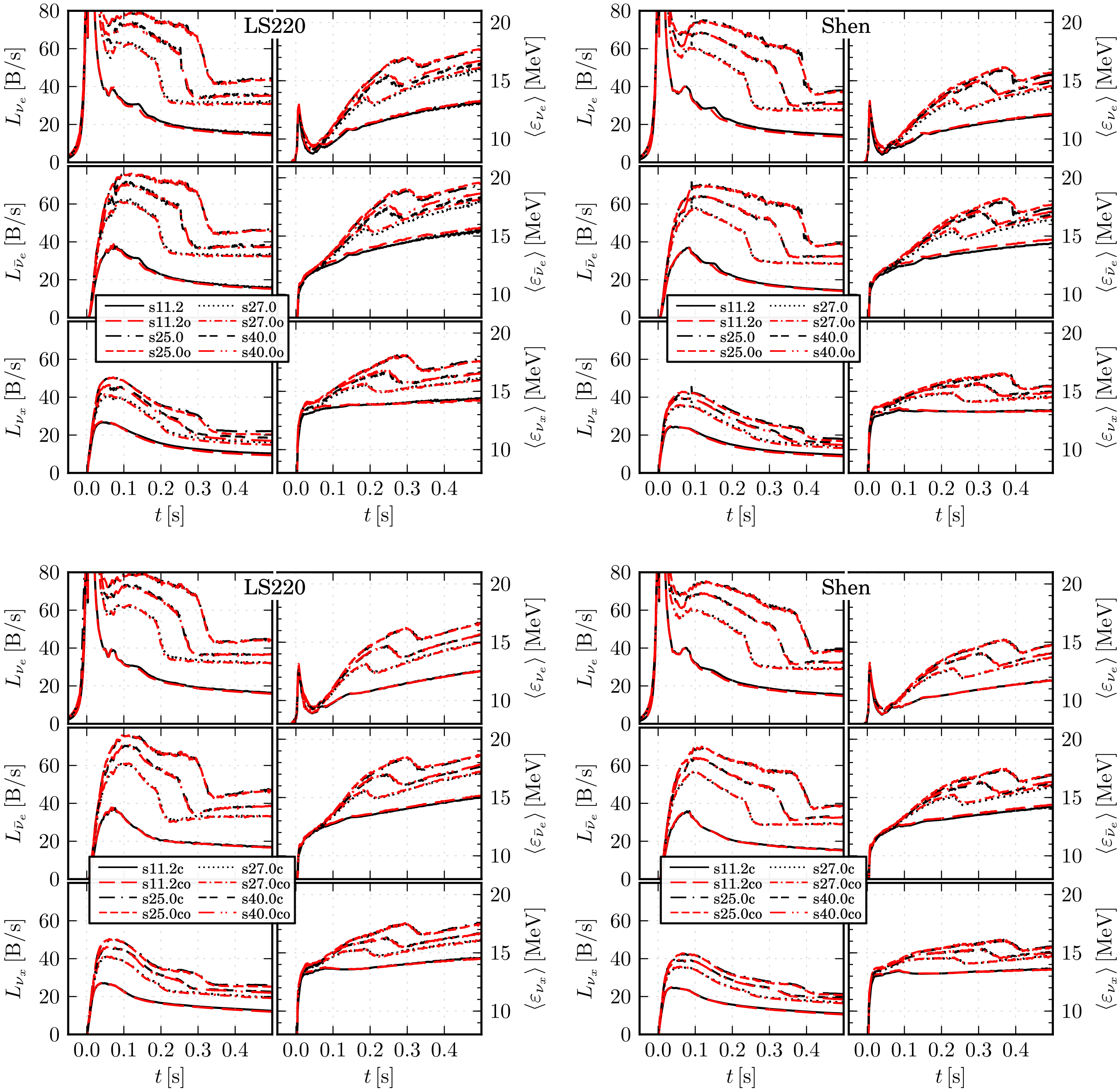

Figure 3.13: Comparison of the neutrino signal of the s11.2 and s40.0 models with ("o", and if additionally also with convection as "co") and without the correction due to the neglected nucleon potential effects.

3.5 Neutrino Spectra

With Eq. (3.4) in mind, we define the normalized neutrino energy spectrum as

$$f(\varepsilon) = \frac{\int_{-1}^{1} d\mu\, \mathcal{I}(\varepsilon, \mu)}{\int_0^\infty d\varepsilon \int_{-1}^{1} d\mu\, \mathcal{I}(\varepsilon, \mu)}, \tag{3.14}$$

such that the mean energy is recovered as

$$\langle \varepsilon \rangle = \int_0^\infty d\varepsilon\, \varepsilon f(\varepsilon). \tag{3.15}$$

A purely thermal, black-body spectrum is with this definition given by

$$f_T(\varepsilon) = \frac{2}{3\zeta_3 T^3} \cdot \frac{\varepsilon^2}{1 + \exp(\varepsilon/T)}, \tag{3.16}$$

where here and in the following ζ_n are values of the Riemann-Zeta function. Following Keil et al. (2003), we characterize the spectra by energy moments, compatible to their definition and calculated in analogy to Eq. (3.15) as

$$\langle \varepsilon^n \rangle = \int_0^\infty d\varepsilon\, \varepsilon^n f(\varepsilon). \tag{3.17}$$

In the literature one often encounters "rms"-mean energies, unfortunately with conflicting definitions, Liebendörfer et al. (2005) for example define it (in our notation) as

$$\langle \varepsilon \rangle_{\mathrm{rms}} = \sqrt{\langle \varepsilon^2 \rangle}, \tag{3.18}$$

while Keil et al. (2003) use

$$\langle \varepsilon \rangle_{\mathrm{rms,Keil}} = \sqrt{\frac{\langle \varepsilon^3 \rangle}{\langle \varepsilon \rangle}}. \tag{3.19}$$

It has become common to look at the first two moments to characterize the spectrum, or to derive parameters of model spectra in such a way as to reproduce the first two moments of the simulated spectra. Commonly used models are degenerate Fermi-Dirac spectra, with the two parameters η, T as

$$f_{\eta,T}(\varepsilon) = \frac{1}{-2\mathrm{Li}_3(-e^\eta) T^3} \cdot \frac{\varepsilon^2}{1 + \exp\left(\varepsilon/T - \eta\right)}, \tag{3.20}$$

where the function $\mathrm{Li}_n(z)$ in the normalization factor is the polylogarithm, or general Fermi-Integral, cf. Abramowitz and Stegun, 1970, p. 1005. (Note that the parameter η of the emanating spectrum should not be directly identified with any physical degeneracy of the neutrinos at their "source", as the resulting spectra are shaped by processes out of thermal equilibrium)

By integration of Eq (3.20), one finds for the energy moments

$$\langle\varepsilon\rangle_{\eta,T} = 3\frac{\mathrm{Li}_4(-e^\eta)}{\mathrm{Li}_3(-e^\eta)}T, \tag{3.21}$$

$$\left\langle\varepsilon^2\right\rangle_{\eta,T} = 12\frac{\mathrm{Li}_5(-e^\eta)}{\mathrm{Li}_3(-e^\eta)}T^2, \tag{3.22}$$

$$\langle\varepsilon^n\rangle_{\eta,T} = \frac{(n+2)!}{2}\frac{\mathrm{Li}_{n+3}(-e^\eta)}{\mathrm{Li}_3(-e^\eta)}T^n. \tag{3.23}$$

Note that for $\eta \to 0$ the polylogarithm is given in terms of Dirichlet η-function or Riemann ζ-function values by

$$\mathrm{Li}_s(-1) = -\eta(s) = \left(2^{1-s} - 1\right)\zeta(s). \tag{3.24}$$

Unfortunately, as already noted by Raffelt (2001), equations (3.21) and (3.22) cannot be solved for all possible pairs of energy moments $\langle\varepsilon\rangle, \left\langle\varepsilon^2\right\rangle$, but only when

$$\frac{16}{15} < \frac{\left\langle\varepsilon^2\right\rangle}{\langle\varepsilon\rangle^2} < \frac{4}{3} \tag{3.25}$$

holds. Another model spectrum was suggested by Keil et al. (2003), normalized it is

$$f_{\alpha,\bar\varepsilon}(\varepsilon) = \frac{(1+\alpha)^{1+\alpha}}{\bar\varepsilon\Gamma(1+\alpha)}\cdot\left(\frac{\varepsilon}{\bar\varepsilon}\right)^\alpha \exp(-(\alpha+1)\,\varepsilon/\bar\varepsilon), \tag{3.26}$$

with the two parameters α, $\bar\varepsilon$. The energy moments of that spectrum are

$$\langle\varepsilon\rangle_{\alpha,\bar\varepsilon} = \bar\varepsilon \tag{3.27}$$

$$\langle\varepsilon^n\rangle_{\alpha,\bar\varepsilon} = \bar\varepsilon^n \cdot \frac{\Gamma(1+\alpha+n)}{\Gamma(1+\alpha)(1+\alpha)^n}. \tag{3.28}$$

It has the advantage that it is analytically simple and can represent arbitrary ratios of the first two energy moments.

A more direct quantity derived explicitly from the energy moments was introduced by Raffelt (2001), the “pinching-parameter” p. It is defined as

$$\begin{aligned} p = \left(\frac{\left\langle\varepsilon^2\right\rangle_T}{\langle\varepsilon\rangle_T^2}\right)^{-1}\cdot\frac{\left\langle\varepsilon^2\right\rangle}{\langle\varepsilon\rangle^2} = \frac{49\pi^8}{486,000\,\zeta_3\zeta_5}\cdot\frac{\left\langle\varepsilon^2\right\rangle}{\langle\varepsilon\rangle^2} \\ =: \frac{1}{a}\cdot\frac{\left\langle\varepsilon^2\right\rangle}{\langle\varepsilon\rangle^2} \simeq \frac{1}{1.30291}\cdot\frac{\left\langle\varepsilon^2\right\rangle}{\langle\varepsilon\rangle^2}, \end{aligned} \tag{3.29}$$

where $p = 1$ is obtained when the first two energy moments are thermal, $p < 1$ denotes a “pinched” spectrum – meaning it has a suppressed high energy tail compared to a thermal spectrum, and vice versa for $p > 1$.

The shape determining parameters η and α can directly be expressed only as a function of p, by

$$p(\eta) = \frac{4}{3a}\frac{\mathrm{Li}_3(-\mu)\mathrm{Li}_5(-\mu)}{\mathrm{Li}_4(-\mu)^2} \text{ and } \frac{3}{4}a < p < \frac{15}{16}a, \tag{3.30}$$

$$p(\alpha) = \frac{1}{a}\frac{2+\alpha}{1+\alpha}. \tag{3.31}$$

We will thus always only provide p, the reader interested in either η or α can invert these equations, trivially so for Eq. (3.31) and for Eq. (3.30) either numerically or for values near $p = 1$ via expansions, e.g. given in Keil et al. (2003).

Numerical problems with the propagation of the neutrino energy distribution along the radial grid result in some diffusive losses of the energy peak to neighbouring energy bins, therefore a naive evaluation of the pinching parameter or the rms mean energy at a fixed radius of, say, 500km as it is usually done comes up with an anti-pinched, unphysical spectrum. (Note that this is not a problem connected to the frame transformations needed to get the values for an observer frame at rest, as the pinching parameter is an invariant Lorentz scalar that can safely be evaluated in the comoving quantities directly provided in our simulation data) A visualization of this artificial spectral distortion can be found in Figure 3.14.

The numerical diffusivity seems mostly to be dependent on the velocity gradient at the shock front, where the doppler terms result in a strong redistribution along the (fixed) energy grid, as the neutrinos coming out of the interior appear strongly blue-shifted in the frame of the infalling matter and are thus distributed into higher energy bins, then redistributed as the in-fall velocities decrease with increasing radius.

Still, all equations are formulated in an energy and particle number conservative way and thus while the shape of the spectrum might get somewhat distorted as the radiation field is propagated along the grid, its mean and total energy is not affected by this phenomenon.

We therefore evaluated the pinching parameter at a radius just below the shock front, and recovered the true $\langle\varepsilon\rangle^{\mathrm{rms}}$ via Eq. (3.29) from that p and the mean energy at 500km[2].

In Figure 3.15 we present the resulting $\langle\varepsilon\rangle^{\mathrm{rms}}$ and p for all convective models, and for s11.2 and s40.0 in comparison with both a convective run and a simulation with the opacity corrections as described in Section 3.4.6.

As expected, all neutrino species start with a strongly pinched spectrum, that is with a suppressed high energy tail compared to a corresponding thermal spectrum, due to the energy dependence of the neutrino cross sections: high energy neutrinos are more likely to be absorbed, or will loose some of their energy in proportionally more scattering reactions on nucleons in the atmosphere above the proto neutron star.

---

[2] In principle, this is slightly inconsistent as there is a delay time of $\mathcal{O}$(ms), which is however much smaller than the timescale for changes in the spectrum or the mean energies

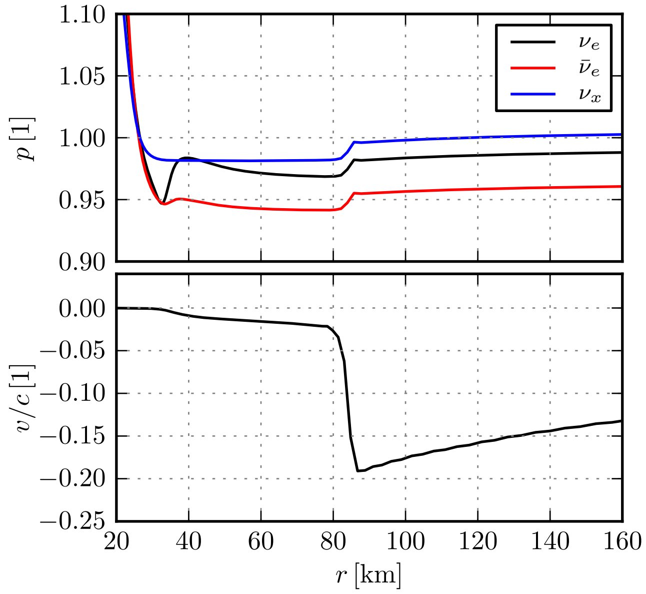

Figure 3.14: Profiles of the pinching parameters (*upper panel*) and the matter velocity (*lower panel*) 0.3 seconds after core bounce for model ls220-s11.2. Physically, a drastic change in the shape of the spectrum is not expected or realistic for the dilute ($\sim 10^8\,\mathrm{g/cm^3}$) matter around the shock front at $\sim 80\,\mathrm{km}$, the jump in the pinching parameters for all neutrino flavors is a numerical artefact.

Finally, we present the time-averaged neutrino parameters of all models in Tables 3.4 and 3.5, where the different quantities Q were weighted by the number of emitted neutrinos as

$$\langle Q \rangle_t = \frac{\int_t \mathrm{d}t \dot{N}_\nu Q(t)}{\int_t \mathrm{d}t \dot{N}_\nu}, \tag{3.32}$$

which might be of interest for judging the total amount and characteristics of the neutrino output of accretion dominated core-collapse events into the diffuse supernova neutrino background.

Typically, half a second of accretion emits $\sim 1.0 - 1.5 \cdot 10^{57}$ electron neutrinos, $\sim 0.5 - 1.0 \cdot 10^{57}$ anti-electron neutrinos, and $\sim 1.5 - 2.5 \cdot 10^{57}$ heavy lepton (anti-) neutrinos.

Electron neutrinos have lowest mean energies of $\sim 10 - 12\,\mathrm{MeV}$, while both anti-electron and heavy-lepton neutrinos present with very similar mean energies of $\sim 13 - 16\,\mathrm{MeV}$.

Note that the heavy-lepton neutrinos have a harder spectrum with $p > 1$ when using the reduced opacity set, due the aforementioned lack of energy-exchange reactions that could bring the high energy tail down.

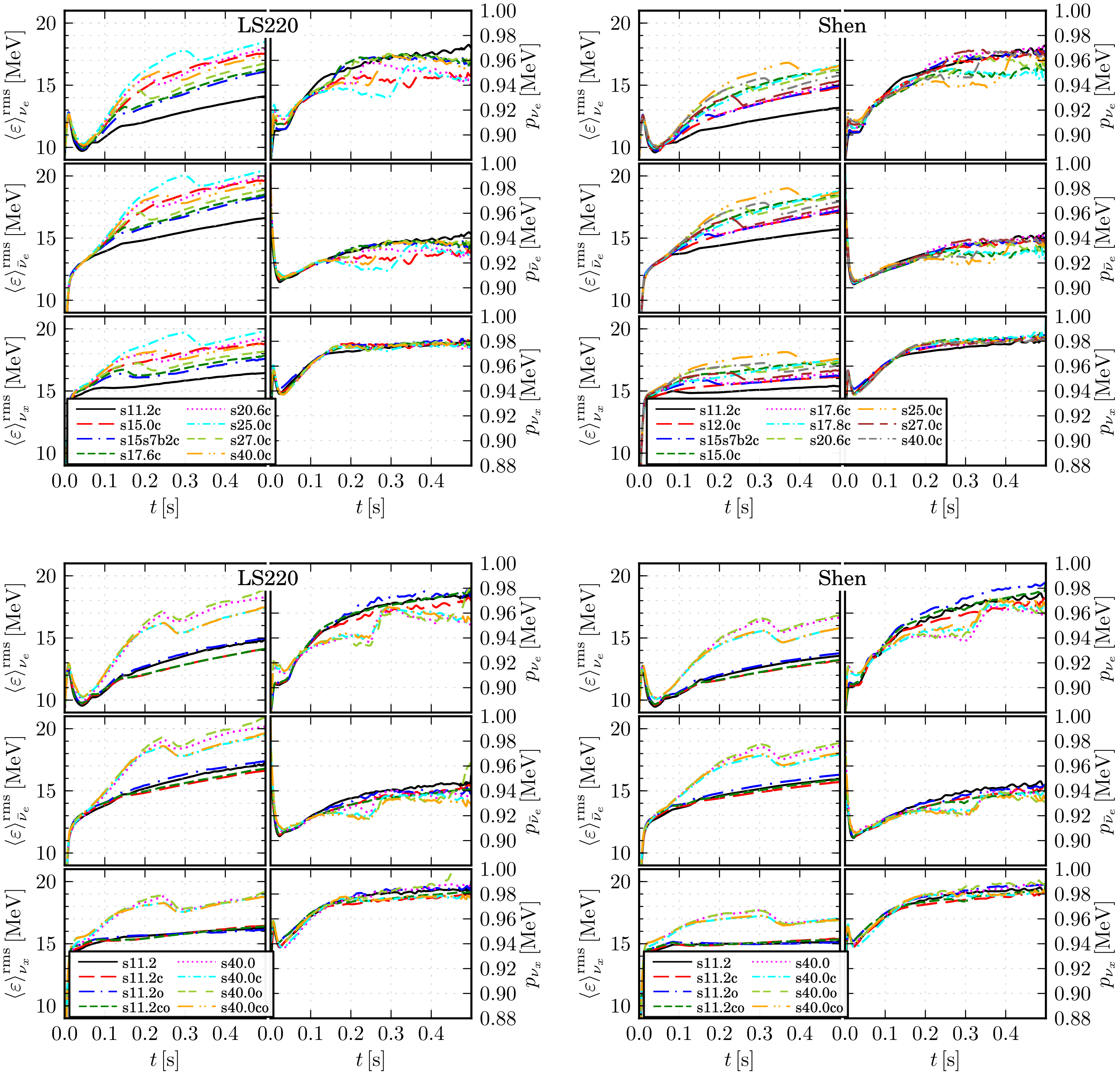

Figure 3.15: The rms-mean energies defined by Eq. (3.18) and the pinching parameter for all convective models (upper panels) and for selected models in comparison to models without the convection scheme, using either standard or corrected opacities.

Table 3.4: Time averaged mean neutrino energies and total number of emitted neutrinos from before collapse up to the simulated 0.5s after bounce, for the LS220 models. Note that N_{ν_x} and E_{ν_x} are for only one of the four heavy lepton neutrino kinds, i.e. the total emitted energy is $E_{\nu_e} + E_{\bar{\nu}_e} + 4E_{\nu_x}$.

Model	$\langle\varepsilon\rangle_{\nu_e}$	$\langle\varepsilon\rangle_{\bar{\nu}_e}$	$\langle\varepsilon\rangle_{\nu_x}$	p_{ν_e}	$p_{\bar{\nu}_e}$	p_{ν_x}	N_{ν_e}	$N_{\bar{\nu}_e}$	N_{ν_x}	E_{ν_e}	$E_{\bar{\nu}_e}$	E_{ν_x}
	[MeV]			[1]			[10^{57}]			[B]		
s11.2r	10.6	13.1	14.6	0.93	0.92	1.02	0.89	0.47	0.28	15.1	9.8	6.4
s11.2	10.6	13.6	13.7	0.93	0.93	0.97	0.93	0.51	0.35	15.7	11.0	7.8
s11.2c	10.5	13.4	13.8	0.93	0.93	0.97	0.96	0.50	0.38	16.2	10.7	8.4
s11.2o	10.8	13.8	13.8	0.93	0.93	0.97	0.89	0.48	0.34	15.4	10.7	7.5
s11.2co	10.6	13.5	13.8	0.93	0.93	0.97	0.95	0.49	0.37	16.0	10.6	8.3
s12.0	11.5	14.6	14.3	0.93	0.93	0.97	1.12	0.65	0.39	20.6	15.3	9.0
s15.0	12.4	15.7	15.3	0.93	0.93	0.97	1.49	0.92	0.51	29.5	23.1	12.6
s15.0c	12.2	15.4	15.3	0.93	0.92	0.97	1.51	0.90	0.53	29.6	22.2	13.1
s15s7b2r	11.3	14.0	15.1	0.93	0.92	1.02	1.13	0.66	0.32	20.5	14.7	7.7
s15s7b2	11.6	14.7	14.5	0.93	0.93	0.97	1.14	0.67	0.41	21.1	15.7	9.5
s15s7b2c	11.3	14.3	14.5	0.93	0.93	0.97	1.18	0.66	0.44	21.4	15.3	10.2
s17.6	11.5	14.6	14.6	0.93	0.93	0.97	1.26	0.75	0.46	23.2	17.5	10.8
s17.6c	11.3	14.4	14.6	0.93	0.93	0.97	1.30	0.73	0.49	23.6	16.9	11.6
s17.8	12.4	15.7	15.3	0.93	0.93	0.98	1.41	0.86	0.48	28.1	21.8	11.7
s20.0	11.3	14.4	14.4	0.93	0.93	0.97	1.17	0.68	0.43	21.1	15.7	9.9
s20.6	12.3	15.6	15.4	0.93	0.93	0.97	1.60	0.99	0.58	31.5	24.7	14.2
s20.6c	12.2	15.4	15.4	0.93	0.92	0.97	1.63	0.97	0.61	31.8	23.9	15.0
s25.0r	12.6	15.4	16.4	0.93	0.92	1.01	1.79	1.13	0.48	36.1	27.8	12.5
s25.0	13.0	16.3	16.2	0.93	0.93	0.97	1.74	1.10	0.63	36.3	28.8	16.2
s25.0c	12.7	16.0	16.0	0.93	0.92	0.97	1.80	1.10	0.66	36.7	28.0	16.9
s25.0o	13.0	16.4	16.1	0.93	0.93	0.98	1.73	1.10	0.61	36.1	28.8	15.8
s25.0co	12.8	16.1	16.0	0.93	0.92	0.97	1.78	1.08	0.65	36.4	27.9	16.7
s27.0	11.7	14.9	14.8	0.93	0.93	0.97	1.39	0.84	0.51	26.1	20.0	12.1
s27.0c	11.6	14.7	14.9	0.93	0.93	0.97	1.43	0.82	0.54	26.5	19.4	13.0
s27.0o	11.9	15.1	14.9	0.93	0.93	0.97	1.35	0.81	0.49	25.8	19.7	11.7
s27.0co	11.6	14.8	14.9	0.93	0.92	0.97	1.41	0.81	0.54	26.4	19.2	12.8
s40.0r	12.0	14.8	15.9	0.93	0.92	1.01	1.58	0.96	0.44	30.3	22.7	11.1
s40.0	12.2	15.4	15.3	0.93	0.93	0.97	1.58	0.98	0.57	30.9	24.1	14.1
s40.0c	12.1	15.3	15.4	0.93	0.92	0.97	1.61	0.96	0.61	31.3	23.4	15.0
s40.0o	12.4	15.7	15.5	0.93	0.92	0.97	1.54	0.95	0.55	30.7	24.0	13.7
s40.0co	12.2	15.4	15.4	0.93	0.92	0.97	1.60	0.95	0.60	31.2	23.3	14.8

Table 3.5: Same as Table 3.4 for the Shen EoS.

Model	$\langle\varepsilon\rangle_{\nu_e}$	$\langle\varepsilon\rangle_{\bar\nu_e}$	$\langle\varepsilon\rangle_{\nu_x}$	p_{ν_e}	$p_{\bar\nu_e}$	p_{ν_x}	N_{ν_e}	$N_{\bar\nu_e}$	N_{ν_x}	E_{ν_e}	$E_{\bar\nu_e}$	E_{ν_x}
	[MeV]			[1]			$[10^{57}]$			[B]		
s11.2	10.3	13.1	13.2	0.93	0.93	0.97	0.93	0.50	0.35	15.3	10.4	7.3
s11.2c	10.3	13.0	13.3	0.93	0.93	0.97	0.96	0.49	0.37	15.7	10.2	7.8
s11.2o	10.5	13.3	13.3	0.93	0.93	0.97	0.89	0.48	0.33	14.9	10.1	7.0
s11.2co	10.3	13.2	13.3	0.93	0.92	0.97	0.93	0.48	0.36	15.4	10.1	7.7
s12.0	11.0	14.0	13.7	0.93	0.93	0.97	1.11	0.63	0.38	19.6	14.2	8.3
s12.0c	10.9	13.8	13.7	0.93	0.92	0.97	1.13	0.62	0.40	19.8	13.7	8.8
s15.0	11.8	14.9	14.5	0.93	0.92	0.97	1.47	0.90	0.48	27.9	21.5	11.2
s15.0c	11.7	14.7	14.5	0.93	0.92	0.97	1.49	0.88	0.50	28.0	20.7	11.6
s15s7b2	11.2	14.1	13.9	0.93	0.93	0.97	1.13	0.66	0.39	20.3	14.8	8.8
s15s7b2c	11.0	13.9	13.8	0.93	0.92	0.97	1.17	0.65	0.42	20.6	14.4	9.3
s17.6	11.1	14.0	13.9	0.93	0.93	0.97	1.26	0.73	0.45	22.4	16.5	9.9
s17.6c	11.0	13.9	14.0	0.93	0.93	0.97	1.29	0.72	0.47	22.7	15.9	10.5
s17.8	11.8	14.9	14.4	0.93	0.92	0.97	1.44	0.87	0.47	27.2	20.8	10.9
s17.8c	11.7	14.7	14.3	0.93	0.92	0.97	1.46	0.85	0.49	27.2	19.9	11.3
s20.0	11.0	13.9	13.9	0.93	0.93	0.97	1.15	0.65	0.41	20.3	14.6	9.1
s20.6	11.8	14.8	14.6	0.93	0.92	0.97	1.59	0.98	0.55	30.0	23.2	12.8
s20.6c	11.7	14.7	14.6	0.93	0.92	0.97	1.62	0.95	0.57	30.3	22.3	13.4
s25.0	12.3	15.4	15.1	0.93	0.92	0.97	1.77	1.11	0.60	34.9	27.5	14.5
s25.0c	12.2	15.2	15.0	0.93	0.92	0.97	1.80	1.08	0.62	35.1	26.4	15.0
s25.0o	12.5	15.6	15.2	0.93	0.92	0.97	1.74	1.10	0.58	34.8	27.5	14.2
s25.0co	12.2	15.3	15.1	0.93	0.92	0.97	1.78	1.08	0.61	34.9	26.4	14.8
s27.0	11.3	14.3	14.2	0.93	0.93	0.97	1.38	0.82	0.49	25.0	18.8	11.1
s27.0c	11.2	14.1	14.2	0.93	0.93	0.97	1.42	0.81	0.52	25.4	18.2	11.7
s27.0o	11.5	14.5	14.3	0.93	0.93	0.97	1.35	0.80	0.47	24.8	18.7	10.8
s27.0co	11.3	14.3	14.2	0.94	0.92	0.97	1.40	0.80	0.51	25.3	18.2	11.6
s40.0	11.9	15.0	14.8	0.93	0.92	0.97	1.57	0.96	0.54	30.0	23.0	12.8
s40.0c	11.7	14.7	14.6	0.93	0.92	0.97	1.61	0.95	0.57	30.2	22.3	13.4
s40.0o	12.0	15.1	14.8	0.93	0.92	0.97	1.55	0.95	0.53	29.8	23.0	12.5
s40.0co	11.7	14.8	14.7	0.93	0.92	0.97	1.60	0.94	0.57	30.1	22.2	13.3

3.6 Summary

We simulated the gravitational collapse, neutron star formation and subsequent accretion phase for a large number of progenitors and three different high density equations of state with a detailed neutrino transport and hydrodynamics code in spherical symmetry.

For the first time, this was augmented also with a mixing-length prescription applied within the proto neutron star in order to mimic the genuinely multidimensional effect of convection. We found that the resulting neutrino signal with this scheme active was in much better agreement to true, computationally much more costly multidimensional simulations.

The most important consequence of the convection is a somewhat enlarged proto neutron star, which to zeroth order is reflected in larger neutrino luminosities and lower mean energies.

We could confirm a rather generic neutrino signal of the first 100ms of the accretion phase – for which the assumption of spherical symmetry is not bad – over the progenitors and equation of state models used. This was a requirement for the work of Serpico et al. (2012) which concerns itself with the possibility of detecting the neutrino mass hierarchy and in which also some of the models with the LS180 equation of state also presented in this chapter were used.

All models where simulated for 500ms of accretion. However, during this time the accretion layer will become unstable to nonspherical perturbations, and we know from true multidimensional models that this can result in quite large, global modes of non-radial motion. Next to that, if the conditions are right, these could help to develop an explosion, which is never found in spherically symmetric simulations (except for the very lowest mass progenitors).

However, we could still make good use the model set simulated. For one, to judge again the influence of certain opacity improvements implemented in our code, e.g. the inclusion of nucleon-recoil and nucleon correlations at high densities. Without these, a similar study of the pre-explosion accretion signal by O'Connor and Ott (2013) could infer a very clear imprint of the high-density equation of state from their simulated neutrino signal. With our comparatively more advanced neutrino opacities this clear signal, sadly, disappears.

Next to that, we could test the impact of the recently discovered (Roberts, 2012; Martínez-Pinedo et al., 2012) omission of the nucleon-interaction potentials in the nucleon opacities of Burrows and Sawyer (1999). We could reassure with our own code what was already claimed, that these effects are not important during the early, hot phase of accretion (and thus possibly also not for explosion scenarios).

Finally, the models produced here will serve as the starting point for the artificially exploded model set used in Chapter 5.

4 Black hole formation

A massive star has to die - one way or another - when the electron degeneracy pressure in its iron core is no longer able to withstand gravity. Its core then collapses under its own weight, and forms a proto neutron star.

One way to die for the star is then to explode in a spectacular supernova. For this, the intense neutrino irradiation from core and accretion must be able to heat up the matter above strongly enough to expel it. Then, the continuing infall of matter is stopped, its remaining hull is ejected and what is left behind is a neutron star.

However, it has become clear that this process is by no means overly robust: spherically symmetric simulations consistently fail to explode, except for the very low mass end of progenitors. It is thought that multi-dimensional effects that enhance this neutrino mechanism are a crucial ingredient to the explosion of the majority of massive progenitors, but for a certain fraction with unfavourable conditions – whatever they might be – this mechanism will simply fail and will not produce an explosion.

In such a case, stellar matter will continue to stream onto the proto neutron star. Its mass will continue to grow accordingly until a second threshold of instability is crossed, when it reaches the Tolmann-Oppenheimer-Volkoff-Mass, where thermal and neutron-degeneracy pressure give way to gravity. In such cases, the star will die by becoming a black hole. As the equation of state of neutron star matter is only poorly known, so is the precise value of this threshold mass. A lower bound could be established by the observation of stable $2\mathrm{M}_\odot$ neutron stars by Demorest et al. (2010) and Antoniadis et al. (2013).

Recent estimates for core collapse that result in a direct black hole formation range from $10-23\%$ (Woosley et al., 2002; Ugliano et al., 2012). Optically, such an event might not be visible at all other than by the fact that the light of a single star suddenly disappeared (unless rotation and/or strong magnetic fields are present to create an accretion disc around the black hole).

The neutrinos in these cases could then be the only signature of such an event. With no explosion, accretion will continue for a long time and thereby heat the proto neutron star to very high temperatures. This will result in neutrinos with particularly high energies. Not only is this favourable for a direct terrestrial detection of individual events due the increased interaction cross-sections ($\propto \epsilon^2$), but these neutrinos might also be the main source (of energy) for the diffuse supernova neutrino background (Beacom, 2010; Nakazato et al., 2008).

In the literature, first studies involving the black hole collapse of a neutron star were already done in early works of Wilson (1971), and occurred almost regularly for the soft high density equations of state used then.

Later, Baumgarte et al. (1996a,b) looked at the delayed collapse of a neutron star that was formed above the threshold mass but was initially stabilized by thermal pressure support. Due to neutrino emission, this object subsequently becomes unstable and collapses, ending the neutrino emission abruptly. In full GR, they used artificially reduced neutrino opacities (Baumgarte et al., 1996b) in order to trigger the collapse already 20ms post-bounce and then scaled the resulting neutrino emission accordingly, or used a rather coarse numerical grid (Baumgarte et al., 1996a), in order to save computer time. They used a high density equation of state that forms a Kaon condensate at high densities, resulting in a maximum neutron star mass of about $1.5\mathrm{M}_\odot$, which is not compatible with experimental and astrophysical constraints anymore. With their singularity avoiding formulation they were able to follow the neutrino signal even after the formation of an event horizon and could observe the very rapid, $\mathcal{O}(\mathrm{ms})$, decay of the neutrino emission. In a way the study in this chapter is complementary to their approach: where they used a very detailed and accurate description of GR and only a very simplistic model for the effects of neutrinos, we focus more on a detailed prescription of neutrino transport and only model GR in very phenomenological way.

Beacom et al. (2001) used these fast cutoff time scales to infer constraints on the absolute neutrino masses from future observations of such a delayed collapse event. The idea there is that the very rapid decay of the luminosities of all neutrino flavors at the same time over this short timescale allows a direct measurement of the relative propagation time delay due to the nonzero neutrino masses. For this to work, accurate prediction on the neutrino luminosities and mean energies at the time of collapse are necessary.

Liebendörfer et al. (2004), and more recently, Fischer et al. (2007, 2009) looked at the neutrino signal of black-hole formation for a number of 40 and 50 solar mass progenitors with a detailed three-flavor Boltzmann neutrino transport treatment and in full GR.

Sumiyoshi et al. (2007, 2008) simulated the black hole collapse of a 40 solar mass progenitor, also using a Boltzmann neutrino transport. All these studies use the nucleon opacities according to the isoenergetic formalism of Bruenn (1985), that is ignoring recoil, weak-magnetism, and nucleon correlation effects at high densities. They agree in that they find increasingly hard spectra towards the moment of black hole collapse, especially for the heavy lepton flavor neutrinos. Due to their lower coupling to electron-generation matter, they are emitted from higher densities and thus reflect the growing temperature from the more and more compressed core.

One motivation for this study was to check whether these very hard spectra are still found when the effect of neutrino energy changing nucleon-recoil is taken into account. While it is true that the “neutrinospheres” of the heavy lepton flavors are indeed much farther inside the proto neutron star, they still can scatter on their way out through the more dilute matter. Neglecting nucleon recoil will thus overestimate the high energy tail of the resulting spectra, especially considering that the more energetic neutrinos are also more likely to undergo an interaction with the medium of the proto neutron star's accretion atmosphere. Keil et al. (2003) have found in very detailed Monte-Carlo simulations, in which they could selectively switch off different neutrino interaction processes and assumptions, that nucleon recoil is the most important process in the scattering atmosphere for the heavy lepton neutrinos.

Yang and Lunardini (2011) emphasize, that megaton detectors could potentially detect black hole forming neutron star collapses out to distances as far as 2-3 megaparsec, a distance that contains enough galaxies for a detection rate of up to one event per decade, depending on the precise values for the expected neutrino signal.

Most recently, O'Connor and Ott (2011) simulated a large number of progenitors, however, with a focus more on determining the fraction and progenitor dependence of black-hole formation cases in the different sets of progenitors, than on a detailed neutrino signal. They also used full GR simulations, but only a comparably simple treatment of neutrinos, via a parametrized deleptonization during collapse and a leakage scheme with heating-terms for the neutrino back-reaction on the medium post bounce. They introduced the now widely used ζ-parameter as a measure for compactness and suggested threshold values to determine which progenitor is more likely to form a black hole. With a calibrated, parametrized neutrino transport, Ugliano et al. (2012) also studied the progenitor-remnant connection and found that it is difficult to predict with a single parameter whether a given progenitor will form a black hole or a successful explosion with a neutron star.

Compared to Fischer et al. (2009) (and their previous publications, Liebendörfer et al., 2004; Fischer et al., 2007) and Sumiyoshi et al. (2007, 2008), the only of the mentioned works with a similarly accurate neutrino transport, our code models GR only approximately, but has more realistic neutrino opacities implemented. At first glance, accurate GR treatment should be the prime necessity for anything involving black-holes. In our setup, we model the effect of GR with a post-newtonian, TOV-like potential (Marek et al., 2006) in an otherwise classical hydrodynamical simulation. However, we argue that for the scenario in question this is not a bad approximation: as the accretion on the proto neutron star is up until its very last few milliseconds a comparatively slow, quasi-hydrostatic process, the dynamics are not greatly affected by the approximation of using Newtonian mechanics, while the black-hole singularity is also present in our TOV-like potential.

To assure this, we perform an explicit comparison calculation with an (as most as we can) identical setup of a model of Fischer et al. (2009), result are presented in Section 4.3.

As another improvement over the existing models in the literature, we also model the genuinely multi-dimensional effect of proto neutron star convection via the mixing-length treatment, and explore the resulting changes of the neutrino signal.

4.1 Simulated Models

The pre-supernova progenitors are the two very compact s25.0 and s40.0 from the set in Woosley et al. (2002) and model s40s7b2 from Woosley and Weaver (1995). The last progenitor was also used by Fischer et al. (2009) and all three are included in O'Connor and Ott (2011).

4.1.1 Equation of state of high density matter

Of particular importance for simulations near the threshold of instability is the choice of the high-density equation of state (EoS), for which astrophysics is dependent on theoretical models given to us from nuclear physics.

For most of our models we have chosen the EoS of Lattimer and Swesty (1991 and Lattimer et al., 1985), using the version with a nuclear incompressibility parameter of $\mathsf{K} = 220\,\mathrm{MeV}$ ("LS220"). To compare with Fischer et al. (2009) we also produced a model with the $\mathsf{K} = 180\,\mathrm{MeV}$ version ("LS180"), which has since fallen somewhat into disgrace with the measurements of a stable $\sim 2\,\mathrm{M}_{\odot}$ neutron star, for which at least the $\mathsf{K} = 220\,\mathrm{MeV}$ version has to be used, a value that is also more in agreement with measurement from nuclear physics (see e.g. references in Steiner et al., 2013).

We would like to emphasize again that for typical supernova simulations with less massive neutron stars the choice between LS180 and LS220 is not overly important, as they are very similar for hot proto neutron star configurations away from the maximum mass instability threshold. See also the comparison in Section 3.4.5.

4.1.2 Neutrino opacities

Each progenitor was simulated both with the full set of neutrino opacities as given in Table 2.1 and with a reduced set of reactions, where pure neutrino-neutrino pair reactions as described in Buras et al. (2003a) were omitted and the nucleon opacities were treated using the formulation of Bruenn (1985); Mezzacappa and Bruenn (1993b), that is they neglected nucleon correlations at high densities and the neutrino energy exchange via nuclear recoil. Runs with the reduced set of opacities have an "r" appended. All models suffer from the defect described in Section 3.4.6, the omission of the effect of the nucleon potentials in the neutrino-nucleon opacities at high densities. This should not be overly important here, the effect of the nucleon potentials is most important for the diffusive neutrino contribution from the proto neutron star, and thus visible only on the long timescales associated with its cooling. It should not be relevant for the comparatively short simulations discussed here. Next to that, black hole forming scenarios necessarily have a strong accretion and an accompanied neutrino luminosity from there, which originates from much lower densities. There, the effect of the nucleon potentials is negligible. Additionally, the higher temperatures encountered in the strongly compressed black hole forming proto neutron stars also quenches the impact of the nucleon potentials, see also

Table 4.1: A selection of quantities at the moment of core-bounce, the compactness parameter $\zeta_{2.5}$, the radius (r_{sh}) and enclosed baryon mass (M_{sh}) of the shock at the moment of core-bounce, and the collapse duration t_{col}.

Model		ls180			ls220		
	$\zeta_{2.5}$ [1]	r_{sh} [km]	M_{sh} [$\mathrm{M}_\odot$]	t_{col} [s]	r_{sh} [km]	M_{sh} [$\mathrm{M}_\odot$]	t_{col} [s]
s25.0	0.33				11.17	0.441	0.455
s25.0r	–”–				11.19	0.441	0.456
s40.0	0.26				11.15	0.441	0.409
s40.0r	–”–				11.19	0.442	0.407
s40s7b2	0.59	11.19	0.429	0.378	11.14	0.434	0.409
s40s7b2r	–”–	11.21	0.430	0.379	11.20	0.437	0.410
s40s7b2r$\nu\nu$	–”–	11.08	0.487	0.367			

the later Section 5.4.

4.1.3 Convection Approximation

For all progenitors, an additional simulation using the full set of neutrino opacities and also with the mixing-length scheme active was done, indicated by an appended “c”. For details of the implementation, see Section 2.4.1.

In total, 12 simulations were performed, 9 with the LS220 and 3 with LS180 equation of state.

4.2 Theoretical considerations

A direct collapse without first forming a neutron star is prevented by the strong nuclear forces, and as we have seen in Section 3.2, the initial mass of the proto neutron stars is predominantly a function of the high density equation of state and not of the progenitor initial mass or compactness. In Table 4.1 we give an overview of the proto neutron star radii and masses at the moment of core-bounce.

Thus, subsequent mass growth by accretion after a proto neutron star was formed in the centre will ultimately be responsible for the black hole formation.

Contrary to the physics determining the related Chandrasekhar mass for the instability of electron-degenerate matter, the conditions for the collapse of neutron star matter are only poorly constrained, ranging from $\sim 2-3$ solar masses.

The Tolman-Oppenheimer-Volkoff (TOV) equation,

$$\frac{\mathrm{d}p(r)}{\mathrm{d}r} = -\frac{G}{r^2}\left(\rho_e(r) + \frac{p(r)}{c^2}\right)\left(M + \frac{4\pi p(r) r^3}{c^2}\right)\left(1 - \frac{2GM(r)}{c^2 r}\right)^{-1}, \tag{4.1}$$

describes static, spherically symmetric solutions of the Einstein field equations for a given equation of state, relating pressure p to the total mass-energy density $\rho_e = \rho + e/c^2$, with ρ the matter density, e the internal energy. Here, $M(r)$ is the *gravitational mass* felt at the coordinate radius r, which has to be solved alongside Eq. (4.1), and is formally defined by

$$M(r') = \int_0^{r'} \mathrm{d}r\, 4\pi\rho_e(r)r^2. \tag{4.2}$$

Even though this looks remarkably like the classical, Newtonian definition of the enclosed mass, the integration is not over the proper volume element, the amount of mass-energy contained in the configuration, i.e. the total amount needed to assemble the configuration from unbound matter at infinity, is given by

$$M_\infty(r') = \int_o^{r'} \mathrm{d}r\, \frac{4\pi\rho_e(r)r^2}{\sqrt{1-\frac{2GM(r)/c^2}{r}}}. \tag{4.3}$$

This results from the fact that the proper distance s of the Schwarzschild metric that is necessary for calculating the physical volume element is related by

$$\mathrm{d}s = \frac{1}{\sqrt{1-\frac{2GM(r)/c^2}{r}}}\,\mathrm{d}r, \tag{4.4}$$

to the coordinate radius r. Note that the area A of a sphere with $r = \mathrm{const}$ is still

$$A = 4\pi r^2, \tag{4.5}$$

in the curved space of the Schwarzschild metric, and it is this quantity and the associated radius r that a number of neutron star measurements are sensitive to (e.g. X-Ray thermal emission on a photosphere identified with the neutron star's surface). It is therefore common to take the coordinate radius r as "the" radius, e.g. when showing mass-radius relations.

A third definition of mass one commonly encounters is the so-called *baryonic mass*, proportional to the number of baryons contained within a given radius r',

$$M_\mathrm{bar}(r') = \int_0^{r'} \frac{4\pi n_\mathrm{B}(r)m_\mathrm{B}r^2}{\sqrt{1-\frac{2GM(r)/c^2}{r}}}\mathrm{d}r, \tag{4.6}$$

with n_B the local baryon number density, and m_B a fixed, fiducial baryon mass. It is not so much a real "mass" but really only a measure for the *number* of baryons contained. It is very often used, though, as in GR only the baryon number is a conserved quantity, contrary to mass and energy, which also are actively decreased by the emitted neutrinos in a cooling proto neutron star. With $dr < ds$ and $n_B m_\mathrm{B} < \rho_e$, one has

$$M < M_\mathrm{bar} < M_\infty. \tag{4.7}$$

As it turns out, no hydrostatic solutions with a total mass exceeding a certain critical mass can be found, instead, configurations with more mass can only be

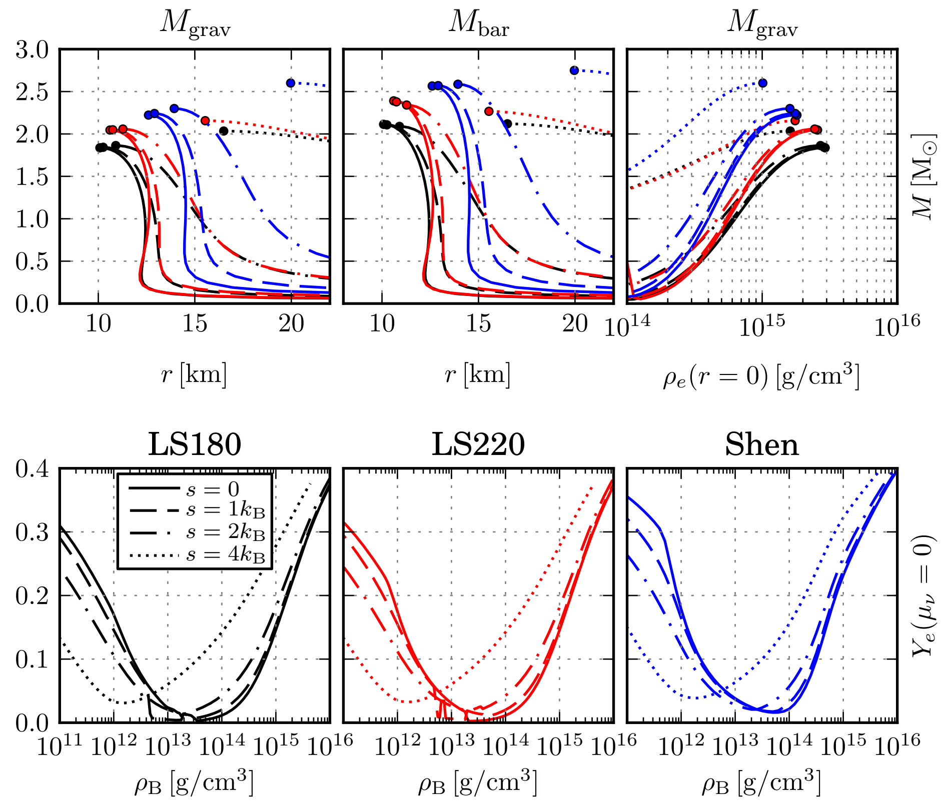

Figure 4.1: Mass-radius and mass-central density relations are shown in the upper panels, the last stable masses are marked with a dot. The lower panels gives the β-equilibrium Y_e values from the three different equations of state, for cold and three selected hot configurations (Colours distinguishing the three EoS in the upper panels as given by the lower panels).

expressed by solutions with a black-hole singularity in the centre. In Figure 4.1, one can see this for the LS180 and LS220 equations of state, as well as for the Shen equation of state which was used in the previous chapter. There, we plot the key quantities total mass and radius for families of TOV solutions by varying the initially chosen central density up to the value for which a maximum mass is found. Next to the usually depicted curves for a completely cold configuration valid for old neutron stars, we also show the relations for a hot structure, in which we assume the medium to have a constant specific entropy throughout, in this case for 1, 2 and extreme 4 k_{B} per baryon. The remaining state variable, the electron fraction Y_e, was derived by assuming that the star is in neutrino-less β-equilibrium, i.e. Y_e was inverted for a given density ρ and entropy s such that the electron neutrino chemical potential $\mu_\nu(\rho, s, Y_e)$ vanishes. The resulting β-equilibrium Y_e value can be found in the lower panels of Figure 4.1.

It is not immediately clear – although often stated – that additional thermal

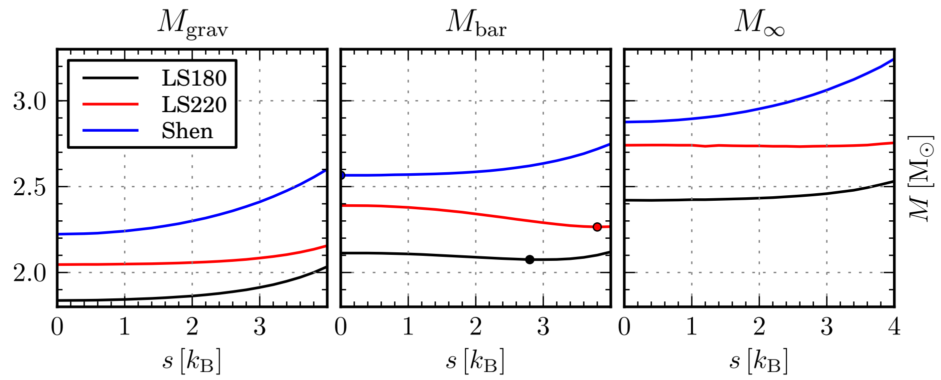

Figure 4.2: The influence on thermal energy on the maximum stable masses, as a function of the value of an assumed flat entropy profile for the whole neutron star. As can be seen, for the two LS EoS, a hot neutron star can support a somewhat smaller maximum baryon number (*mid panel*) compared to a completely cold configuration, minima are indicated with a dot. The effective gravitational mass (*left panel*) and total mass-energy contained in the neutron star (*right panel*) increase monotonically with the entropy.

Table 4.2: Numerical values for the maximum stable neutron star masses, corresponding to Figures 4.1 and 4.2

EoS		$M_{\rm grav}$	$M_{\rm bar}$	M_∞
LS180	s=0	1.837	2.113	2.421
	s=2.8	1.899	2.075	2.452
	s=4.0	2.034	2.120	2.531
LS220	s=0	2.046	2.390	2.741
	s=3.8	2.135	2.265	2.749
	s=4.0	2.156	2.267	2.755
Shen	s=0	2.223	2.566	2.876
	s=4.0	2.601	2.749	3.244

pressure support inevitably increases the maximum baryonic mass. There are two competing effects, on the one hand additional thermal pressure should support more mass, on the other hand, the thermal energy is itself an additional source of mass-energy in the Einstein equations. Keil and Janka (1995) already noted that these effects overall resulted in a very small increase of the maximum stable mass for their particular EoS.

It is not possible for us to resolve whether this is realistic or an artefact of deficiencies in the high density equation of state models.

And indeed, as can be seen in Figure 4.2, additional thermal energy does not always increase the maximum baryonic mass. For the two Lattimer&Swesty EoS, the maximum baryonic mass can be reduced by 0.038 and 0.125 solar masses, for LS180 and LS220, respectively. Only for even higher entropies do the maximum baryonic masses increase again, while in the Shen EoS, the maximum baryonic mass increases monotonically with entropy. In Table 4.2 we also give the corresponding numerical values.

4.3 Comparison to a full GR simulation in the literature

Model s40s7b2 using the LS180 EoS was also simulated by Fischer et al. (2009). In their Figure 2, they present neutrino luminosities and rms-mean energies. We therefore produced three models, one with our full opacity set and one with the reduced rates according to section 4.1.2 and finally, as Fischer et al. (2009) also discuss neutrino pair-reactions ($\nu\nu \leftrightharpoons \nu\nu$, Buras et al., 2003a), for a third model we also ran a simulation with our reduced opacity set but with $\nu\nu$-pair reactions include (model "ls180-s40s7b2r$\nu\nu$"). Unfortunately, it is not immediately clear from the description in Fischer et al. (2009) whether they make use of neutrino pairs rates for the s40s7b2 progenitor, nor if they include weak-magnetism, which they also discuss in a section in their paper.

In Figure 4.3, we show the accretion of mass-shells, the shock and proto neutron star formation, and the evolution of the matter temperature up until the final black hole collapse for model ls180-s40s7b2, as a representative case. The continuous heating of the proto neutron star's mantle around an enclosed mass shell of $\sim 1\,\mathrm{M}_\odot$ due to compression by the ongoing accretion, is visible, as well as the final, very fast collapse of the whole proto neutron star at the end.

To compare our neutrino signal with Fischer et al. (2009), recall from Eq. (3.4) that we define as the normal mean energy $\langle\varepsilon\rangle$ the neutrino energy density J over neutrino number density $\mathcal{J}$,

$$\langle\varepsilon\rangle = \frac{\int J\,d\varepsilon}{\int \mathcal{J}\,d\varepsilon} = \frac{\int_{-1}^{1} d\mu \int_0^\infty d\varepsilon\, \mathcal{I}(\varepsilon,\mu)}{\int_{-1}^{1} d\mu \int_0^\infty d\varepsilon\, \varepsilon^{-1}\mathcal{I}(\varepsilon,\mu)}, \tag{4.8}$$

where $\mathcal{I}(\varepsilon,\mu)$ is the neutrino radiation intensity. As in the previous chapter, we follow Janka and Hillebrandt (1989) and write this for arbitrary moments and in terms of the neutrino particle distribution function $f(\varepsilon,\mu)$ (using $\mathcal{I} \propto \varepsilon^3 f$) as

$$\langle\varepsilon^n\rangle = \frac{\int_{-1}^{1} d\mu \int_0^\infty d\varepsilon\, \varepsilon^{2+n} f(\varepsilon,\mu)}{\int_{-1}^{1} d\mu \int_0^\infty d\varepsilon\, \varepsilon^{2} f(\varepsilon,\mu)}. \tag{4.9}$$

The rms-mean energy as used by the Basel group (explicitly defined in e.g. Liebendörfer et al., 2005) is in this notation then

$$\langle\varepsilon\rangle^{\mathrm{rms}} = \sqrt{\langle\varepsilon^2\rangle} \tag{4.10}$$

and presumably this definition was also used in Fischer et al. (2009). Note that e.g. Keil et al. (2003) use another definition of the rms-mean energy, in their

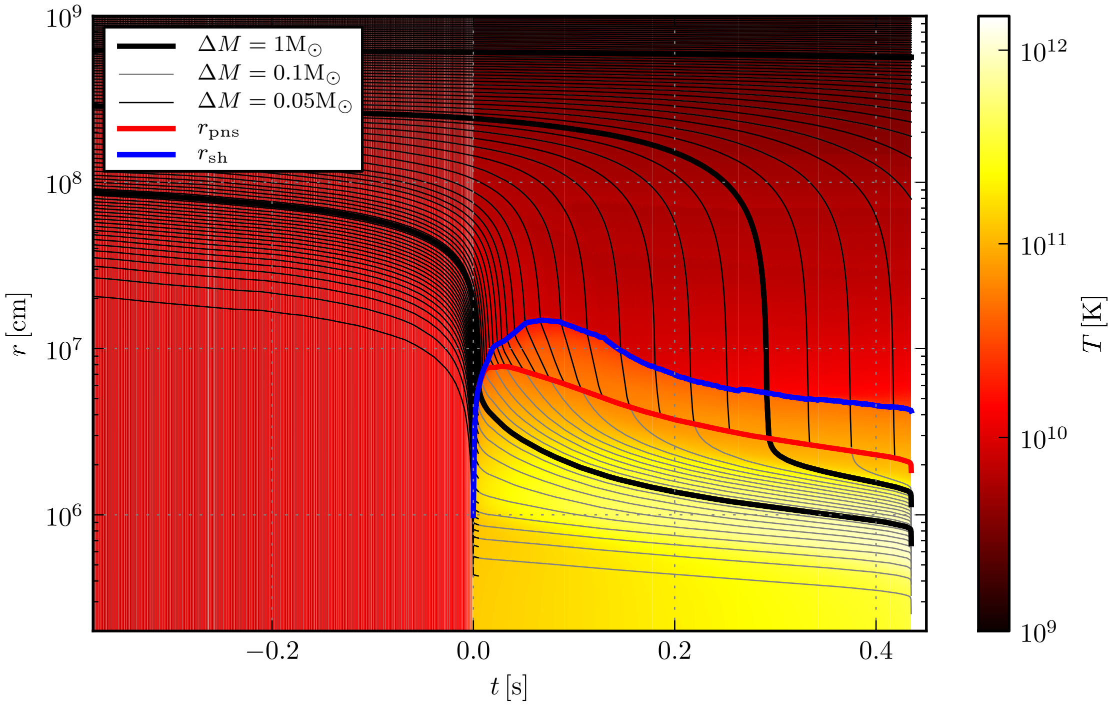

Figure 4.3: A mass shell plot of the black hole collapse of model ls180-s40s7b2. Colour coded is the matter temperature, the blue line is the radius of the accretion shock, the red line is the neutron star's surface (defined as $\rho = 10^{11}\mathrm{g/cm}^3$). The final collapse at the end of the simulations happens within a few milliseconds only.

Equation 10 they define it as

$$\langle\varepsilon\rangle^{\mathrm{rms\,Keil}} = \sqrt{\frac{\langle\varepsilon^3\rangle}{\langle\varepsilon\rangle}}. \tag{4.11}$$

As can be seen by comparing Figure 2 of Fischer et al. (2009) to our Figure 4.4, the $\bar{\nu}_e$ mean energies of model s40s7b2r$\nu\nu$ fit quite well, we are therefore confident that our definition is compatible with the one used in Fischer et al. (2009).

After a bit less than half a second accretion, the proto neutron star formed out of the progenitor s40s7b2 becomes unstable again and forms a black hole, the simulation effectively has to be stopped when the central density reached the end of the equation of state table ($\sim 10^{16}\,\mathrm{g/cm}^3$).

While the ν_e and $\bar{\nu}_e$ rms mean energies of our model ls180-s40s7b2r are very similar to the results of Fischer et al. (2009), our ν_x energies are a bit lower. Their electron flavor luminosities seem to be some $10-20\%$ higher than in our simulations for the most part, but the difference reduces somewhat during the late phase. The heavy-lepton neutrino luminosity is comparable to our values for most of the simulation except for the late-phase were it is also some $10-15\%$ larger.

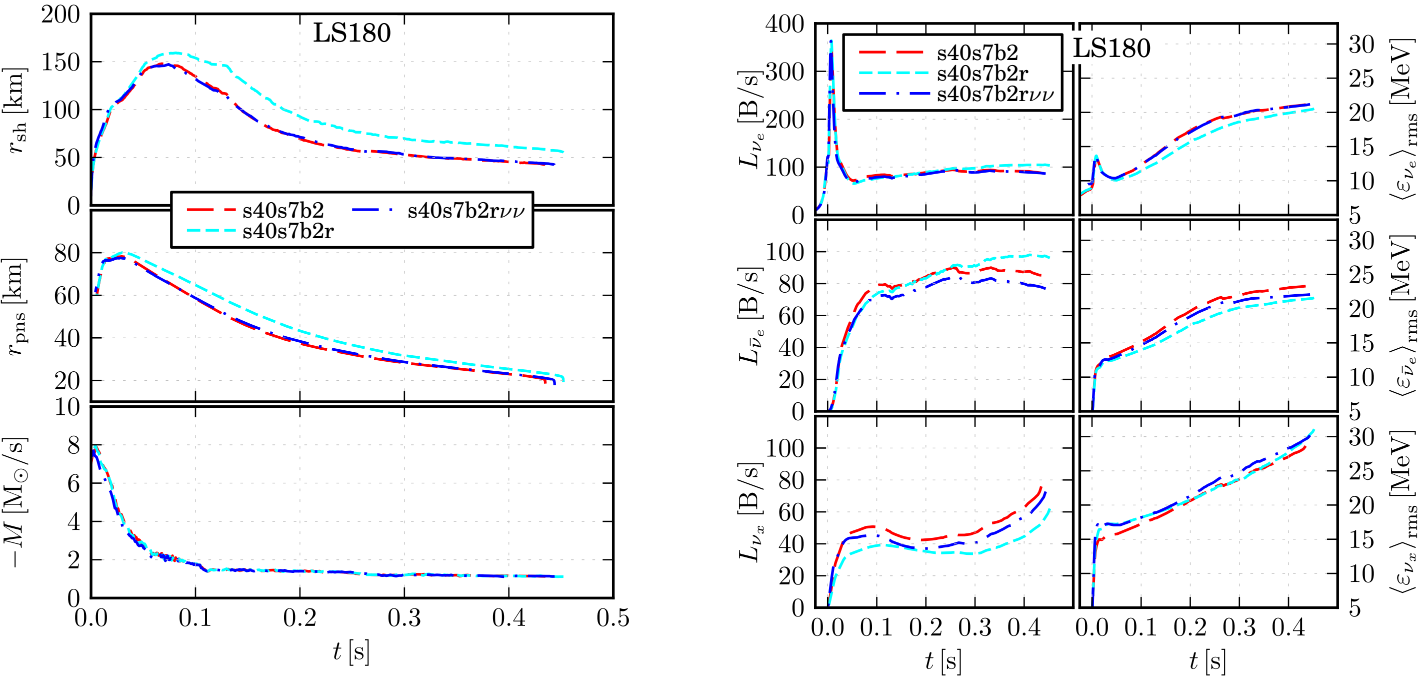

Figure 4.4: Neutrino signal and proto neutron star accretion data for a comparison run with the progenitor s40s7b2 of Woosley and Weaver (1995) and the LS180 EoS, analogous to a model in Fischer et al. (2009).

However, their heavy-lepton rms mean energies are significantly higher than we find. The source of this difference remains elusive. It could very well be connected to the numerical problem regarding numerical diffusion and the distortion of the shape of the spectrum, described in Section 3.5, although there, the rms mean energies were artificially enhanced at larger radii, making the discrepancy even worse. Other than that, it would necessitate a higher temperature in the region of decoupling for the heavy-lepton neutrinos, possibly due to a proto neutron star that is a bit more compact. A comparison of our profiles at a very compact configuration, shortly before the collapse sets in, with a solution of the TOV equation using the current mass-density and matter pressure found in our simulations as input, however, yields a very good agreement.

Purely hydrodynamically, though, the agreement with Fischer et al. (2009) is very satisfactory. It seems to be a nice testament to our approximative GR treatment via an effective potential, that the collapse sets in at a very similar time as with the full GR code of Fischer et al. (2009), 443ms after bounce for model ls180-s40s7b2r$\nu\nu$. Curiously, our full model, ls180-s40s7b2, is in even better agreement with the collapse duration, its 435ms is precisely the time Fischer et al. (2009) find for the collapse.

As will become clear in the following sections, differences in the neutrino transport and the influence of thermal energy and pressure support in the unstable proto neutron star can easily be the reason for the remaining discrepancies. Also, the details and duration of the gravitational collapse of the progenitor star could have a small influence there, see also to the discussion in Section 3.2.1, about the influence of the electron capture modelling on the collapse duration. O'Connor and Ott (2011) find a somewhat larger collapse time for the same progenitor, which they attribute to their neutrino transport approximation.

In Steiner et al. (2013), the same black hole collapse is calculated again, for a variety of high density equations of state in fact, and with the same code as used in Fischer et al. (2009). There, the authors explicitly write that they include neutrino-pair reactions, and the evolution of this model is clearly different compared to Fischer et al. (2009), with a much shorter timespan till the black hole collapse sets in.

Looking at our own models with the LS180 in comparison, we see that for this particular progenitor with its very large mass accretion rate, the inclusion of neutrino-neutrino-pair processes indeed makes quite a difference, as can be seen in the left hand side of Figure 4.4.

4.4 Neutrino signal of the LS220 models

We now turn our focus to the simulations with the LS220 high density equation of state and compare them, first regarding their neutrino transfer treatment.

The three different progenitors have quite a different density profile at the begin or, equivalently, a different mass accretion rate over the course of the simulation. The most compact s40s7b2 collapses in about half a second, the s25.0 has to accrete matter for 1.2-1.3 seconds, and the least compact s40.0 takes up to over 2 seconds until a sufficient amount of matter is collected. With the LS220 as the high density equation of state, the critical baryonic mass is about 2.25-2.3 solar masses, which indeed is significantly lower than the cold maximum mass of 2.39. In the LS180 runs, collapse sets in already at $\sim$2.18 solar masses, but contrary to the LS220 case, this value is even slightly higher than the cold maximum mass of 2.113, see Tables 4.2 and 4.3.

An overview of the resulting neutrino signal of all models can be found in Figure 4.5.

4.4.1 Influence due to Neutrino Opacities

Let us recall that models with the reduced opacity set treat neutrino-nucleon scattering as iso-energetic and neglect the possibility of neutrino-neutrino pair interactions. Additionally, in the full opacity set, the neutrino-nucleon cross sections are modified due to correlations of nucleons in the dense medium, which results in reduced opacities there (see e.g. Burrows and Sawyer, 1998; Reddy et al., 1998, 1999).

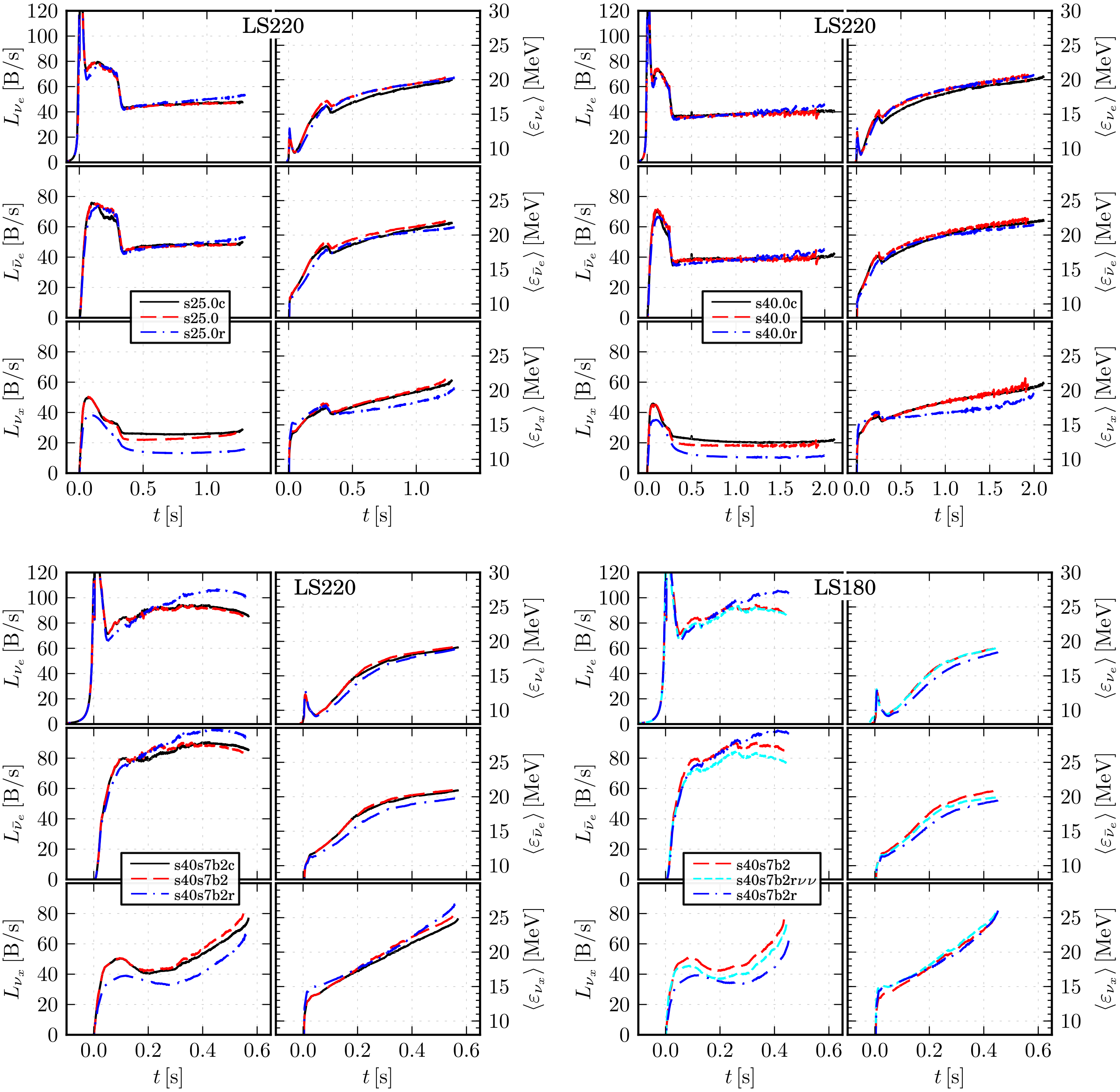

Figure 4.5: Neutrino quantities for all models. Note the different time scales, and the different equation of state for the models in the lower right panel, the comparison case for Fischer et al. (2009).

In general, runs with the full opacity set show decreased electron and anti-electron neutrino luminosities, especially at late times, while the heavy lepton neutrino luminosity is enhanced compared to models with the reduced opacity treatment, especially for the fast collapsing s40s7b2.

The situation is more complex when looking at the mean energies. In the long duration cases of s25.0 and s40.0, the electron flavor mean energies are very close, if a bit larger at times, to the values found in the reduced opacity simulations. The electron anti neutrino mean energies increase a bit more, while the heavy lepton flavor mean energies are decidedly higher.

For the very fast collapsing case of the s40s7b2, both the electron flavor neutrino mean energies are somewhat enhanced in the full simulations, while the heavy lepton neutrinos are emitted with similar, and especially close to the end of the simulation with visibly lower mean energies.

There seems to be a qualitative difference between the slow and fast collapsing cases. Fischer et al. (2009) already remarked that progenitors with low or high mass accretion rate, or correspondingly slow or fast black hole collapse, have a different electron flavor neutrino emission, which they call to be either accretion or diffusion dominated. Including pair reactions can transfer this difference also to the heavy lepton neutrinos.

Looking at the neutrino production in more detail for the case of ls220-s40s7b2 in the upper panels of Figure 4.6, we find that in the full simulation heavy-lepton neutrino flux is additionally produced in a region of density around $10^{11}\mathrm{g/cm^3}$, and not only mostly from denser regions as is the case in the reduced model. Neutrino pair production processes are responsible for this, due to the very intense accretion luminosity from the large mass accretion rate, a sizeable number of $\nu_e\bar{\nu}_e$ pairs can be annihilated into $\nu_x\bar{\nu}_x$, redistributing the energy from the electron into the heavy lepton neutrino sector.

In the long-duration cases with much lower accretion rates, for example s25.0 visible in the lower panels of the same Figure, however, this difference is not present. There, in both the reduced opacity and full opacity simulations, the bulk of the heavy-lepton flavor emission is purely from a region with very high density around $10^{13}\mathrm{g/cm^3}$.

The interplay between additional production of all flavors due to the inclusion of Bremsstrahlung and the redistribution of energy in neutrino pair reactions and the dependency of these two factors on the accretion rate seems to be the underlying reason for the differences.

Another general feature of all models with the full opacity treatment is a faster time till the black hole collapse sets in, accompanied by smaller, thus more compact, neutron stars in the full models.

4.4.2 Convection

Next to models with a reduced opacity set discussed in the previous section, for all models with the full opacity set we also ran a simulation where the mixing length

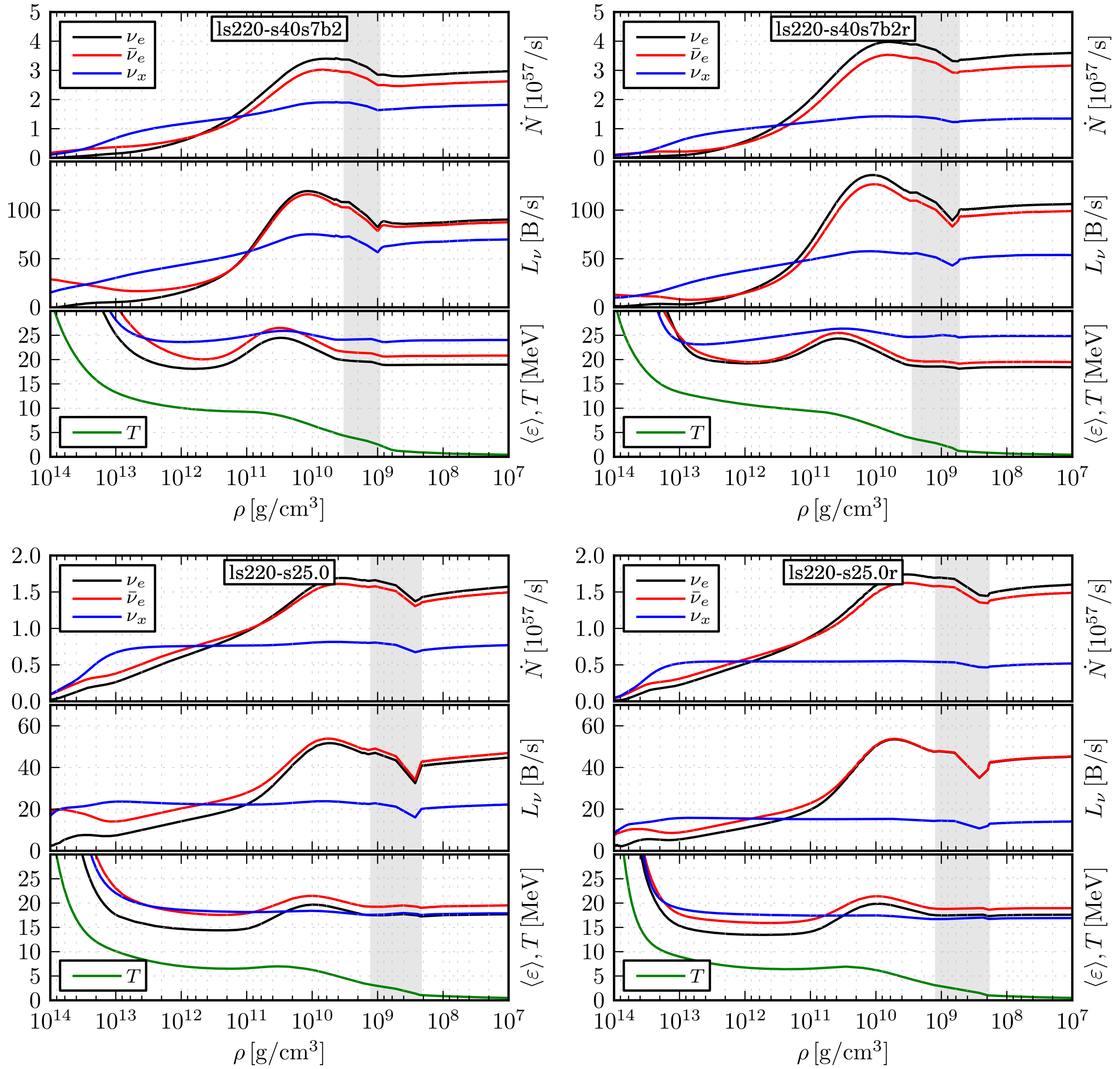

Figure 4.6: Comparison of the profiles for two simulations with s40s7b2 progenitor in the *upper* and with the s25.0 in the *lower* panels. Both models on the *left* panels are simulated with the full opacity set of Table 2.1, while the models on the the *right* were done with the reduced opacities. Shown are profiles of the neutrino flux mean energies $\langle\varepsilon\rangle_{\mathrm{flux}}$, luminosities L_ν, number flux $\dot{N}$ and the matter temperature T at a time of 0.5 seconds after bounce. Neutrinos stream out of the core at high densities on the left to lower densities on the right hand side of the plots. Only in model ls220-s40s7b2 are heavy-lepton neutrinos also vividly produced at low densities around $10^{11}\mathrm{g/cm^3}$. Shaded in grey is the accretion shock discontinuity, a region with a very small spatial extent and a strong velocity gradient. The jump in the neutrino quantities there and the gradual rise behind it is an artefact of problems with the $\mathcal{O}(\beta)$ transformation into an observer frame, and not physical.

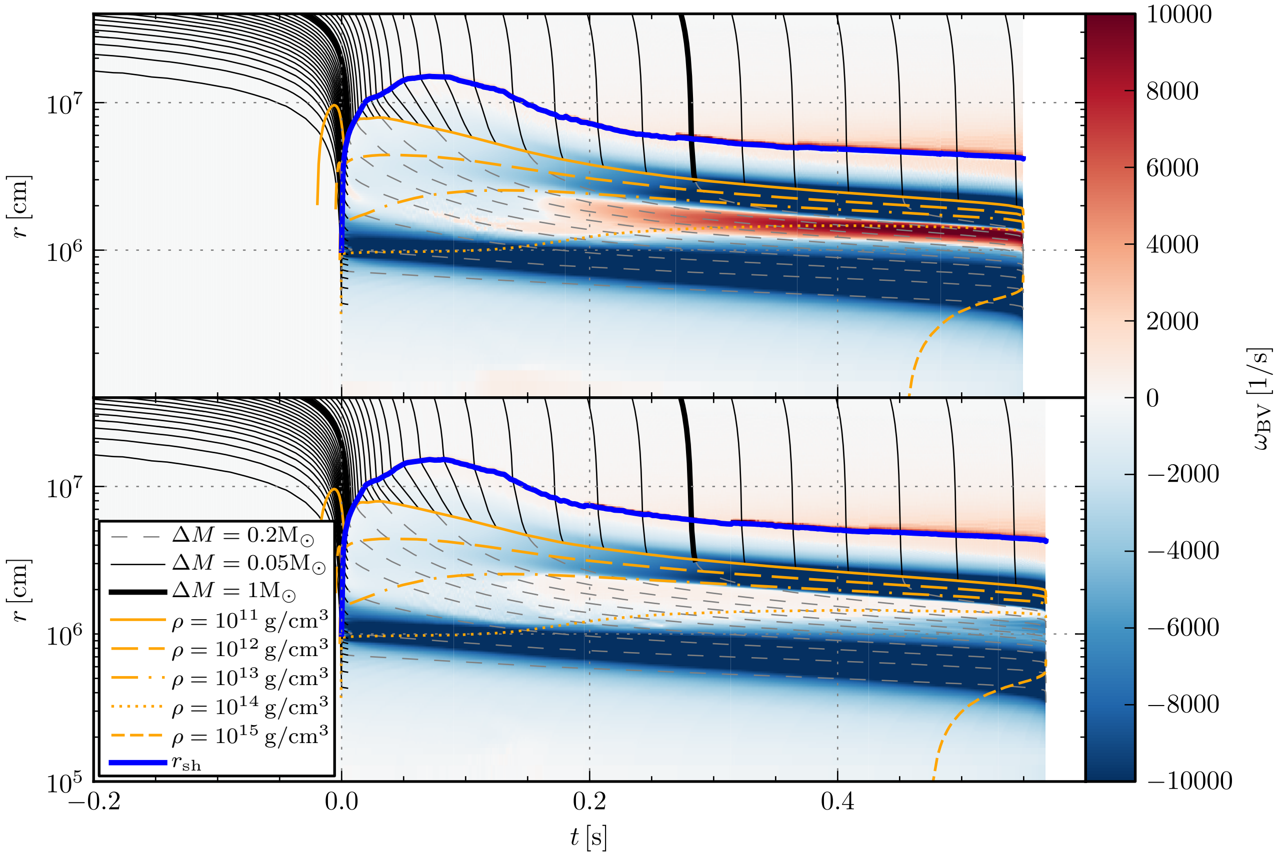

Figure 4.7: A colour plot of the Brunt-Väisälä frequency for model ls220-s40s7b2 without (*upper panel*) and model ls220-s40s27b2c with (*lower panel*) the mixing length scheme active. The lines mark mass shells of certain enclosed mass differences, density contours and the shock radius, as described in the legend.

scheme in the proto neutron star was active to mimic the effects of multidimensional convection.

In Figure 4.7, the outcome of the mixing length scheme can be seen. There, the evolution of the Brunt–Väisälä frequency ω_{BV} – a measure for the growth rate of convection, see Section 2.4 – is depicted for both a model with the mixing length convection scheme active and the corresponding model without. Areas with a convectively unstable stratification, with positive ω_{BV}, in the proto neutron star are nicely brought into a stable configuration when the additional fluxes of the mixing-length scheme are applied.

As can be seen in Figure 4.5, the effect of convection is most visible for the heavy lepton flavor neutrino signal. Their luminosity is enhanced in the long duration cases s25.0 and s40.0, whereas it is slightly reduced for the fast collapsing s40s7b2. A number of different effects are at play here: the convective models come with larger neutron stars, pushing the heavy lepton neutrinospheres outwards to slightly lower temperatures, which reduces the mean energies of the emitted neutrinos and consequently the luminosity. On the other hand, the larger radiating surface results in an enhancement of the luminosity, as does the energy transport by the convection itself. See also the discussion in the previous chapter in Section 3.3.2.

For all convective models, the time till black-hole collapse is increased, even though the neutrinos always carry away more energy in total than in the non-convective cases. Here, the sometimes destabilizing effect of thermal energy discussed before is directly reflected.

4.4.3 Neutrino signal at the moment of black hole collapse

A distinct feature in many simulations of Fischer et al. (2009) are very high heavy-lepton (rms-)mean energies at the very end of the simulation, with 30-35 MeV. Sumiyoshi et al. (2007) even find rms-mean energies exceeding 45 MeV.

Estimates for the values of mean energies and luminosities at the moment the black hole is formed and the neutrino signal vanishes could be used to measure or constrain the absolute neutrino masses (Beacom et al., 2001). The drastic values obtained in the literature are most likely an artefact of the iso-energetic neutrino-nucleon treatment.

Assuming a non-degenerate ($\eta \to 0$) Fermi-Dirac spectrum, the rms mean energy is related to the temperature at a (hypothetical) sphere of decoupling by

$$T = \sqrt{\frac{\zeta_3}{15\zeta_5}} \langle \varepsilon \rangle_{\mathrm{rms}} \approx \frac{1}{3.597} \langle \varepsilon \rangle_{\mathrm{rms}}, \tag{4.12}$$

(see Eq. 3.22). Therefore, for 45 MeV rms mean energies a temperature of $\sim$ 12.5 MeV at the heavy lepton neutrinosphere would be necessary. This is not an unreasonable temperature to be found around the region of decoupling for the heavy lepton neutrinos ($\rho \sim 10^{13}\mathrm{g/cm}^3$, as can be seen from the profiles in Figure 4.6).

However, these high energy neutrinos still have to pass the accretion layer. Without the possibility of energy-exchange, they will of course eventually be emitted with precisely this very high energy, however, physically nucleon-recoil will deplete the high energy part of the spectrum. This ingredient is especially relevant in a black hole forming scenario, where the high mass accretion rate feeds a comparatively thick scattering atmosphere around the radiating proto neutron star.

In Table 4.3, we present the neutrino mean energies and pinching parameters, extracted as described in Section 3.5, at the very end of the simulation when the black hole collapse is in progress. In the reduced opacity calculations, the isoenergetic treatment is directly visible in the anti-pinched ($p > 1$, i.e. high energy tail enhanced) spectral shape of the heavy lepton neutrinos. In the full simulations and even when only accounting for neutrino-neutrino pair reactions (model ls180-s40s7b2r$\nu\nu$), the spectra become much softer (i.e. p smaller). The

Table 4.3: Proto neutron star configuration and neutrino signal, mean energies, pinching parameter and number fluxes, right before the moment of black hole collapse. Radius and baryonic mass of the proto neutron star are defined to be the threshold $\rho = 10^{11}\mathrm{g/cm}^3$, and are from 5ms before the actual collapse. Note that N_{ν_x} is a representative number flux for one of the four heavy lepton neutrino species.

Model	LS180											
	r_{pns}	M_{pns}	t_{BH}	$\langle\varepsilon\rangle_{\nu_e}$	$\langle\varepsilon\rangle_{\bar{\nu}_e}$	$\langle\varepsilon\rangle_{\nu_x}$	p_{ν_e}	$p_{\bar{\nu}_e}$	p_{ν_x}	$\dot{N}_{\nu_e}$	$\dot{N}_{\bar{\nu}_e}$	$\dot{N}_{\nu_x}$
	[km]	[$\mathrm{M}_\odot$]	[s]	[MeV]			[1]			[10^{57}/s]		
s40s7b2r	22.3	2.184	0.452	18.5	19.5	26.0	0.92	0.91	1.01	3.50	3.08	1.49
s40s7b2r$\nu\nu$	20.8	2.164	0.444	19.0	19.9	25.7	0.93	0.92	1.03	2.83	2.41	1.77
s40s7b2	21.1	2.163	0.435	19.0	20.8	24.8	0.93	0.94	1.00	2.89	2.55	1.92

Model	LS220											
	r_{pns}	M_{pns}	t_{BH}	$\langle\varepsilon\rangle_{\nu_e}$	$\langle\varepsilon\rangle_{\bar{\nu}_e}$	$\langle\varepsilon\rangle_{\nu_x}$	p_{ν_e}	$p_{\bar{\nu}_e}$	p_{ν_x}	$\dot{N}_{\nu_e}$	$\dot{N}_{\bar{\nu}_e}$	$\dot{N}_{\nu_x}$
	[km]	[$\mathrm{M}_\odot$]	[s]	[MeV]			[1]			[10^{57}/s]		
s25.0r	16.4	2.280	1.297	20.3	21.1	20.3	0.97	0.96	1.16	1.64	1.57	0.49
s25.0	15.8	2.256	1.225	20.2	22.0	21.5	0.98	0.99	1.07	1.45	1.38	0.76
s25.0c	16.3	2.271	1.277	20.0	21.7	21.4	0.98	0.98	1.06	1.48	1.43	0.83
s40.0r	15.0	2.260	1.993	20.6	21.4	19.4	0.98	0.97	1.21	1.37	1.30	0.37
s40.0	14.4	2.242	1.930	20.7	22.3	20.9	1.00	1.01	1.11	1.17	1.11	0.57
s40.0c	14.8	2.279	2.106	20.4	22.1	21.0	1.00	1.00	1.09	1.23	1.19	0.65
s40s7b2r	20.5	2.312	0.558	18.8	19.8	26.9	0.92	0.91	1.02	3.31	2.94	1.53
s40s7b2	19.7	2.300	0.550	19.2	21.0	25.3	0.93	0.94	1.00	2.77	2.49	1.98
s40s7b2c	20.3	2.320	0.568	19.1	20.9	24.8	0.94	0.94	1.00	2.78	2.55	1.93

rms-mean energies can easily be reconstructed from p and $\langle\varepsilon\rangle$ by means of Eq (3.29) as

$$\langle\varepsilon\rangle_{\mathrm{rms}} = \sqrt{ap}\langle\varepsilon\rangle \approx 1.141\sqrt{p}\langle\varepsilon\rangle. \tag{4.13}$$

We never obtain values of $\langle\varepsilon_{\nu_x}\rangle_{\mathrm{rms}}$ above 29 MeV for models with the full opacity set.

4.4.4 Time-Integrated Emission

For the output of black hole forming core-collapse events into the diffuse supernova neutrino background, only the time-integrated emission of the neutrino signal is relevant.

Analogous to Section 3.5, we thus present time-averaged neutrino properties, as well as the time-integrated energy and neutrino numbers in Table 4.4.

Comparing the entries for progenitors s25.0 and s40.0 with the corresponding rows in Table 3.4, as they were also simulated for the first 0.5s after core-bounce in

Table 4.4: Time integrated spectral parameters for the black hole simulations, mean energies $\langle\varepsilon\rangle$, pinching parameter p, total number N and total energy E of the emitted neutrino type. The pinching parameter was inferred according to the procedure described in Section 3.5, and then time-averaged. Note that N_{ν_x} and E_{ν_x} are for only one of the four heavy lepton neutrino kinds, i.e. the total emitted energy is $E_{\nu_e} + E_{\bar{\nu}_e} + 4E_{\nu_x}$.

Model	LS180											
	$\langle\varepsilon\rangle_{\nu_e}$	$\langle\varepsilon\rangle_{\bar{\nu}_e}$	$\langle\varepsilon\rangle_{\nu_x}$	p_{ν_e}	$p_{\bar{\nu}_e}$	p_{ν_x}	N_{ν_e}	$N_{\bar{\nu}_e}$	N_{ν_x}	E_{ν_e}	$E_{\bar{\nu}_e}$	E_{ν_x}
	[MeV]			[1]			[10^{57}]			[B]		
s40s7b2r	13.4	16.1	18.7	0.92	0.91	1.01	2.10	1.40	0.56	45.3	35.9	16.7
s40s7b2r$\nu\nu$	13.9	16.6	19.0	0.93	0.92	1.01	1.87	1.20	0.64	41.7	31.8	19.3
s40s7b2	13.8	17.1	18.3	0.93	0.92	0.98	1.91	1.23	0.71	42.2	33.7	20.9

Model	LS220											
	$\langle\varepsilon\rangle_{\nu_e}$	$\langle\varepsilon\rangle_{\bar{\nu}_e}$	$\langle\varepsilon\rangle_{\nu_x}$	p_{ν_e}	$p_{\bar{\nu}_e}$	p_{ν_x}	N_{ν_e}	$N_{\bar{\nu}_e}$	N_{ν_x}	E_{ν_e}	$E_{\bar{\nu}_e}$	E_{ν_x}
	[MeV]			[1]			[10^{57}]			[B]		
s25.0r	15.3	17.9	17.1	0.95	0.94	1.07	3.07	2.33	0.85	75.1	66.8	23.4
s25.0	15.3	18.5	17.7	0.95	0.96	1.02	2.84	2.13	1.17	69.6	63.2	33.1
s25.0c	15.0	18.2	17.6	0.95	0.95	1.01	3.02	2.24	1.32	72.8	65.5	37.2
s40.0r	15.9	18.3	16.7	0.96	0.96	1.10	3.52	2.78	1.02	89.6	81.7	27.2
s40.0	15.8	18.8	17.4	0.97	0.97	1.04	3.38	2.65	1.44	85.2	79.6	40.2
s40.0c	15.7	18.7	17.6	0.97	0.97	1.03	3.73	2.88	1.71	93.8	86.2	48.3
s40s7b2r	14.1	16.7	19.7	0.92	0.91	1.01	2.50	1.73	0.69	56.4	46.2	21.8
s40s7b2	14.4	17.7	19.2	0.93	0.93	0.98	2.28	1.54	0.91	52.5	43.6	27.9
s40s7b2c	14.4	17.6	18.8	0.93	0.93	0.98	2.37	1.59	0.93	54.4	44.9	28.1

Chapter 3 for the LS220 EoS, one can nicely see that the very high mean energies are a result of the late phase due to the increasingly hotter and more compact proto neutron star.

Yang and Lunardini (2011) use the results of Sumiyoshi et al. (2007) (as they are presented in Figure 5 of Nakazato et al., 2008, note also the corresponding erratum in Nakazato et al., 2009) for estimating the detection rate of black hole forming core-collapse event in megaton neutrino detectors. The corresponding model W40S of Sumiyoshi et al. (2007) uses the s40s7b2 with the Shen equation of state and a correspondingly longer collapse duration of about 1.35s, it should therefore be best compared with our long-duration cases and not directly with our model using the same progenitor.

The model used by Yang and Lunardini (2011) was selected as it is the most optimistic case with regard to both the cumulative emitted and mean neutrino energies. For that model, Nakazato et al. (2008) gave a total neutrino energy output exceeding 500 B and a mean neutrino energy of 23.6 MeV (with a definition compatible with Eq 3.4). None of our various cases can come close to these values. Note that the Shen equation of state used by Sumiyoshi et al. (2007) will result in larger, less compact neutron stars, which would only tend to further reduce the mean energies compared to a simulation with the LS220 or LS180.

Model W40L presented in Nakazato et al. (2008) with the same progenitor but with the LS180 EoS results in a total emitted neutrino energy of more than 200 B, with a mean neutrino energy of 20.2 MeV. This model can directly be compared with this work. Using the values in Table 4.4 for the corresponding case ls180-s40s7b2r (which would best fit their neutrino treatment), we find a total energy of ~ 150 B and a mean neutrino energy (of all emitted neutrinos) of 16.1 MeV. The values from our best simulation, ls180-s40s7b2 using the full opacity set, result in ~ 160 B total energy, 16.6 MeV per neutrino.

Sadly, in light of our less favourable results it looks as if the previously deduced potential detection rate in Yang and Lunardini (2011), of already only about one event per decade, is unrealistically large.

4.5 Summary

We followed the long accretion phase and subsequent black hole collapse of three very compact progenitors which are likely candidates for these kind of events.

It could be demonstrated that our pseudo-Newtonian code with an approximate inclusion of the main effects of general-relativity via a TOV-like gravitational potential can reproduce fully relativistic simulations from the literature quite well.

As an improvement over existing spherically symmetric simulations of the neutrino signal associated with a black-hole collapse, we could demonstrate the impact of differently advanced neutrino opacities, especially the influence of non-iso-energetic neutrino nucleon interactions. With our full set of neutrino opacities, we can not reproduce the very large mean energies found in previous studies in the literature, which e.g. were used to estimate the likelyhood of detection such an event with neutrino detectors.

Additionally, we also used the convection method discussed in the previous chapter, which has minor, but still measurable influence on the neutrino signal. Convective models presented with somewhat more thermal, a bit less “pinched” spectra, a somewhat larger total emitted neutrino energy and number, and took a slightly longer time until the proto neutron star collapses to a black hole.

Black hole forming core-collapse events still produce neutrinos with very high mean energies and will thus be an important contribution to the diffuse “supernova” neutrino background. The neutrino emission of the three different progenitors simulated here could serve as templates to determine this contribution more quantitatively.

5 Proto neutron star cooling

From observations we know that at least in a certain fraction of cases a supernova occurs after a proto neutron star was formed. Somehow, the delayed neutrino heating mechanism succeeded in depositing enough energy in the material above the proto neutron star to launch an explosion.

This will quench the accretion flow and push out the material, stripping the proto neutron star of its thick, surrounding atmosphere. Subsequently, the accretion part of the neutrino emission will cease, leaving the "core" part from the cooling proto neutron star's surface itself.

Over the next few tens of seconds, the neutrinos will carry away all the energy and excess lepton number of the compact central object. Without the pressure of the accretion layer, the neutrinos even manage to deposit enough energy in absorption and scattering reactions to unbind material from the proto neutron star's surface and expel it outwards, in what is called the "neutrino driven wind".

The composition of this wind of expelled material is interesting regarding nucleosynthesis, and is regarded as a potential site for the r-process, see e.g. Woosley et al. (1994) and references therein. For this to happen, a neutron rich outflow is necessary. And indeed, the material at the proto neutron star's surface is obviously initially very neutron rich – but from energetic considerations, it can be shown that its final composition is purely determined by the electron and electron anti-neutrino emission: in order to unbind the material, the gravitational potential energy difference has to be absorbed by a nucleon via neutrinos. For the neutron star itself this is precisely its binding energy, and is about 10% of its energy (roughly the difference between M_{bar} and M_{grav} discussed in Section 4.2). Thus to unbind a nucleon with mass of 1GeV, an energy of $\mathcal{O}(100\,\mathrm{MeV})$ has to be absorbed by each nucleon. With mean neutrino energies of $\mathcal{O}(10\,\mathrm{MeV})$ this would then require $\mathcal{O}(10)$ isospin changing absorptions, leaving no trace of the initial character of the nucleon.

Therefore, it could just as well be all protons that get lifted initially from the proto neutron star's surface. An accurate prediction of the electron neutrino signal is thus key for determining the nucleosynthetic outcome.

Next to that, also the bulk of neutrino energy and number is radiated away in these tens of seconds of proto neutron star cooling. For a nearby, galactic, supernova this tail of the neutrino signal will be observed in current terrestrial neutrino detectors with $\mathcal{O}(10^3)$ events. Such a measurement would allow to look directly at the newly formed proto neutron star, uniquely probing the high density matter and neutrino physics at work there. Indirectly, every successful core-collapse supernova also contributes to the so-called diffuse supernova neutrino background flux, the sum over all distant supernova neutrino bursts happening in the visible universe, see e.g. Beacom (2010) for a review. Even though it becomes less and less likely to detect the more and more diluted burst of ever more distant supernovae, their increasing number with the growing distance adds up in a total flux that just might be detectable even with current detectors. The currently best limit on this flux is due to the non-detection by the Super-Kamiokande collaboration (Malek et al., 2003).

Historically, proto neutron star cooling has been studied for a long time. With a grey diffusion neutrino scheme, Burrows et al. (1981) and Burrows and Lattimer (1986) already noted that the "cooling"-phase is initially dominated by a heating, as the trapped neutrinos of the mantle diffuse not only outwards but also in the relatively cold, low-entropy centre. They followed the proto neutron star cooling for tens of seconds, and already remarked that convection in the proto neutron star will have important effects on the neutrino signal. Another type of convection in the form of so-called neutron-fingers – now no longer thought to exist – was discussed by Wilson and Mayle (1988) as means for a robust neutrino explosion mechanism.

A number of authors ran simulations of proto neutron star cooling with a grey diffusion neutrino transport scheme. Keil and Janka (1995) investigated the effect of a delayed hadronic phase transition in the proto neutron star at a few times nuclear density, in connection with the time-distribution of the SN 1987A neutrino signal and a potential black hole collapse of the proto neutron star after a few seconds.[1] Subsequently the influence of particular high density phases such as Kaon-condensates, hyperons, or quarks on the proto neutron star cooling neutrino signal were investigated (e.g. Pons et al., 2001). Keil et al. (1995) used proto neutron star cooling simulations to infer constraints on the neutrino nucleon opacities from the SN 1987A neutrino measurements. In a very prudent work, Pons et al. (1999) took care to calculate the neutrino opacities consistently with the underlying high density equations of state used in their models. They found that the decay constant of the neutrino luminosity at late times is then sensitive to these high density physics models.

All of these studies were done in spherical symmetry (1D), as most of the axially symmetric (2D) simulations focused more on the multidimensional effects on the accretion layer and its potentially helpful effect for an explosion. Thus, many either ignored the neutrino transport or cut-out a large potion of the proto neutron star's core due to computational costs (e.g. Burrows and Fryxell, 1992, 1993; Janka and Müller, 1996). A notable exception is the work by Keil et al. (1996), which includes the whole proto neutron star and made use of a ray-by-ray neutrino diffusion scheme. They were able to simulate up to two seconds of the proto neutron star's evolution and could directly observe the convection in the unstable stratification in the core, which they found to persist over the whole simulated time span.

With a much more accurate Boltzmann neutrino transport, Fischer et al. (2010)

---

[1] No compact remnant at the site of SN1987A has been found so far

simulated the self-consistent explosion of an Oxygen-Neon-Magnesium core star – a special progenitor which ends its life with a very thin envelope and that thereby consistently explodes even in spherically symmetric simulations – as well as more massive progenitors that were exploded with artificially enhanced neutrino opacities. They followed the subsequent cooling over many seconds and raised first doubts about the viability for the neutrino driven wind as a candidate site for the r-process, as they found a proton rich wind composition.

In Hüdepohl et al. (2010), we followed up on that, simulating the same low mass progenitor. A proton rich outflow was also found, and the importance of the neutrino opacity was investigated. Compared to the results of Fischer et al. (2010), our comparatively more sophisticated neutrino interactions (roughly coinciding with what was called "reduced" and "full" opacities in the previous two chapters) resulted in very different neutrino energies and faster cooling time scales.

Roberts et al. (2012b) used a grey neutrino diffusion scheme similar to Pons et al. (1999) on slowly-varying, hydrostatic proto neutron stars, with the addition of a mixing length convection treatment very similar to the one introduced in Section 2.4. They found a direct, potentially observable influence of the high density nuclear properties on the neutrino signal, namely the parameter J (see Eq. 2.8), the density derivative of the nuclear symmetry energy. Due to their setup, however, they could not make detailed predictions about neutrino spectra or the resulting neutrino driven wind.

Meanwhile, another topic relevant for the proto neutron star cooling appeared: as noted by Martínez-Pinedo et al. (2012) and Roberts (2012), and highlighted again in Roberts et al. (2012a), the nucleon background potentials were neglected in the rates of Bruenn (1985) and Burrows and Sawyer (1999). In their results, the effect on the cooling signal was large, in Martínez-Pinedo et al. (2012) even to the extent that slightly neutron rich outflows were found.

We therefore included the necessary corrections into our nucleon opacities and looked into this as well.

5.1 Models

We use four selected progenitors of the models that were advanced to 0.5s after core-bounce from the set discussed in Chapter 3. That way we start with somewhat realistic proto neutron star profiles resulting from an extended accretion phase prior to a potential explosion.

For each of the four progenitors we simulate four individual model runs, both with and without the mixing length convection scheme and additionally with and without the inclusion of the nucleon potential effects that were previously ignored in our neutrino nucleon opacities (see the discussion in Section 3.4.6).

This allows a comparison not only with previous results in the literature but also enables to judge the importance of these two ingredients.

Next to that, all simulations are done with both the Shen as well as the LS220 high density equation of state, giving a total set of 32 simulations. An overview of the model set and the configuration of the proto neutron star at the end of the simulations and the total emitted neutrino energies can be found in Tables 5.1 and 5.2. The total emitted neutrino energy provided there is also given as a fraction of the available gravitational binding energy, derived from a cold TOV solution with the relevant EoS and given baryon mass at the end of the simulation. Next to that, also the net total radiated (electron) lepton number in the table is compared to the theoretical expectation from the difference in lepton number enclosed by the final proto neutron star's mass at the start of the simulation minus the expected lepton number contained in the TOV solution.

These fractions serve as a measure of the completeness of the individual simulation, due to computing time constraints, not every simulation could be advanced to equally cold and deleptonized states (so far). They are also a nice consistency check of the total energy and lepton number conservation of our code over this very long timespan (numerically divided into $\mathcal{O}(10^5 - 10^6)$ time-steps), the most advanced simulations indeed approach, and never exceed, the expected binding energy and lepton number to within a few percent.

5.2 Initiating the Explosion

As self-consistent spherically symmetric models do not explode except for a few exceptional cases on the very low-mass end of progenitors, the explosion has to be initiated in some artificial way.

This can be achieved by artificially enhancing the neutrino opacities, as has been done e.g. in Fischer et al. (2009). The drawback is that the resulting neutrino signal is invariably tainted to some degree by that procedure. This is especially relevant when discussing the neutrino driven wind phase following the explosion, where the details of the neutrino signal sensitively influence the outflow composition.

We thus refrain from playing with the opacities and take an approach that is more drastic further out but less artificial for the proto neutron star itself: We artificially reduce the material density in the infall-region by a large factor (10-40), thus "ripping-off" the bulk of the hull of the progenitor. When the region with the reduced density passes the accretion shock, the resulting drop in ram-pressure leads to a shock-expansion, a corresponding increase in the advection time, resulting in more neutrino-heating, and thus invariably to a run-away explosion.

While this might seem like a rather brutal approach, for the proto neutron star this is actually precisely what would happen in an actual explosion scenario, which would equally quench the mass accretion rate.

Genuinely multi-dimensional effects, such as localized down-flows that can still happen even after an explosion is already under way, can of course not be modelled with this simple approach.

Effectively, starting from a radius of 500km we reduce the density by a factor that increases linearly with radius over a large region, typically 2000km, after which

Table 5.1: Proto neutron star configuration at the end of the Shen simulations, and the total emitted neutrino energy E_ν, in brackets also as a fraction of the available gravitational binding energy for an ideal TOV solution with that baryon mass. Lastly, the total radiated net Lepton number N_L, also given as a fraction of the theoretical expectation from a TOV solution.

Model	r_{pns} [km]	M_{pns} [$\mathrm{M}_\odot$]	t_{end} [s]	E_ν [B] [1]	N_L [10^{56}] [1]
s11.2	14.9	1.365	10.7	164 (0.97)	5.99 (0.98)
s11.2c	14.9	1.365	10.3	163 (0.97)	6.00 (0.98)
s11.2o	14.9	1.365	13.8	162 (0.96)	5.91 (0.97)
s11.2co	15.0	1.365	10.1	162 (0.96)	5.85 (0.96)
s25.0	15.0	2.031	16.5	372 (0.99)	8.37 (0.97)
s25.0c	15.3	2.031	10.7	371 (0.99)	8.48 (0.98)
s25.0o	15.3	2.031	13.8	353 (0.94)	7.72 (0.90)
s25.0co	17.6	2.031	3.6	279 (0.74)	7.96 (0.93)
s27.0	15.1	1.758	13.3	276 (0.98)	7.50 (0.98)
s27.0c	15.0	1.758	11.8	277 (0.99)	7.52 (0.98)
s27.0o	16.3	1.758	6.0	223 (0.80)	6.45 (0.84)
s27.0co	17.4	1.758	3.5	213 (0.76)	7.02 (0.92)
s40.0	15.1	1.908	14.3	324 (0.98)	7.99 (0.97)
s40.0c	17.0	1.904	4.3	273 (0.83)	7.94 (0.97)
s40.0o	15.2	1.906	15.4	318 (0.96)	7.60 (0.93)
s40.0co	17.2	1.905	4.0	256 (0.78)	7.57 (0.92)

the reduction factor stays constant, see Figure 5.1 for an example. It then takes the material about 10-20ms to fall from 500km through the accretion shock, about 250ms for the outer 2500km. That way, over time an ever larger reduction in the mass accretion rate is felt by the shock, until the conditions for run-away are met, it is pushed outward and the neutrino driven explosion is launched.

5.3 Influence of the Convection

As discussed already by Roberts et al. (2012b), the term with the Y_e derivative in the Ledoux-criterion, which we recall from Eq. (2.34) as

$$C_{\mathrm{ledoux}} = \left(\frac{\partial \rho}{\partial s}\right)_{p,Y_e} \frac{\mathrm{d}s}{\mathrm{d}r} + \left(\frac{\partial \rho}{\partial Y_e}\right)_{p,s} \frac{\mathrm{d}Y_e}{\mathrm{d}r} > 0, \tag{5.1}$$

Table 5.2: Same as Table 5.1 for the LS220 models.

Model	r_{pns} [km]	M_{pns} [$\text{M}_\odot$]	t_{end} [s]	E_ν [B]	E_ν [1]	N_L [10^{56}]	N_L [1]
s11.2	13.4	1.362	10.2	186	(0.97)	6.33	(0.98)
s11.2c	13.4	1.361	7.6	187	(0.97)	6.33	(0.98)
s11.2o	13.8	1.367	8.1	169	(0.87)	5.76	(0.89)
s11.2co	15.1	1.366	3.5	159	(0.82)	6.15	(0.95)
s25.0	13.8	2.061	5.5	334	(0.75)	7.39	(0.79)
s25.0c	14.7	2.060	4.8	382	(0.86)	9.34	(1.00)
s25.0o	16.9	2.061	1.7	213	(0.48)	6.24	(0.67)
s25.0co	16.3	2.060	2.4	272	(0.61)	7.69	(0.82)
s27.0	13.9	1.776	7.9	286	(0.87)	7.43	(0.90)
s27.0c	13.5	1.762	8.4	317	(0.98)	8.00	(0.97)
s27.0o	13.8	1.775	9.0	271	(0.83)	6.75	(0.81)
s27.0co	15.4	1.774	3.9	261	(0.79)	7.86	(0.95)
s40.0	13.8	1.926	8.0	329	(0.85)	7.71	(0.87)
s40.0c	15.4	1.926	3.8	309	(0.79)	8.56	(0.96)
s40.0o	15.6	1.928	2.5	214	(0.55)	6.06	(0.68)
s40.0co	15.7	1.927	3.5	288	(0.74)	8.20	(0.92)

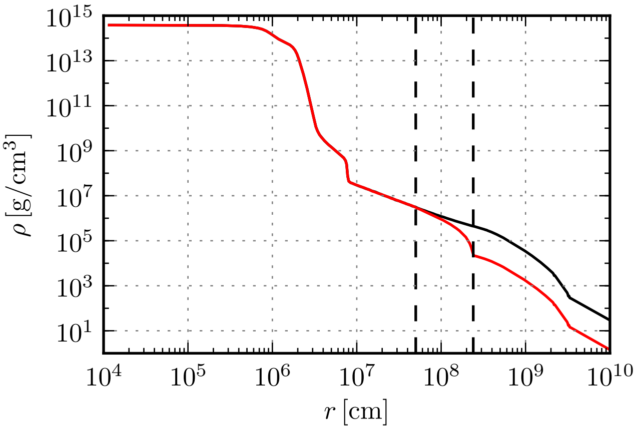

Figure 5.1: The scaled density profile to initiate the explosion, black is the original profile, red after scaling. Shown is model shen-s11.2, at 0.5s post-bounce when the explosion is launched.

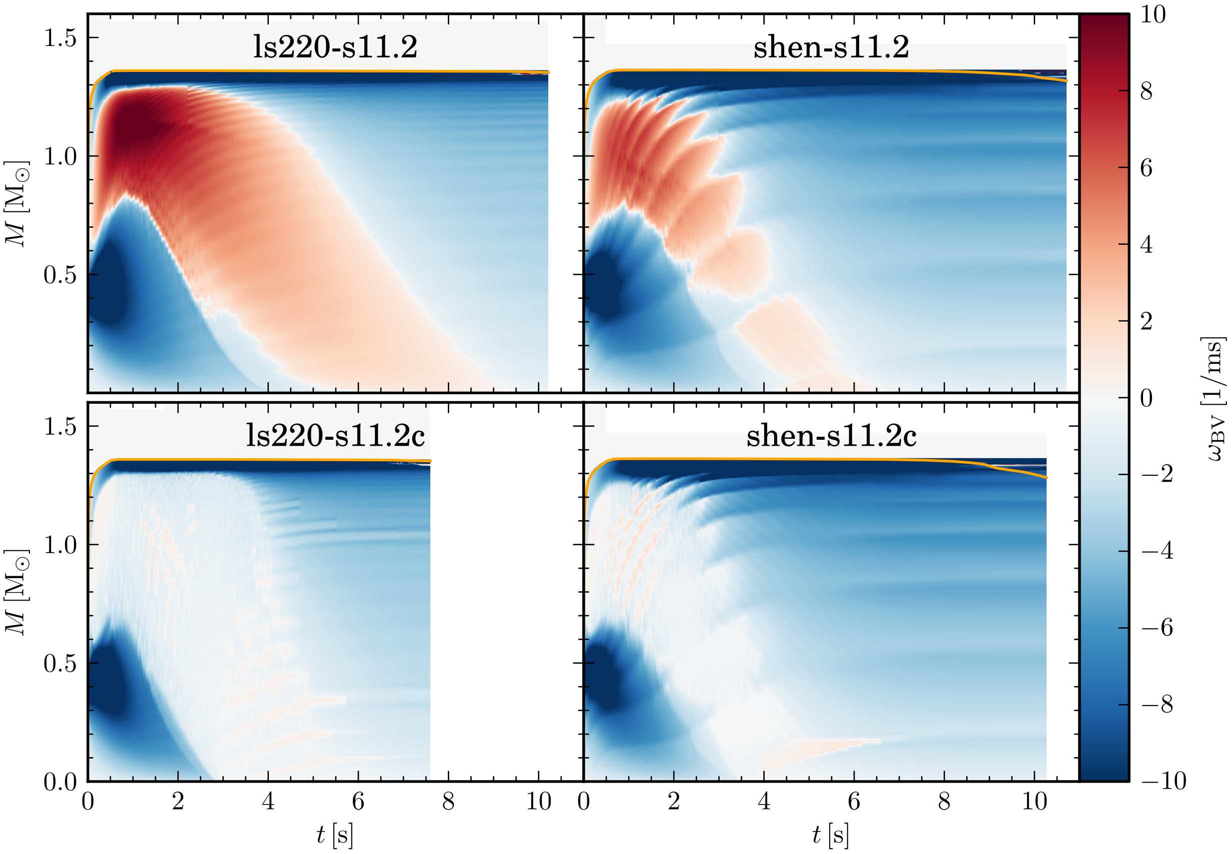

Figure 5.2: Evolution of the Brunt–Väisälä frequency for all four different models with the s11.2 progenitor. The top panels are simulations without, the lower panels with the mixing length scheme active. The orange line is the energy-averaged ν_x-sphere.

is sensitive to the high density equation of state. Specifically – and not surprisingly – to the behaviour of the symmetry energy J, a measure of the additional energy penalty due to any neutron/proton asymmetry, (see e.g. Lattimer and Swesty, 1991).

From Figure 5.2, showing the evolution of the Brunt–Väisälä frequency for four different models using the s11.2 progenitor, we can see that for the Shen equation of state, the convection happens in a much smaller mass-region than for the LS220, and persists for a shorter time.

This is in agreement with the analysis of Roberts et al. (2012b), who note that equations of state with a higher density derivative of the symmetry energy exhibit smaller convective regions. From Steiner et al. (2013) we get the relevant nuclear parameter L, defined as

$$\mathsf{L} = 3n_{\rm s}\left(\frac{\partial \mathsf{J}}{\partial n_B}\right)_{n_B=n_s, Y_e=\frac{1}{2}, T=0}, \tag{5.2}$$

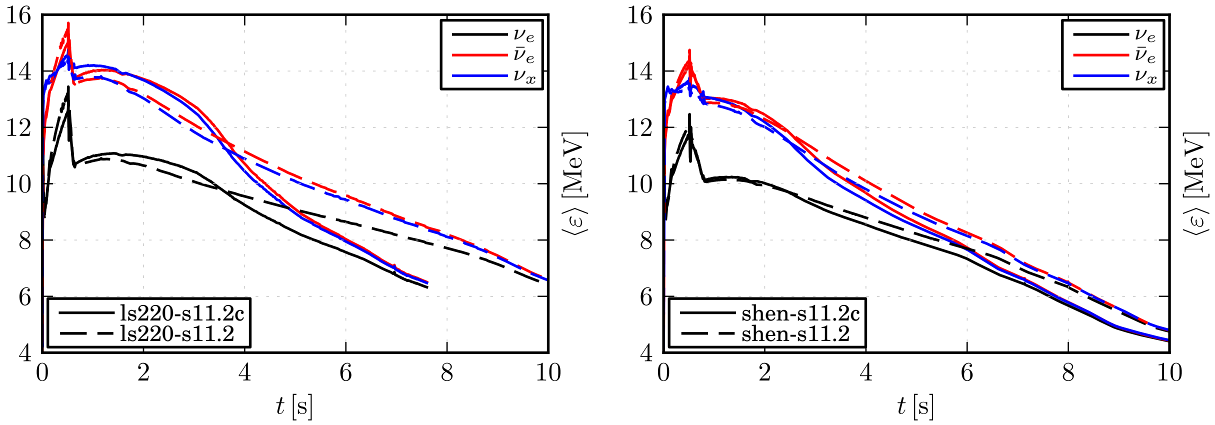

Figure 5.3: Mean neutrino energies of the s11.2 models with the LS220 (*left*) and Shen (*right*) EoS, with- and without convection.

for our two equations of state: $\mathsf{L}_{\mathrm{LS220}} = 73.82\,\mathrm{MeV}$ and $\mathsf{L}_{\mathrm{Shen}} = 110.79\,\mathrm{MeV}$.

Finally, also visible in Figure 5.2 is the effect of the mixing length scheme in the lower panels, which efficiently drives regions with positive ω_{BV} into (marginal) stability. The additional convective fluxes enhance the energy transport and visibly reduce the time necessary for the temperature maximum to reach the core. Subsequently, the whole configuration becomes stable again and can cool down.

The peculiar ripples and line-structures, especially visible in the Shen models, are not physical, but due to the gridding of the equation of state tables (where the Shen table is much more coarse). As a number of (higher) derivatives of the equation of state quantities are needed for the evaluation of the Ledoux critertion, the finite resolution of the tables is reflected in these oscillations in ω_{BV}. The resulting lines precisely trace the contours of the density grid values of the two tables.

In Figures 5.5 and 5.6 the detailed hydrodynamical evolution of all four progenitors with both EoS and with and without the mixing length scheme is presented, namely profiles of the material density, temperature, electron fraction, entropy, and the electron neutrino optical depth as well as the net electron-neutrino fraction. Note how the negative entropy gradients are levelled, with a corresponding change in the electron fraction profiles, in order to drive C_{led} to zero. Further down, in Figure 5.14 and 5.15, the time evolution of the central values of these quantities are also shown.

With convection, the proto neutron stars are initially larger and hotter in the outer layers when compared with non-convective models, during the time of accelerated core-heating. In Figure 5.4, a visualization of the changed temperature evolution is presented, it can be seen that the convective models also increase the temperatures in the neutron star's mantle. After the convective zone has reached the centre and vanishes, the enhanced energy loss from the more energetic previous

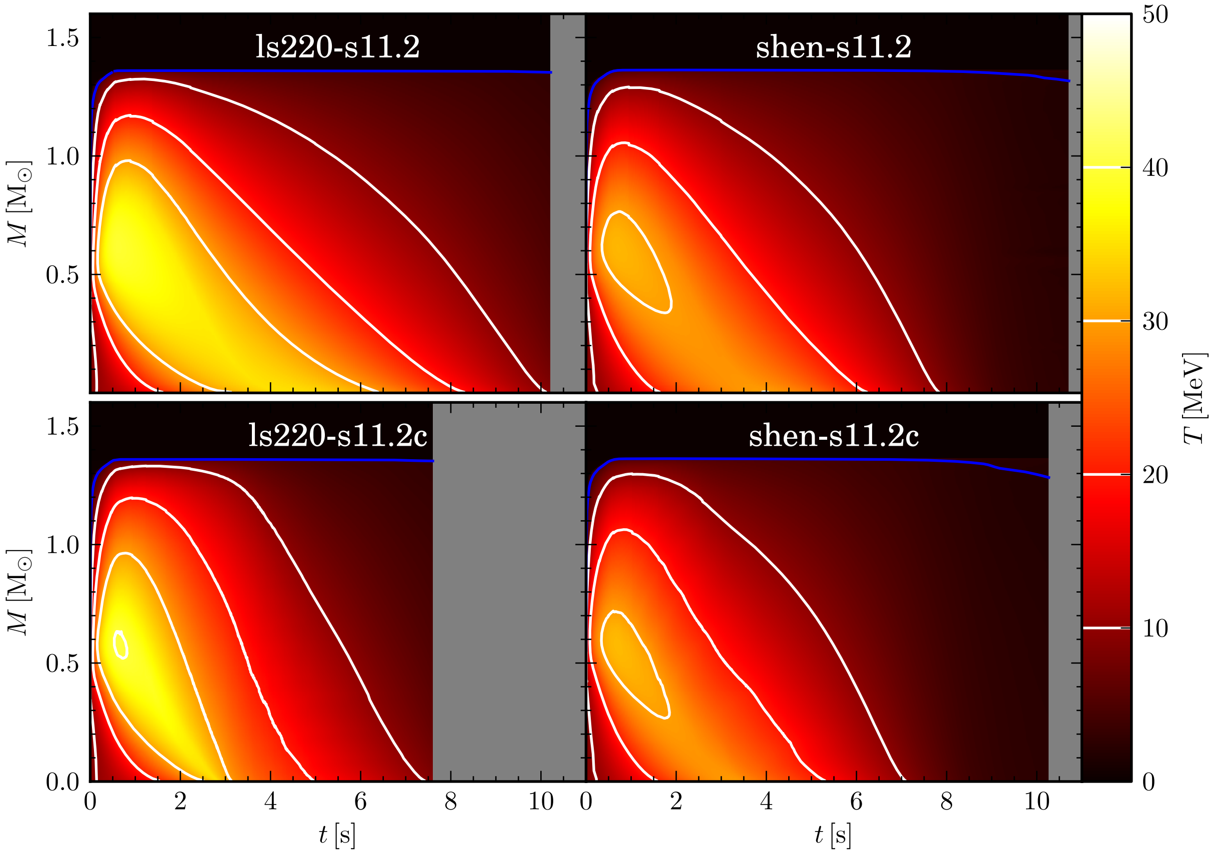

Figure 5.4: Colour coded is the temperature evolution of the four proto neutron stars with the s11.2 progenitor, as a function of the enclosed baryon mass. In the *upper* panels without, in the *lower* panels with the mixing length scheme active, for both the LS220 (*left*) and Shen (*right*) EoS. The blue line is the energy-averaged heavy-lepton neutrinosphere.

emission then results in neutron stars that are smaller and colder earlier than their non-convective counterparts. This is directly reflected in the neutrino luminosities due to the change in radiating surface and material temperature. Initially, convective models have higher luminosities, supplementing the increased energy transport outwards with a more efficient neutrino energy loss. Later, when the convection ends the luminosities drop noticeably, especially pronounced in the LS220 case. Roberts et al. (2012b) suggest that a measurement of this drop in the luminosities could be used to infer constraints on the derivative of the nuclear symmetry energy mentioned earlier. With our energy-dependent Boltzmann neutrino transfer, we can also make accurate predictions on the mean energies. As can be seen in Figure 5.3, they are also sensitive to this break.

Note that the convective region is always well inside the neutrino spheres, see

Figure 5.4, convection does not transport material directly to exposed, neutrino transparent regions. Its influence on the emitted neutrino signal is thus always only via the secondary effects of enhanced energy and lepton transport from the inside and changed proto neutron star radius and surface temperatures.

This also validates our simple mixing length ansatz here, as the more general case of convection in a semi-transparent region would certainly need a much more considerate approximation.

5.4 Nucleon opacities

As already mentioned in Chapter 3, our neutrino nucleon opacities were previously missing a term regarding the nucleon background potentials in the dense medium (Roberts et al., 2012a; Martínez-Pinedo et al., 2012), see Section 3.4.6.

It has been shown there that for the results in the previous Chapters 3 and 4, this omission was not critical. However, this is no longer true for the time scales and conditions we encounter in the proto neutron star's cooling. There, accretion ceases and the neutrino emission is now solely from the diffusion out of the dense core, where these effects are important. Also, the diffusion time scales of the neutrinos is directly affected by any change in the opacities – and the corrections arising from Martínez-Pinedo et al. (2012) are different for ν_e and $\bar{\nu}_e$.

This is especially important in regards to the neutrino driven wind ejecta, whose composition is sensitively dependent on the neutrino mean energies and luminosities, and it was hoped that the corrections could revive the possibility for at least a weak r-process in the supernova neutrino driven wind phase.

Thus we implemented these corrections into our simulation code, and ran all simulations again – also the convective model set – with these corrections included. As in the previous chapters, these are marked with a trailing "o" in their model name. The "best physics" case is the model set "co", where both the convective effects are modelled and these corrections are included.

Sadly, tests and subsequent iterations necessary to validate the corrected opacity implementation delayed the start of the simulations somewhat, therefore they are all not as far progressed as their uncorrected counterparts (a complete cooling simulation typically takes three to four months, not including the first 0.5s of accretion discussed in Chapter 3).

The corrections noted by Martínez-Pinedo et al. (2012) effectively shift the Q-value of the neutrino nucleon opacity compared to our previous treatment the difference in neutron/proton background interaction potential, $U_n - U_p$. Martínez-Pinedo et al. (2012) thus note that the neutrino and electron energies for the β-processes

$$\nu_e + n \rightarrow e^- + p, \tag{5.3}$$

$$\bar{\nu}_e + p \rightarrow e^+ + n \tag{5.4}$$

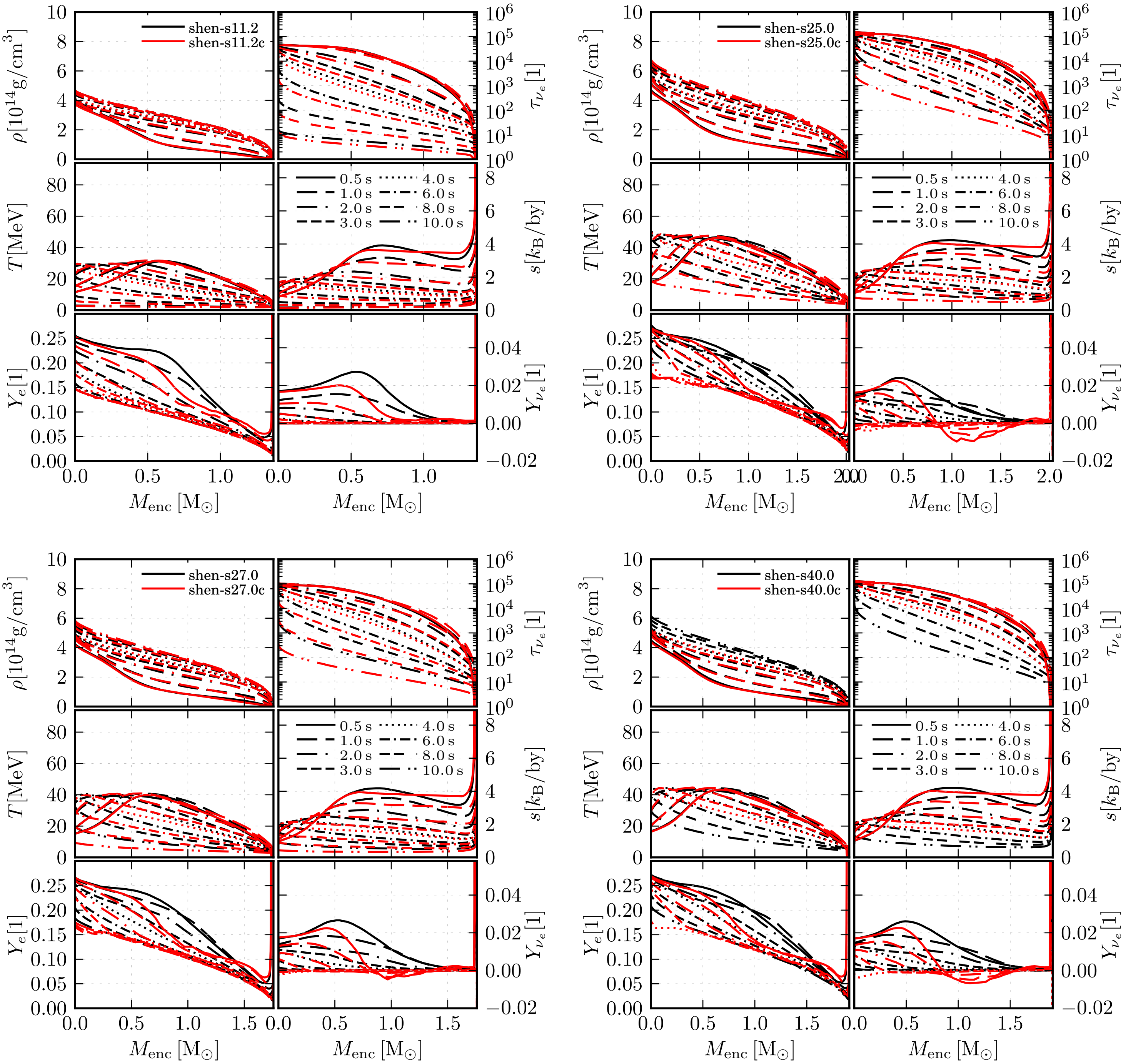

Figure 5.5: Profiles illustrating the proto neutron star cooling for the Shen models with the standard opacities, with and without the mixing length convection scheme active. Shown are the material density ρ, temperature T, electron fraction Y_e, electron neutrino optical depth τ_{ν_e}, material entropy s, and net electron fraction Y_{ν_e}.

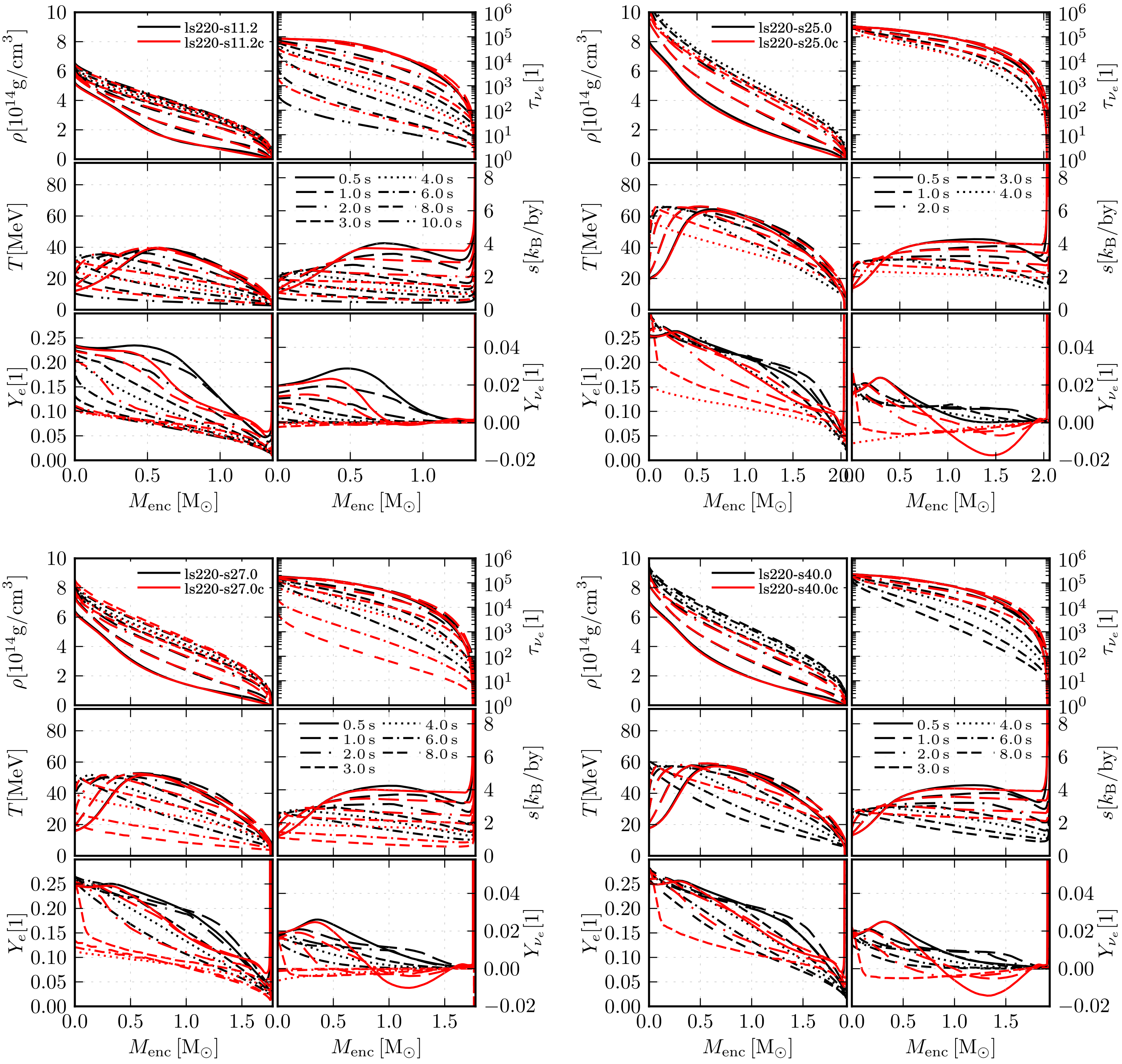

Figure 5.6: Analogous panels as in Figure 5.5 for the LS220 models.

satisfy the relations

$$\varepsilon_{\nu_e} = E_{e^-} - \Delta - (U_n - U_p), \tag{5.5}$$

$$\varepsilon_{\bar{\nu}_e} = E_{e^+} + \Delta + (U_n - U_p), \tag{5.6}$$

where $\Delta = (m_n - m_p)c^2 \approx 1.29\,\mathrm{MeV}$ is the neutron proton rest-mass difference, and $U_n - U_p$ is positive for neutron star conditions.

The effect of this is that the opacity for electron neutrino absorption on neutrons is enhanced for all energies, while the opacity for anti-electron neutron absorption on protons is reduced for low and enhanced for higher energies, for details we refer the reader to the explicit relations given in Martínez-Pinedo et al. (2012).

Another important correction to the neutrino nucleon opacities which Martínez-Pinedo et al. (2012) do not include, however, are nucleon-correlations at high densities, which we use according to the prescription given by Burrows and Sawyer (1998). As we have found in Hüdepohl et al. (2010), the effect of this on the mean energies is quite large.

Lastly, a correction for nucleon-recoil and weak-magnetism on the rates of Bruenn (1985) was included by Martínez-Pinedo et al. (2012) for neutrino-nucleon scattering. Strangely, weak-magnetism does not seem to be applied also to the charged-current neutrino absorption reactions, as the authors specifically only mention a correction of the neutral-current scattering processes, even though it has a potentially large influence on the resulting wind electron fraction (Horowitz and Li, 1999).

Martínez-Pinedo et al. (2012) then test their new opacities in a proto neutron star cooling simulation of an artificially exploded 15 solar mass progenitor (s15.0) by enhancing the neutrino opacities in the gain region, as has been done in Fischer et al. (2010). Overall, Martínez-Pinedo et al. (2012) see a slight reduction of all neutrino luminosities, decreased electron neutrino and slightly increased anti-electron neutrino mean energies, with the heavy lepton neutrino mean energy almost unchanged. With this, they find that this increased difference in luminosities and mean energies for the electron and anti-electron neutrinos is large enough to bring the ejected material even to slightly neutron-rich ($Y_e \gtrsim 0.45$) conditions early in the neutrino driven wind phase. However, the omission of weak-magnetism in the charged current neutrino absorption reactions typically underestimates the electron fraction by 20% (Horowitz and Li, 1999), which again could turn the electron fraction from slightly neutron rich to slightly proton rich. See also subsequent Section 5.8, where the neutrino driven wind is discussed.

From Table 3.3 we see that the s15.0 should yield a neutron star with about 1.7 solar masses, considering that the onset of their explosion is with 400ms quite close the 500ms simulated in Chapter 3 and that the mass accretion rate is low at these late times. The best match to compare would thus be our model shen-s27.0o (although we find only little difference in the relative impact of the nucleon potentials over the four different progenitors with the Shen EoS).

When we look at our simulations with the opacity correction – the resulting mean energies and luminosities in comparison to the old treatment are presented

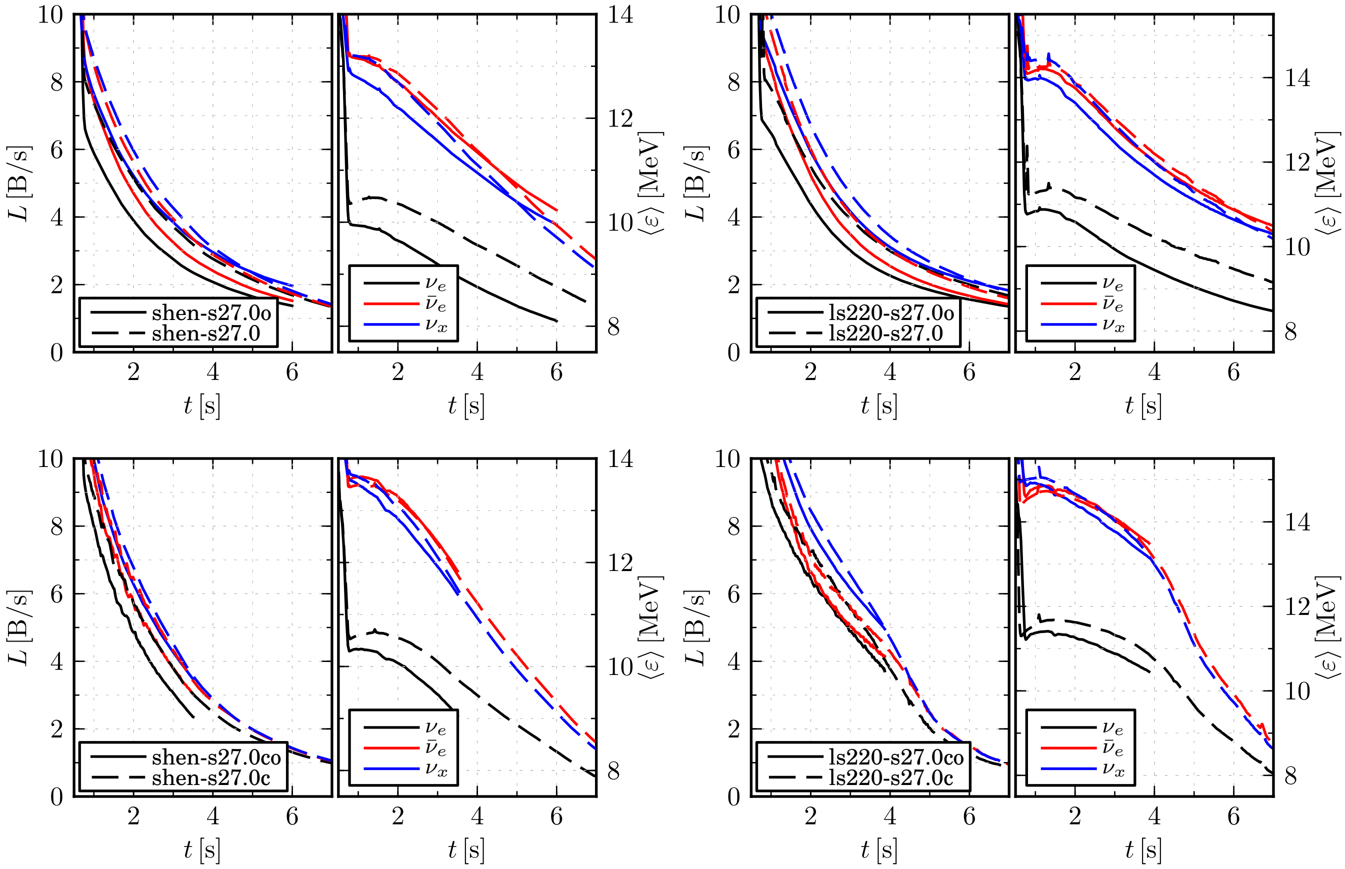

Figure 5.7: Mean neutrino energies and luminosities of the s27.0 models with the Shen (*upper panels*) and LS220 (*lower panels*) EoS, with- (*right*) and without (*left*) convection, each comparing two simulations with and without the opacity corrections.

in Figure 5.7 – we find that the inclusion of the nucleon opacities also leads to a reduction of all neutrino luminosities as seen by Martínez-Pinedo et al. (2012).

The electron neutrino mean energy is also reduced, the anti-electron neutrino energy, however, is also slightly reduced, and not increased as in Martínez-Pinedo et al. (2012). Next to that, also the heavy lepton neutrino mean energy is visibly reduced, even more so than the anti-electron neutrino energies.

Roberts et al. (2012a) present only neutrino mean energies and the resulting electron fraction evolution, and find the same general trend of reduced electron, increased anti-electron neutrino mean energies – although with their high density equation of state models used this results in a much longer time duration of $Y_e < 0.5$. In their slides to the MICRA 2013 Workshop (Roberts, 2012c, slide 16-17), however, the authors acknowledge a bug in their simulation code, and present results very similar to ours when this defect is removed: anti-electron and heavy lepton neutrino mean energies that are at some times slightly decreased or increased, but mostly unchanged, and visibly decreased electron neutrino mean energies, when compared to a simulation without the nucleon potentials included.

Note that when we include also the mixing length convection, the differences with respect to a convective simulation using the old treatment are smaller than when comparing two non-convective models. The mean energies still shift visibly, but not as much as in the non-convective case, see Figure 5.7.

This is expected, Roberts et al. (2012a) already note in their conclusions that to zeroth order, the nucleon potential difference ΔU increases the ν_e absorption by about $\exp(\Delta U/T)$ and correspondingly reduces the $\bar{\nu}_e$ absorption by a factor of $\exp(-\Delta U/T)$. Thus, a larger temperature in the outer layers as found in the convective simulations (see Figure 5.4 for the shifted temperature distribution) will reduce the influence of the nucleon potentials, which – at least for the equation of state models used here – seem predominantly a function of density and less dependent on the temperature themselves.

5.5 Time dependent Neutrino Signal and Deleptonization

In Figure 5.8 the time evolution of the total neutrino energy, that is

$$\dot{E}_{\rm tot} = L_{\nu_e} + L_{\bar{\nu}_e} + 4L_{\nu_x}, \tag{5.7}$$

as well as the net lepton number flux,

$$\dot{N}_L = \frac{L_{\nu_e}}{\varepsilon_{\nu_e}} - \frac{L_{\bar{\nu}_e}}{\bar{\varepsilon}_{\nu_e}}, \tag{5.8}$$

are shown for the simulations with s27.0 progenitor. In the convective LS220 model, deleptonization is essentially complete after a bit more than 4 seconds, and it looks as if this is not very much changed by also including the opacity corrections.

To quantify this, let us define a fractional deleptonization and cooling time, τ_n^L and τ_n^E as the time necessary to radiate away a certain amount of energy or lepton number, due to the exponential decay best expressed by powers of e as

$$\int_0^{\tau_n^E} \dot{E}_{\rm tot}\,\mathrm{d}t = \left(1 - \frac{1}{e^n}\right) E_{\rm TOV}, \tag{5.9}$$

$$\int_0^{\tau_n^L} \dot{N}_L\,\mathrm{d}t = \left(1 - \frac{1}{e^n}\right) N_{\rm L,TOV}. \tag{5.10}$$

To some extent these are influenced by the artificially selected time of explosion, but only to that order of magnitude (0.5s). Also, comparing successive time-spans gives a measure of the speed of deleptonization and cooling independent of the initial setup. Numerical values can be taken from Table 5.3, wherever the progress of the individual simulation allowed to evaluate Eq. (5.9) and (5.10).

In Figure 5.9 for the Shen and Figure 5.10 for the LS220 cases, we show the neutrino signal of the cooling of all 32 models.

Table 5.3: The fractional deleptonization and cooling times as defined in Eq. (5.10) and Eq. (5.9). Values left blank could not be evaluated as some simulations are not yet sufficiently progressed in time.

Model	LS220						Shen					
	τ_1^E	τ_2^E	τ_3^E	τ_2^L	τ_3^L	τ_4^L	τ_1^E	τ_2^E	τ_3^E	τ_2^L	τ_3^L	τ_4^L
		$[s]$			$[s]$			$[s]$			$[s]$	
s11.2	2.2	5.5	8.6	3.6	6.6		1.9	4.5	7.2	2.0	4.0	7.8
s11.2c	1.8	3.6	5.7	1.8	2.8		1.6	4.0	6.7	1.2	2.7	5.7
s11.2o	2.9	7.9		6.9			2.3	6.4	10.7	4.7	10.4	
s11.2co	1.9			2.1			1.8	5.1	9.0	1.7	8.8	
s25.0	3.2						2.7	7.1	10.9			
s25.0c	2.4			2.6	3.6	4.2	2.2	5.2	8.1	0.9	2.9	4.7
s25.0o							3.3	9.4		10.4		
s25.0co							2.3			1.2		
s27.0	2.9	7.7		6.4			2.4	6.0	9.3			
s27.0c	2.1	4.3	6.5	2.3	3.3		1.9	4.6	7.4	1.1	2.9	6.7
s27.0o	3.6						3.0					
s27.0co	2.3			2.5			2.1			1.5		
s40.0	3.1			7.9			2.6	6.7	10.4	3.6	8.2	
s40.0c	2.3			2.5	3.5		2.1			1.1	3.1	
s40.0o							3.2	8.9	13.9	9.1		
s40.0co	2.5			2.7			2.2			1.4		

The dips in the luminosity and mean energies in the convective simulations – connected to the vanishing convective zone – are nicely visible, especially for the LS220 models with their stronger convection.

Let us continue a consideration that had been suggested in Hüdepohl et al. (2010) and investigate if one could infer the proto neutron star's radius from the time dependent neutrino signal, which together with the integrated neutrino energy and lepton number could allow to constrain the high density equation of state model. As the spectra get very thermal during the cooling phase, let as assume that the total luminosity of a particular neutrino species is given by a Stefan-Boltzmann-Law,

$$L_\nu^{\mathrm{SB}}(t) = 4\pi R_\infty^2(t) \cdot \frac{7}{8}\sigma T_\nu^4 \tag{5.11}$$

with $\sigma = 2\pi^5 k_\mathrm{B}^4/15c^2h^3$ the usual Stefan-Boltzmann constant. The factor 7/8 arises from the fact that one has to integrate over a Fermi-Dirac distribution, here also assumed to have zero chemical potential, instead of the Bose-Einstein distribution for photons. With the same assumption of a thermal, $\eta \to 0$ spectrum, the neutrino temperature is related to the mean energy by

$$T_\nu = \frac{\langle \varepsilon_\nu \rangle}{3.597 k_\mathrm{B}}, \tag{5.12}$$

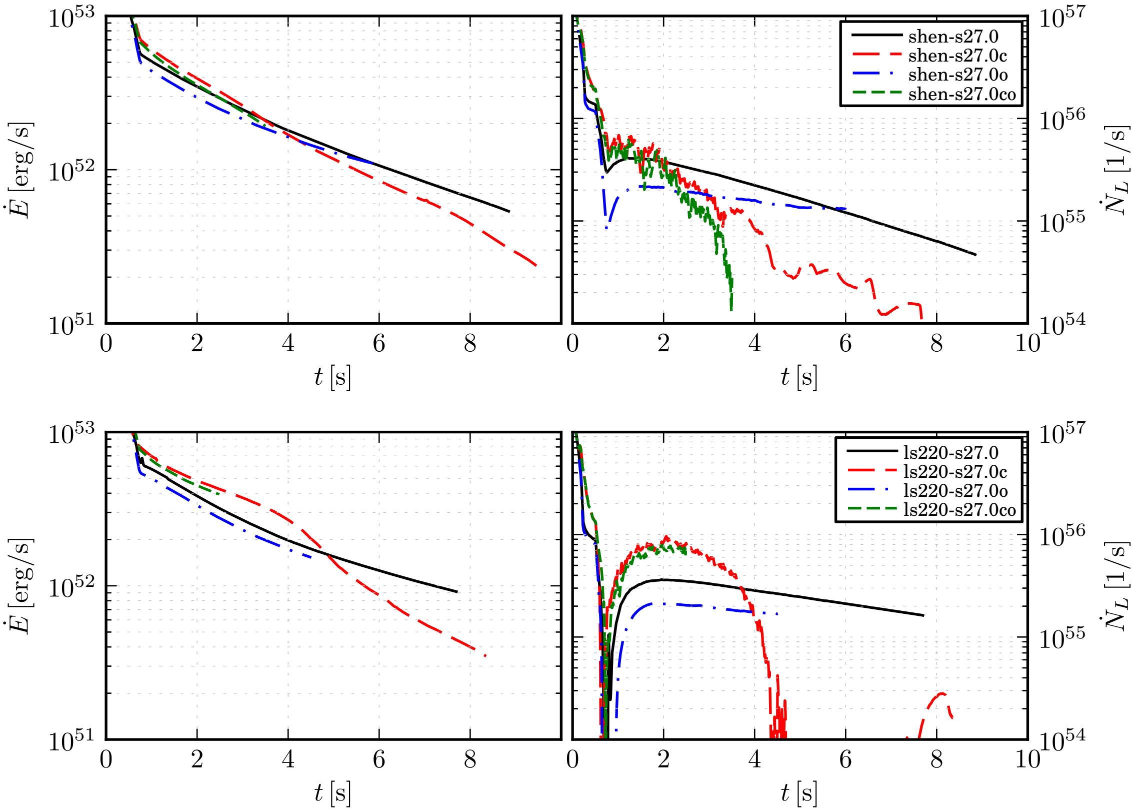

Figure 5.8: Total energy (*left*) and net lepton number fluxes (*right*) for models with the s27.0 progenitor.

as we recall from Eq. (3.22). Lastly, R_∞ is the effectively visible radius for a distant observer, due the curved spacetime this is related to the coordinate radius R of the proto neutron star by

$$R_\infty = \sqrt{1 - \frac{2GM_{\text{grav}}}{Rc^2}}R. \tag{5.13}$$

However, as our code neglects the volume and curvature effects introduced by general relativity, we will identify R_∞ with the coordinate radius as found in our simulation, and not apply Eq. (5.13). With this, we define an $\mathcal{O}(1)$ “greyness” factor measuring the deviation from a black body emission similar to Hüdepohl et al. (2010) as the ratio of our simulated neutrino luminosities to Eq. (5.11) by

$$\varphi = \frac{L_\nu}{L_\nu^{\text{SB}}}. \tag{5.14}$$

In this definition, $\varphi = 1$ would indicate a luminosity exactly corresponding to a thermal emission with the given mean energy and zero chemical potential. It

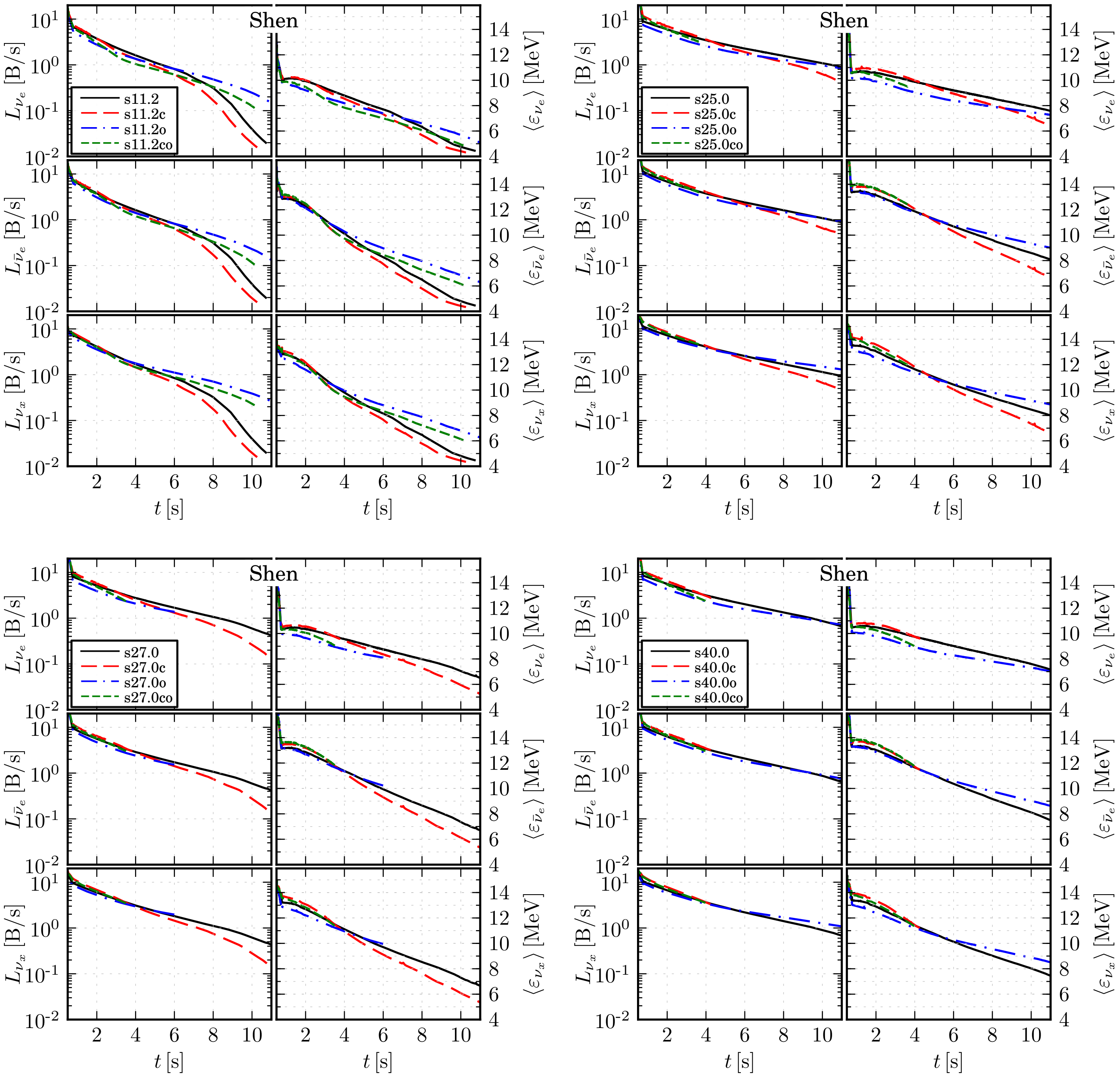

Figure 5.9: Neutrino quantities for all Shen models. Shown are the neutrino luminosities and mean energies, extracted at 500km and transformed into a resting observer's frame, also correcting for the (small) gravitational redshift. Note that L_{ν_x} is representative for one individual of the heavy lepton neutrinos, and not the sum over all four.

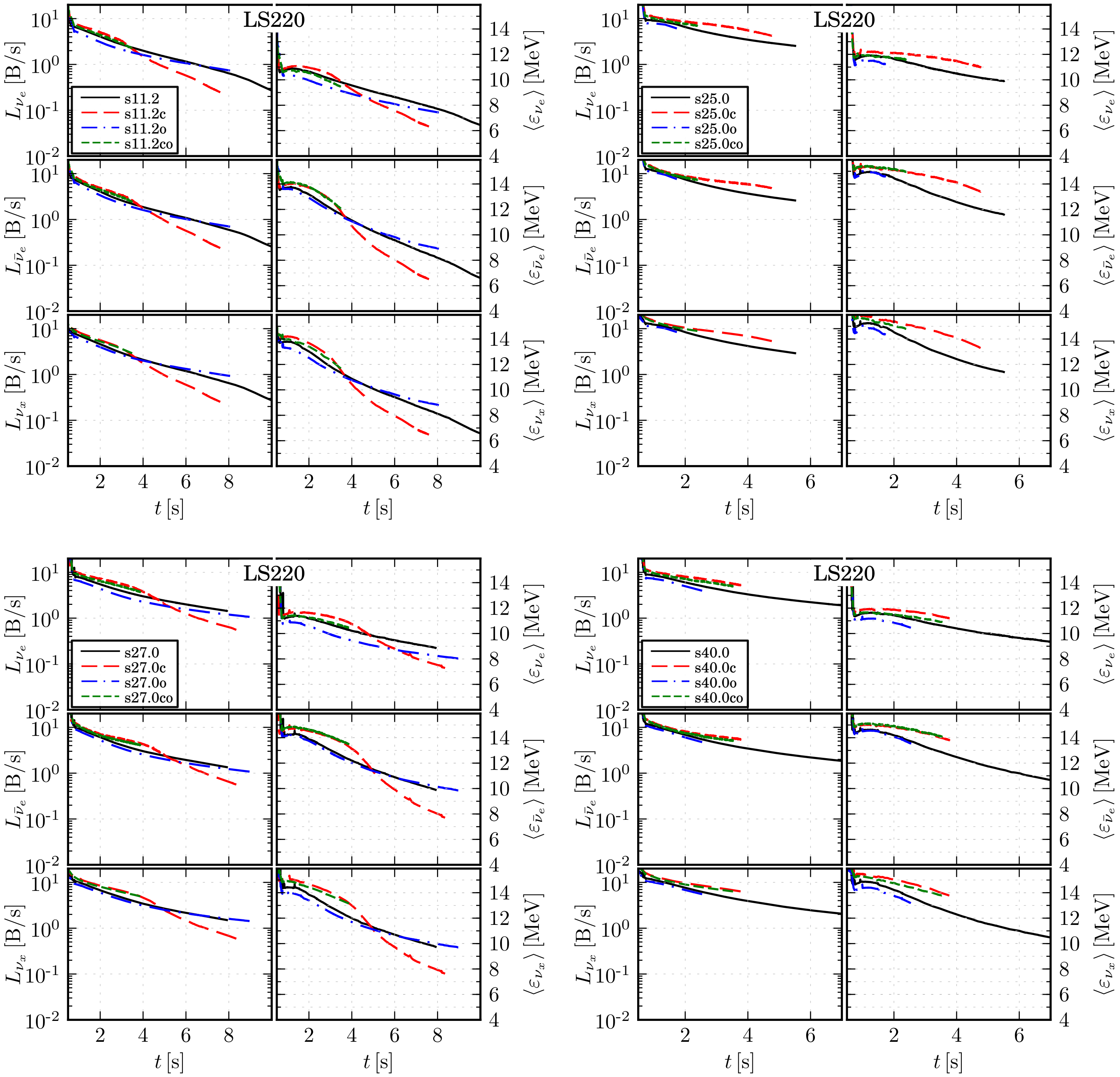

Figure 5.10: Neutrino quantities for all LS220 models, the same remarks for Figure 5.9 apply. Note the different time ranges.

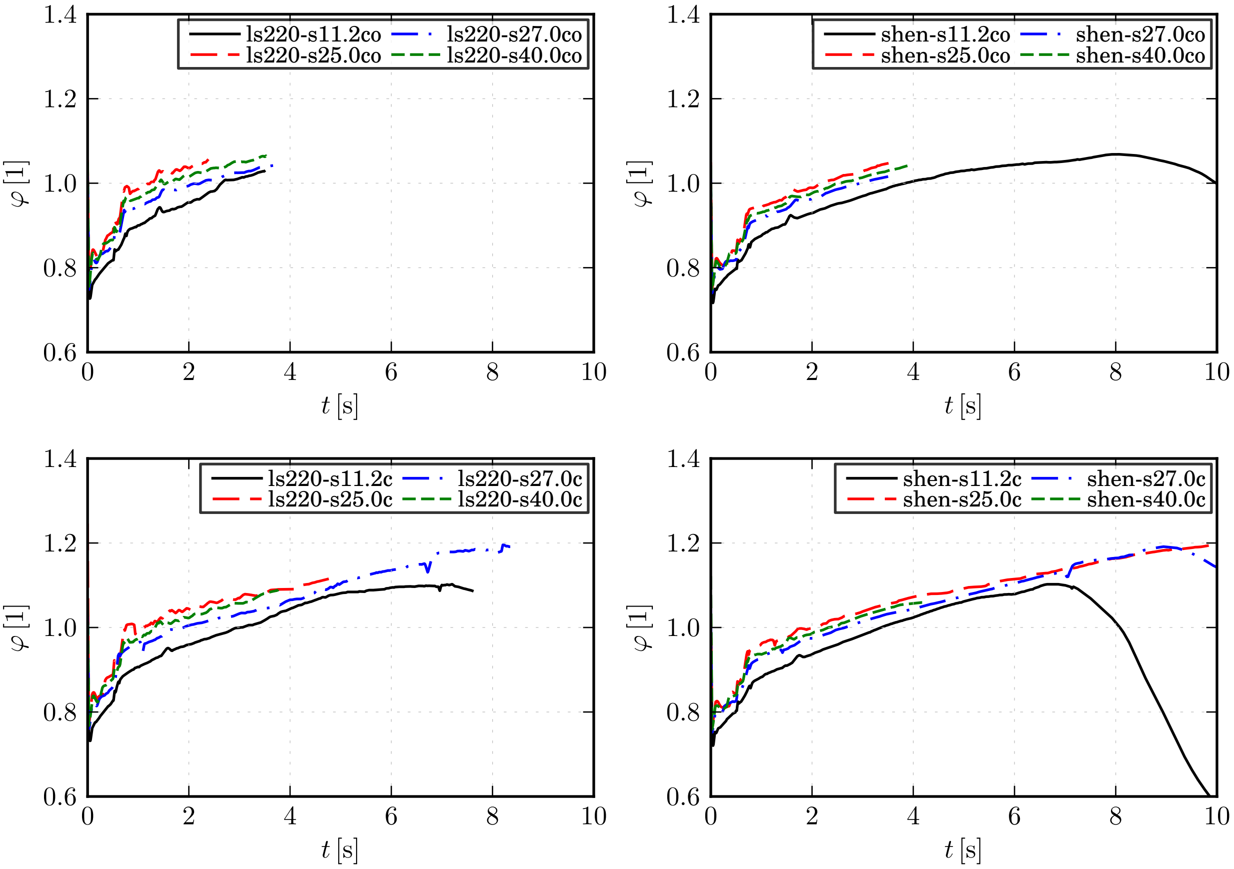

Figure 5.11: The greyness factor φ from Eq. (5.14), for the all models with the mixing length convection scheme active, in the *upper* panels with the corrected opacities, in the *lower* panels without.

is expected that collective flavor oscillations will dramatically mix the individual neutrino spectra during the cooling phase (Dasgupta et al., 2009) (while these seem to be suppressed during the accretion phase, see Sarikas et al., 2012a,b). Therefore we do not evaluate Eq. (5.14) for each individual flavor but for a mean signal over all six neutrino species. In Figure 5.11 we present the resulting values for all our models with convection, where of course the models including the opacity correction represent our "best-physics" cases. The models without those corrections might still serve as a measure of the uncertainty connected to any remaining large corrections of the neutrino opacities (or equivalently, equation of state influence).

There is a roughly 10% spread between the different proto neutron stars and also a considerable time variation of this quantity. Proto neutron star radii could thus potentially only be reconstructed to about 20% accuracy (assuming perfect knowledge of the neutrino signal).

5.6 Integrated neutrino emission

In Table 5.4, the time-integrated spectral parameters for all 32 cooling simulations can be found. Note that the first 500ms of accretion and the collapse phase are deliberately not included in order to only present the signal of a cooling proto neutron star, see Tables 3.4 and 3.5 for the earlier values. Contrary to popular belief, the usual hierarchy of

$$\langle\varepsilon\rangle_{\nu_e} < \langle\varepsilon\rangle_{\bar{\nu}_e} < \langle\varepsilon\rangle_{\nu_x} \tag{5.15}$$

is also almost never found for the time-integrated signal, instead the anti-electron and heavy lepton neutrinos have always very similar mean neutrino energies, with the hierarchy changed to

$$\langle\varepsilon\rangle_{\nu_e} < \langle\varepsilon\rangle_{\nu_x} \lesssim \langle\varepsilon\rangle_{\bar{\nu}_e}. \tag{5.16}$$

This has also been found by earlier parameter-studies of the spectrum formation (Keil et al., 2003), detailed 2D explosion simulations (Buras et al., 2006b; Marek and Janka, 2009; Marek et al., 2009) or our earlier cooling simulations of an self-consistently exploding ONeMg-core star (Hüdepohl et al., 2010), and is a robust feature emerging from the inclusion of non-thermal, energy-exchanging neutrino-nucleon scatterings for the heavy-lepton neutrinos, what has been called the "filter-effect" in Raffelt (2001).

That effect is most prominent during the accretion phase, when the neutron star has a thick scattering atmosphere. Later, though, the neutrinospheres recede further inwards, and allow this effect to become prominent again. Thus, immediately after the explosion has been launched, one typically finds $\langle\varepsilon\rangle_{\nu_x} > \langle\varepsilon\rangle_{\bar{\nu}_e}$ for some time until the growing scattering layer above the ν_x-sphere drives the mean energies down again, $\langle\varepsilon\rangle_{\nu_x} < \langle\varepsilon\rangle_{\bar{\nu}_e}$.

Consequently, also the assumption of equipartition of the total emitted neutrino energy over the six different species is only accurate to about 20%.

5.7 Hydrodynamical evolution

Even though the explosion has been launched artificially, it still exhibits the typical features of a rapidly expanding shock, the appearance of a neutrino driven wind and subsequently the formation of a "reverse-shock". There, the thin material from the wind is accelerated by the neutrinos and hits the previously ejected material from the explosion.

See Figures 5.12 and 5.13 for the evolution of the radius of shock, reverse shock, and proto neutron star as well as the mass loss rate.

The neutron star radius continually shrinks, slowly approaching its equilibrium value. As noted earlier, models with convection have initially larger, later smaller neutron stars, due to the different temperature stratification. In contrast, the neutron star radii show almost no sensitivity to the neutrino opacity correction.

Table 5.4: Time integrated spectral parameters for the cooling simulations, mean energies $\langle\varepsilon\rangle$, pinching parameter p, total number N and total energy E for each neutrino type. The pinching parameter was inferred according to the procedure described in Section 3.5. Note that N_{ν_x} and E_{ν_x} are for only one of the four heavy lepton neutrino kinds, i.e. the total emitted energy is $E_{\nu_e} + E_{\bar{\nu}_e} + 4E_{\nu_x}$.

Model	LS220											
	$\langle\varepsilon\rangle_{\nu_e}$	$\langle\varepsilon\rangle_{\bar{\nu}_e}$	$\langle\varepsilon\rangle_{\nu_x}$	p_{ν_e}	$p_{\bar{\nu}_e}$	p_{ν_x}	N_{ν_e}	$N_{\bar{\nu}_e}$	N_{ν_x}	E_{ν_e}	$E_{\bar{\nu}_e}$	E_{ν_x}
	[MeV]			[1]			[10^{57}]			[B]		
s11.2	9.9	11.8	11.7	0.97	0.99	1.00	1.28	1.06	1.18	20.2	20.2	22.0
s11.2c	10.4	12.6	12.6	0.96	0.98	1.00	1.17	1.00	1.08	19.4	20.2	21.8
s11.2o	9.6	12.2	11.6	0.98	0.99	1.00	1.07	0.90	1.06	16.4	17.5	19.7
s11.2co	10.7	13.8	13.4	0.97	0.97	1.00	0.87	0.71	0.80	14.8	15.7	17.2
s25.0	11.9	14.4	14.1	0.98	0.99	1.01	1.58	1.48	1.54	30.0	34.2	34.8
s25.0c	12.3	15.2	15.2	0.98	0.98	1.00	1.86	1.64	1.78	36.8	39.8	43.3
s25.0o	12.9	15.9	15.0	0.99	0.98	1.01	0.62	0.63	0.58	12.8	16.0	13.9
s25.0co	12.6	15.8	15.6	0.98	0.97	1.00	1.01	0.94	0.96	20.4	23.7	24.0
s27.0	11.0	13.3	12.9	0.97	0.99	1.01	1.67	1.48	1.58	29.4	31.5	32.7
s27.0c	11.1	13.5	13.5	0.97	0.99	1.00	1.82	1.63	1.76	32.2	35.0	38.1
s27.0o	10.3	13.1	12.4	0.98	0.99	1.01	1.52	1.38	1.58	25.0	28.9	31.2
s27.0co	11.6	14.8	14.5	0.98	0.97	1.00	1.30	1.11	1.22	24.0	26.4	28.4
s40.0	11.2	13.5	13.2	0.98	0.99	1.01	1.82	1.66	1.76	32.5	35.9	37.3
s40.0c	12.1	15.0	15.1	0.98	0.98	1.00	1.49	1.29	1.39	28.9	31.1	33.6
s40.0o	11.9	15.0	14.3	0.98	0.97	1.00	0.79	0.77	0.77	15.1	18.6	17.6
s40.0co	11.9	15.2	14.9	0.98	0.97	1.00	1.32	1.16	1.26	25.2	28.2	30.2

Model	Shen											
	$\langle\varepsilon\rangle_{\nu_e}$	$\langle\varepsilon\rangle_{\bar{\nu}_e}$	$\langle\varepsilon\rangle_{\nu_x}$	p_{ν_e}	$p_{\bar{\nu}_e}$	p_{ν_x}	N_{ν_e}	$N_{\bar{\nu}_e}$	N_{ν_x}	E_{ν_e}	$E_{\bar{\nu}_e}$	E_{ν_x}
	[MeV]			[1]			[10^{57}]			[B]		
s11.2	9.4	11.2	10.9	0.96	0.99	1.00	1.17	1.00	1.05	17.6	18.0	18.3
s11.2c	9.5	11.4	11.1	0.96	0.98	1.00	1.11	0.98	1.00	16.9	17.8	17.8
s11.2o	8.6	11.1	10.3	0.97	0.99	1.00	1.12	0.94	1.17	15.4	16.7	19.2
s11.2co	8.9	11.4	10.8	0.97	0.98	1.00	1.04	0.91	1.07	14.9	16.7	18.5
s25.0	9.9	11.7	11.3	0.97	0.99	1.01	2.45	2.27	2.34	38.8	42.6	42.5
s25.0c	10.4	12.5	12.2	0.97	0.99	1.00	2.25	2.12	2.16	37.4	42.3	42.3
s25.0o	9.4	12.0	11.2	0.98	0.99	1.01	2.07	1.94	2.30	31.2	37.4	41.4
s25.0co	10.9	14.0	13.5	0.98	0.97	1.00	1.30	1.21	1.26	22.7	27.1	27.2
s27.0	9.8	11.6	11.2	0.97	0.99	1.00	1.89	1.70	1.76	29.5	31.6	31.5
s27.0c	10.0	11.9	11.7	0.97	0.99	1.00	1.80	1.66	1.68	28.7	31.7	31.5
s27.0o	9.9	12.7	11.9	0.98	0.98	1.00	1.22	1.12	1.24	19.2	22.7	23.6
s27.0co	10.5	13.6	13.0	0.97	0.97	1.00	1.07	0.97	1.01	18.0	21.0	21.2
s40.0	9.9	11.7	11.3	0.97	0.99	1.00	2.18	1.99	2.05	34.4	37.2	37.2
s40.0c	10.9	13.4	13.3	0.97	0.98	1.00	1.45	1.32	1.33	25.3	28.4	28.4
s40.0o	9.1	11.7	10.9	0.98	0.99	1.00	1.97	1.80	2.18	28.7	33.8	38.1
s40.0co	10.6	13.7	13.2	0.98	0.97	1.00	1.26	1.17	1.23	21.4	25.5	26.0

The larger radii and the correspondingly increased neutrino luminosity result also in an initially higher mass loss rate for the convective models, which then later also drop below the values of the standard cases. A slight influence of the opacity correction can also be seen, the lowered neutrino luminosities result in slightly decreased mass loss rates.

At the very end of the simulations, the reverse shock can even disappear again, for sufficiently progressed models, when the neutrino signal decays away and the wind velocities decrease.

The various models are much more diverse when looking at the – of course unobservable – centre of the cooling proto neutron star. These are presented in the panels of Figure 5.14 and 5.15, where we show central densities, temperatures, electron fraction, electron neutrino optical depth, entropy and the net electron neutrino per baryon fraction.

The increased electron neutrino cross sections with the opacity corrections is directly visible in the much higher central optical depths. Also visible is the greatly accelerated deleptonization in the centre when the mixing length scheme is applied, as soon as the convective cell hits the centre the net electron and electron neutrino fraction is very quickly brought down. Not only that, but the overall time to decrease Y_e and Y_{ν_e} is also much shorter.

Interestingly, the central densities are not always monotonically rising, the high temperatures during core-heating can even lead to a temporary expansion of material in the centre. This is especially prominent in the convective models.

Again it is also visible that not all models have entered the cooling phase yet, but are still in the initial phase of core-heating.

5.8 Neutrino driven wind

The material ejected by the neutrino driven wind will contribute to the nucleosynthetic yield of the supernova, at least if the explosion was successful to unbind the outer hull.

The parameters of interest are the mass loss rate $\dot{M}$, the material's electron fraction Y_e, and the entropy per baryon s, setting the neutron to seed nuclei ratio. The composition in the wind is mostly protons, neutrons, and α-particles. As the temperature drops, also heavy nuclei can form out of the α-particles, generating possible seeds for an r-process neutron flow.

Qian and Woosley (1996) give a simple analytical estimate using the neutrino luminosities and mean energies for the equilibrium Y_e value resulting from the neutrino irradiation of nucleons, which is – as mentioned in the introduction to this chapter – purely determined by the neutrinos. Later this was amended by an additional term accounting for the effect of the previously neglected neutrino opacity correction due to weak-magnetism by Horowitz and Li (1999). With a

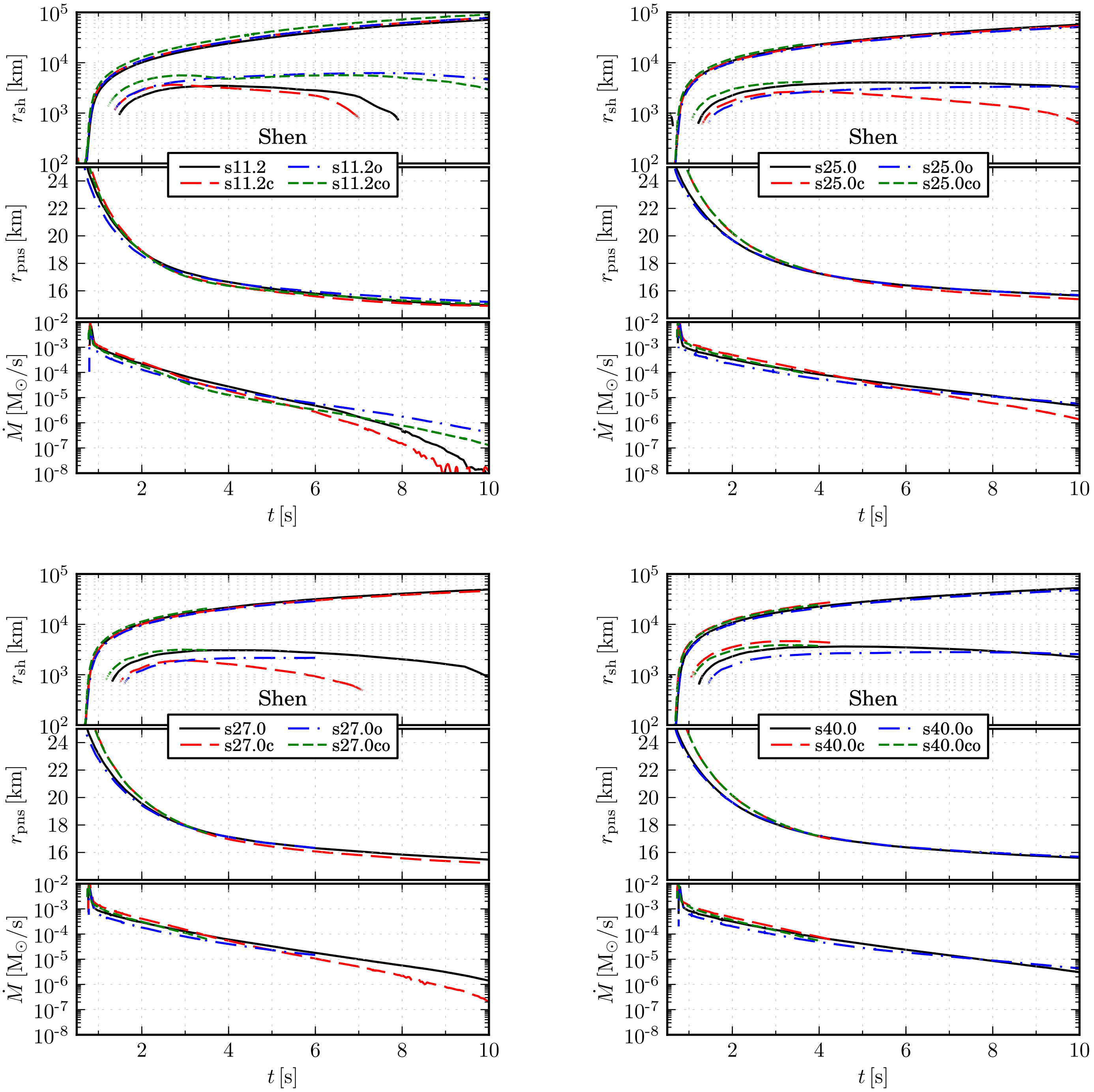

Figure 5.12: Evolution of the shock radii, both from the "explosion" as well as the transient reverse shock, (*upper*), the proto neutron star radius (*mid*) and mass loss rate (*lower* sub panels), for the Shen models.

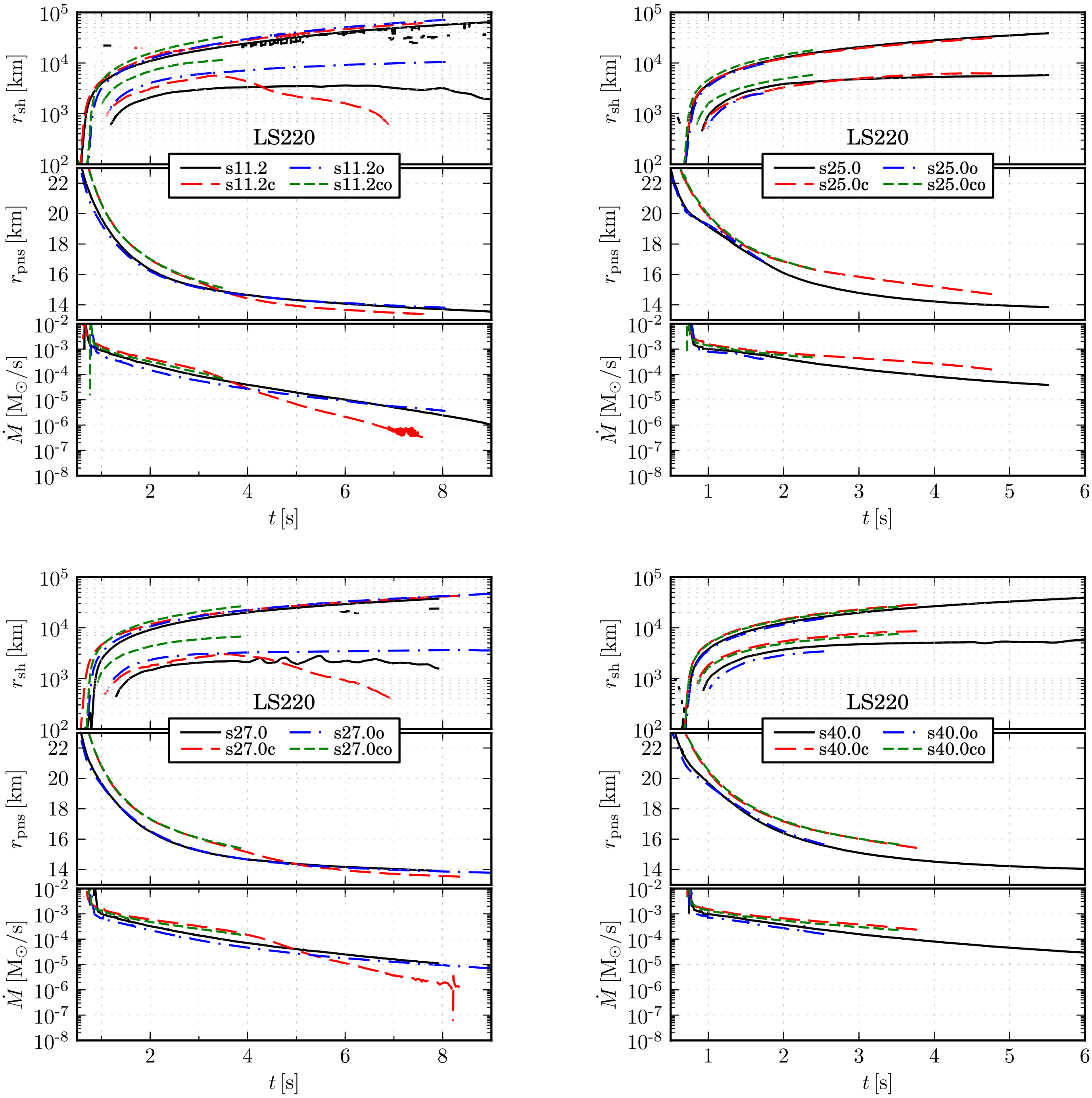

Figure 5.13: Analogous panels as in Figure 5.12 for the LS220 models. Note the different time ranges.

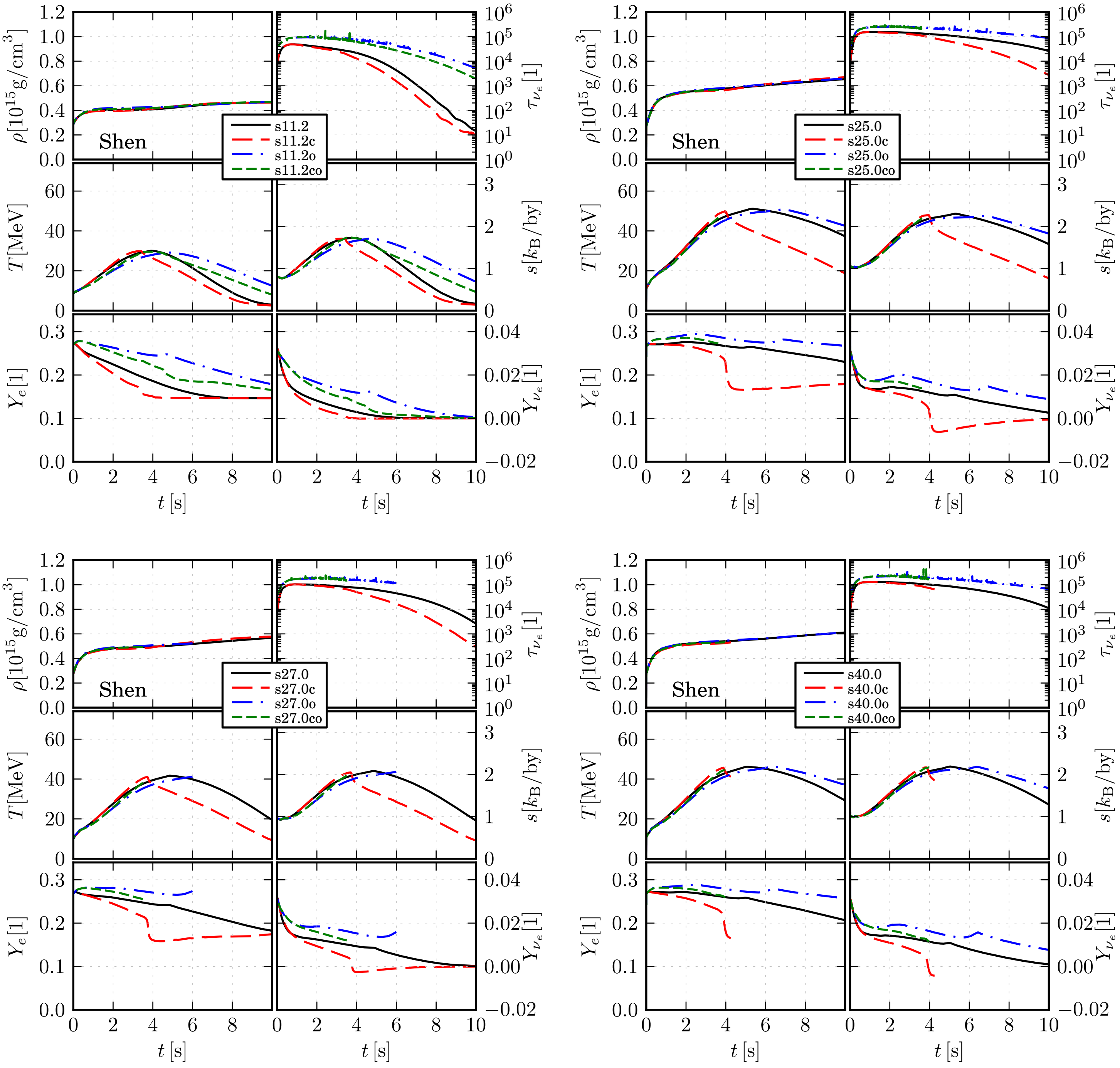

Figure 5.14: Time evolution of the central values of the material density ρ, temperature T, electron fraction Y_e, electron neutrino optical depth τ_{ν_e}, material entropy s, and net electron neutrino per baryon fraction Y_{ν_e}, for the Shen models.

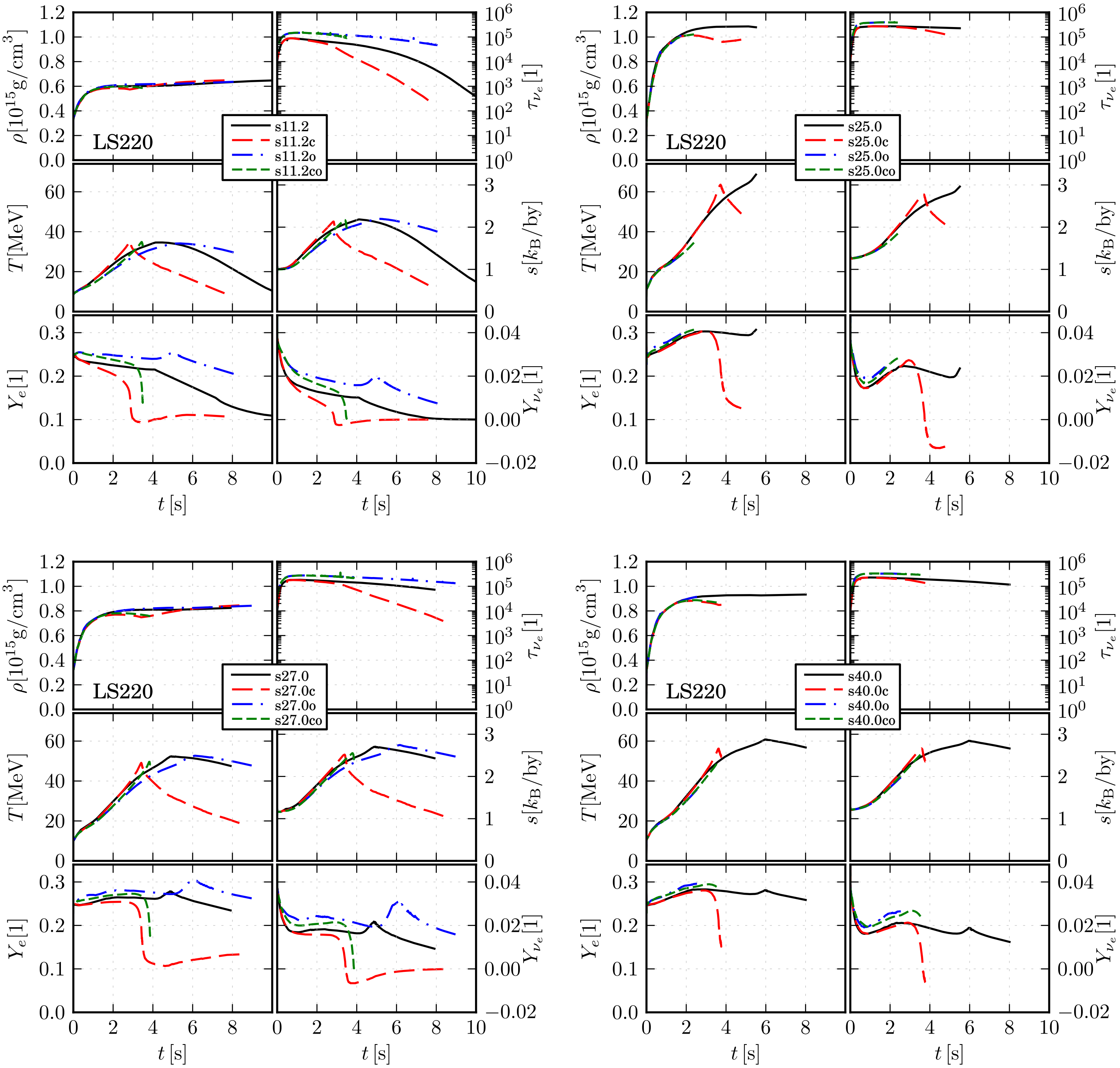

Figure 5.15: Analogous panels as in Figure 5.14 for the LS220 models.

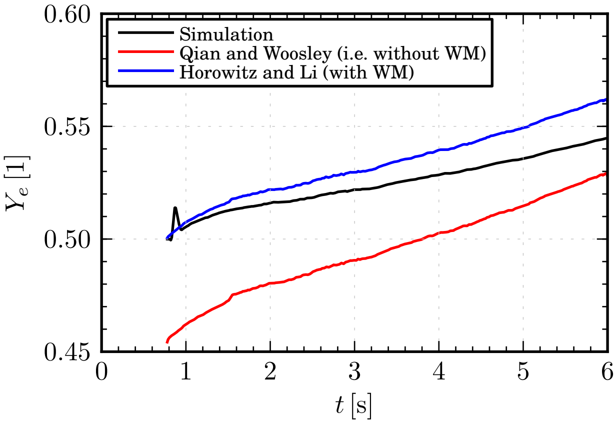

Figure 5.16: The electron fraction as found in the simulation shen-s27.0, and two reconstructions from the simulation's neutrino signal via Eq. (5.18), where the factor C was set to unity to not include the effect of weak magnetism (as given by Qian and Woosley, 1996), as well as the full Eq. 5.18 (Horowitz and Li, 1999)

custom spectrally weighted measure for the neutrino mean energies,

$$\hat{\varepsilon} = \frac{\langle \varepsilon^2 \rangle}{\langle \varepsilon \rangle}, \tag{5.17}$$

in our notation, the equilibrium Y_e value found is then found to be

$$Y_e \approx \left(1 + \frac{L_{\bar{\nu}_e} \hat{\varepsilon}_{\bar{\nu}_e}}{L_{\nu_e} \hat{\varepsilon}_{\nu_e}} Q(\hat{\varepsilon}_{\nu_e}, \hat{\varepsilon}_{\bar{\nu}_e}) C(\hat{\varepsilon}_{\nu_e}, \hat{\varepsilon}_{\bar{\nu}_e}) \right)^{-1}. \tag{5.18}$$

Here, the factors Q and C are due to the reactions' energy thresholds ("Q"-value) and due to the charge-conjugate ("C") violating weak magnetism, respectively, and are given by

$$Q(\hat{\varepsilon}_{\nu_e}, \hat{\varepsilon}_{\bar{\nu}_e}) = \frac{1 - 2\frac{\Delta}{\hat{\varepsilon}_{\bar{\nu}_e}} + 1.2\frac{\Delta}{\hat{\varepsilon}^2_{\bar{\nu}_e}}}{1 + 2\frac{\Delta}{\hat{\varepsilon}_{\nu_e}} + 1.2\frac{\Delta}{\hat{\varepsilon}^2_{\nu_e}}}, \tag{5.19}$$

$$C(\hat{\varepsilon}_{\nu_e}, \hat{\varepsilon}_{\bar{\nu}_e}) = \frac{1 - 8.66\frac{\hat{\varepsilon}_{\bar{\nu}_e}}{m_B c^2}}{1 + 1.22\frac{\hat{\varepsilon}_{\nu_e}}{m_B c^2}}. \tag{5.20}$$

We do not need these relations, as in our code the final composition is determined self-consistently when the material is ejected. However, for one it is used very much in diffusion codes which cannot accurately handle the low-density, free-streaming environment of the wind, e.g. in Roberts et al. (2012b). Secondly, it allows to selectively look at the influence of the weak-magnetism by setting C to 1 as a test. Not included in this simple picture is the so-called alpha-effect, first discussed by Fuller and Meyer (1995), which tends to drive Y_e more to 0.5 if included.

What happens there is that the free neutrons and protons tend to combine into α-particles, leaving only the remainder of the initial fractions, which is then either mostly neutrons if the initial abundances where neutron rich or protons otherwise. The α-particles have much lower neutrino cross sections than free nucleons and stay stable in the outflow, fixing that part of the ejecta to a composition with $Y_e = Z/A = 1/2$. Thus, the neutrinos can invariably only change some of the left-over nucleons into their corresponding counterpart, only driving the electron fraction even closer to 0.5.

In our code, this effect is partially included, due to our EoS setup with a low density NSE composition table used for temperatures above $0.5\,\mathrm{MeV/k_B}$. With this, the α-particle (and in principle also heavy nuclei) fraction is adjusted for the given Y_e value determined by the neutrinos on the current nucleon composition.

For the most accurate determination of Y_e, however, a full nuclear reaction network would have to be used in a post-processing step with the given outflow trajectories and neutrino signal, to also account for out-of-equilibrium burning reactions that cannot be modelled with our instantaneous NSE table composition.

As discussed in Section 5.4, the opacity correction is supposed to make a great influence on the resulting Y_e, in as much as Martínez-Pinedo et al. (2012) even find slightly neutron rich material with $Y_e \sim 0.45$ in the very early ejecta. However, it looks as if they neglect weak magnetism on their charged current neutrino nucleon opacities. In Figure 5.16 we present our self-consistently simulated Y_e, as well as a reconstruction via Eq. (5.18) with the full C-term and with $C = 1$.

As can be seen, the analytic approximation by Eq. (5.18) is in rather good agreement, especially in the early phase of interest here. If used with $C = 1$, which should emulate the effect of neglecting weak magnetism also in a self-consistent simulation, however, the material attains precisely the $Y_e \gtrsim 0.45$ as were found in Martínez-Pinedo et al. (2012).

We present the resulting self-consistent quantities relevant for the wind from our simulations in Figures 5.17 and 5.18. We find that all ejected material is always proton rich.

One has to be cautions, as these results do not yet rule out any possibility of an r-process in the supernova neutrino driven wind context. With the nucleon potentials included, the resulting electron fraction is to a much larger extent than in previous models also a function of the high density equation of state. For the two models we looked at in this study, the prospect to get an r-process scenario there does not seem good. But other high density equation of state models, possibly including more state-of-the art nuclear physics prescriptions, might yield a somewhat different picture. The relevant nuclear physics quantities, the symmetry energy J and its density derivative L, are still only very poorly constrained and could possibly allow a more drastic change of the neutrino spectra than the two models we looked at.

Still troubling are the comparatively low entropies, which only rise high values later when Y_e becomes increasingly large.

Another observation is that models with convection exhibit larger Y_e values than their counterparts. There, the initially enhanced deleptonization are results in the emission of much more electron neutrinos, the electron neutrino are increased much more than the anti-electron neutrino luminosities, while the respective mean energies are both increased by a very similar factor.

Another thing to consider is that collective neutrino flavor oscillations are expected to appear during the wind phase, which will alter the spectra of the different neutrino species in very complex ways, see e.g Duan et al. (2010) for a recent review. For a very detailed prediction of the resulting electron fraction it might be necessary to take these into account.

5.9 Summary

We artificially exploded four progenitors of the set simulated in Chapter 3, with two different high density equations of state, with and without a mixing-length scheme to approximate the multidimensional convection within the proto neutron star's core, and with and without a correction to our opacities regarding the nucleon potentials (see Section 3.4.6).

Some of these 32 models could be simulated to over 10s of neutrino mediated proto neutron star cooling, at which point they radiated away over 97% of their theoretical binding energy and lepton number.

We looked at the influence of the different high density equations of state, especially regarding the convection. In agreement with Roberts et al. (2012b), we could observe a visible imprint of the end of convection in the neutrino luminosities. This is directly a function of the poorly constrained nuclear physics parameter L, the density behaviour of the nuclear symmetry energy. We could augment their result with detailed predictions of also the neutrino mean energies, which they can only infer very approximately with their neutrino diffusion code.

The impact of the omission of the neutrino nucleon potentials in our opacities was expectedly found to be quite large, although the increased proto neutron star temperatures in the early phase were able to reduce that somewhat. As predicted by Roberts et al. (2012b); Martínez-Pinedo et al. (2012), due to the asymmetric nature of the correction to electron and anti-electron neutrinos, the new opacities resulted in a lowered electron fraction in the neutrino driven wind ejecta. Nevertheless, with the two high density equations of states we used we could never attain favourable conditions (i.e. $Y_e < 0.5$) for r-process nucleosynthesis. This is in contradiction to results found by Martínez-Pinedo et al. (2012), which also used the Shen equation of state and a probably similar proto neutron star. We thus believe it was their omission of weak-magnetism in the charged current neutrino-nucleon opacities that was responsible for their lower electron fractions.

Still, the electron fraction and the corresponding neutrino signal is with these corrections included also now a stronger function of the high density equation of state than previously found. Thus, the r-process in the neutrino driven wind could still be a viable scenario, given that high density nuclear physics can deliver favourable equations of state.

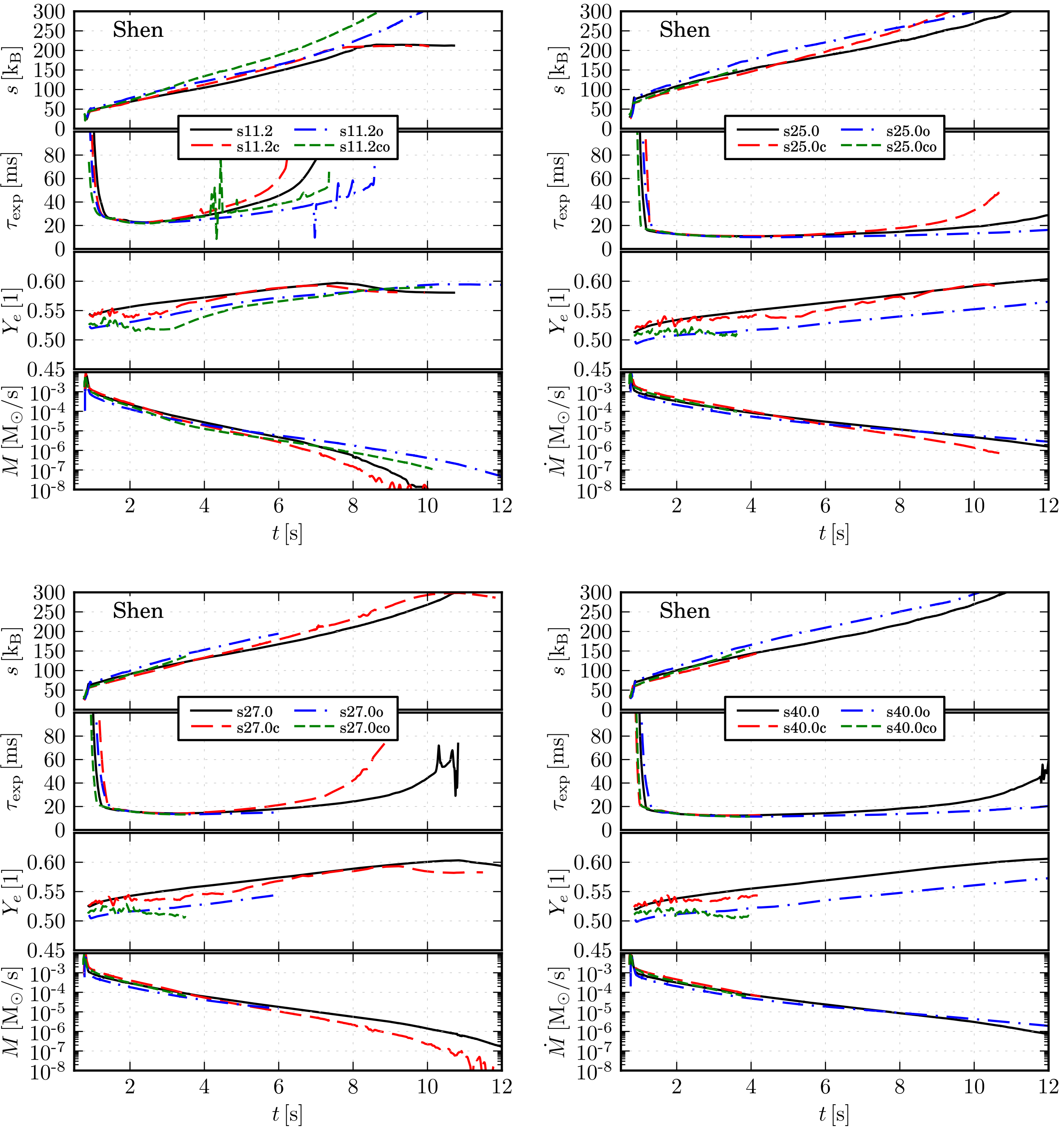

Figure 5.17: The key quantities for r-process conditions, from top to bottom sub-panel: The material entropy s (evaluated at 500km), the expansion time scale τ_{exp}, the electron fraction Y_e, and the mass loss rate $\dot{M}$ (both also from 500km). The ripples in the expansion time scale are due to transient waves propagating from the proto neutron star, which are for example excited by grid refinements.

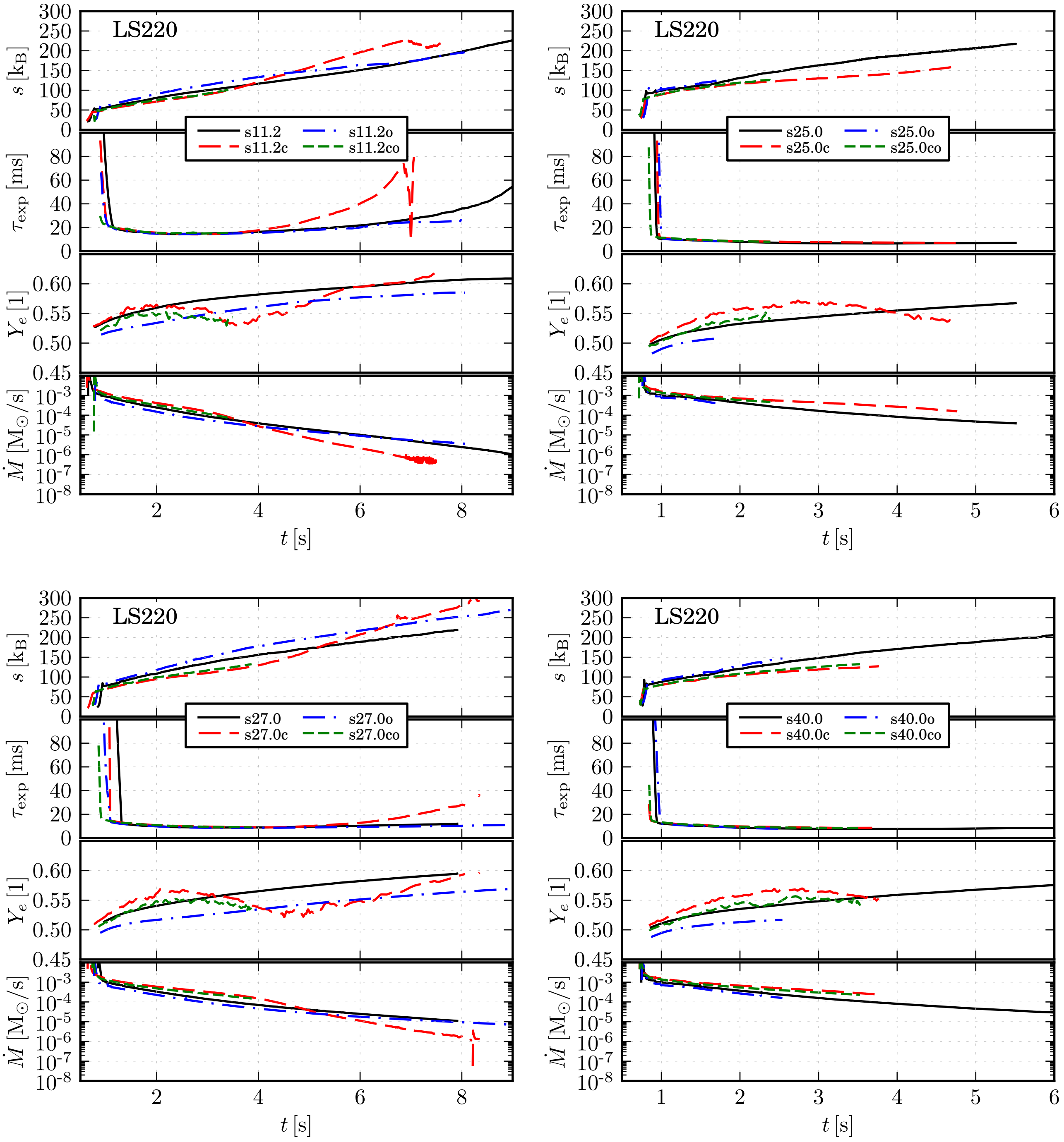

Figure 5.18: Analogous panels as in Figure 5.17 for the LS220 models, see the remarks there and note the different time ranges.

6 The Quenching of the Axial Coupling Constant in Neutron-star Matter

Lastly, we will present a small side project that was done in collaboration with Alexander Bartl and Achim Schwenk from the Technical University of Darmstadt, where we implemented a new method to treat the quenching of the axial coupling of neutron-star matter into our supernova code. To first order, the cross section for free neutrino-nucleon interactions with an initial neutrino energy of ε is

$$\frac{\mathrm{d}\sigma}{\mathrm{d}\Omega} = \frac{G_F^2 \varepsilon^2}{4\pi^2}\big(c_v^2(1+\cos\vartheta) + c_a^2(3-\cos\vartheta)\big), \tag{6.1}$$

where the c_v and c_a respectively are the vector and axial coupling constants for the specific process. Values for c_v and c_a can be found in Table 6.1. As can be seen, the cross section is dominated by the axial component. It turns out that the nucleons axial coupling constant is a function of the baryon density. It gets reduced, "quenched" as the density gets higher. Let us define the quenching factor as

$$q = \frac{g_A^*}{g_A}, \tag{6.2}$$

to relate the necessary high density axial coupling constant g_A^* to the vacuum value of $g_A \approx 1.26$.

Previously, we used a prescription according to Carter and Prakash (2002), who calculated the quenching factor to leading order and for symmetric, cold matter. They provided the supernovae community with a very simple analytic fit formula for the quenching factor as

$$q(\rho) = 1 - \frac{n_\mathrm{B}}{4.15(n_0 + n_\mathrm{B})}, \tag{6.3}$$

where $n_\mathrm{B} = \rho/m_\mathrm{B}$ is the current baryon density and $n_0 = 0.15\mathrm{fm}^{-3}$ is the equilibrium density of symmetric nuclear matter.

Menéndez et al. (2011) noted that second order corrections give a large additional contribution to the g_A quenching when they applied chiral effective field theory to Gamow-Teller transitions and neutrino less double beta decay processes. Building upon this, Alexander Bartl in his Diploma thesis extended the work of Menéndez et al. (2011) to account for finite temperature effects and asymmetric matter conditions as are found in proto neutron star matter.

He provided his result to us in the form of tables of the quenching factor as a function of density, electron fraction (i.e. neutron/proton asymmetry) of the

Table 6.1: Constants for neutrino cross sections, $g_a \approx 1.26$ is the nucleon axial coupling constant in a vacuum, θ_W is the weak mixing or Weinberg angle, with $\sin^2\theta_W \approx 0.231$.

Process	c_v	c_a
$\nu + p \to \nu + p$	$1/2 - 2\sin^2\theta_W$	$g_a/2$
$\nu + n \to \nu + n$	$-1/2$	$-g_a/2$
$\nu_e + n \to e^- + p$	1	g_a
$\bar{\nu}_e + n \to e^+ + n$	1	g_a

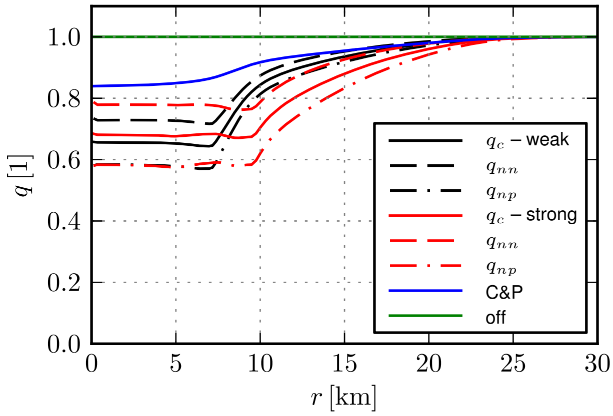

Figure 6.1: Values for the different models of the g_A quenching factor q, evaluated for profiles of the simulations at 250ms after core-bounce. For the two new cases ("weak", "strong") of the new treatment, there is also an additional isospin dependence resulting in different values for q depending on the type of reaction, nn and np for neutral current reactions on neutrons/protons and c for isospin changing reactions via charged currents.

matter, and material temperature, for two representative cases ("weak", "strong") of the parameter space of his model. As a slight technical complication for the simulations, the new quenching factors are now isospin dependent, and different for neutral current and charged current reactions. From Figure 6.1 we can see that the resulting new quenching factors are indeed quite different from the prescription of Eq. 6.3 and one could thus hope to see a direct imprint of this in the neutrino signal. Remarkable is also that even the weak case results in a stronger quenching than our previous treatment according to Carter and Prakash (2002).

However, the complex non-linear nature of the supernova (and also of supernova simulations) makes it difficult for any single $O(1)$ change of a parameter to result in a change of an observable in the same magnitude. So we ran a number of simulations in order to predict the change in the neutrino signal due to the different treatments of the quenching factor.

Table 6.2: Proto neutron star configuration at the end of the quenching simulations, as well as the total radiated Energy and Lepton numbers, also expressed in brackets as a fraction of the expected total value from ideal TOV solutions, see Chapter 5.

Model	r_{pns} [km]	M_{pns} [$\mathrm{M}_\odot$]	t_{end} [s]	E_ν [B] [1]	N_L [10^{56}] [1]
s15.0off	13.8	1.795	9.274	296 (0.88)	7.53 (0.90)
s15.0C&P	13.8	1.794	9.237	304 (0.91)	7.69 (0.92)
s15.0weak	14.2	1.794	5.721	276 (0.82)	7.18 (0.86)
s15.0strong	14.3	1.794	4.923	266 (0.79)	7.02 (0.84)

6.1 Results

In the same manner as was done in Chapter 3, we simulate the gravitational collapse and accretion phase for the first 500ms after core-bounce. The resulting neutrino signal and proto neutron star configuration can be found in the left panels of Figure 6.2.

Afterwards, continuing as was described in Chapter 5, an artificial explosion was launched by reducing the density of the infalling material, continuing the simulation into the proto neutron star cooling phase. Correspondingly, results can be found in the right panels of the same Figure.

Sadly, we can not say with good confidence that there is a discernible difference between any of the four simulations. We only see a very small difference in the resulting neutrino emission on a percent level.

Only when looking at the – of course unobservable – central values within the proto neutron star can one see some differences developing. There, the high densities necessary for the g_A quenching to appear are given and the different methods make themselves visible. One can speculate from this that measurable differences on the outside would present via a subtly different deleptonization and cooling time scale, and possibly also have an influence in the very late phase when the neutrinospheres penetrate higher and higher densities.

In Table 6.2 we show the progress of the simulations in form of the values of the proto neutron star and integrated neutrino emission at and up to the currently very last calculated time step. Additionally, in Table 6.3 we present the characteristics of the time integrated neutrino emission, here evaluated only up to 4.7 seconds, the minimum time attained by all of the simulations.

The expected hierarchy can be seen, models without quenching have a minimally lower energy and number flux, then comes our previous method according to Carter and Prakash (2002), followed by the weak and strong cases of the new treatment. Still, the differences of the new method to our previously used scheme by Carter and Prakash (2002) are only on the level of a few percent.

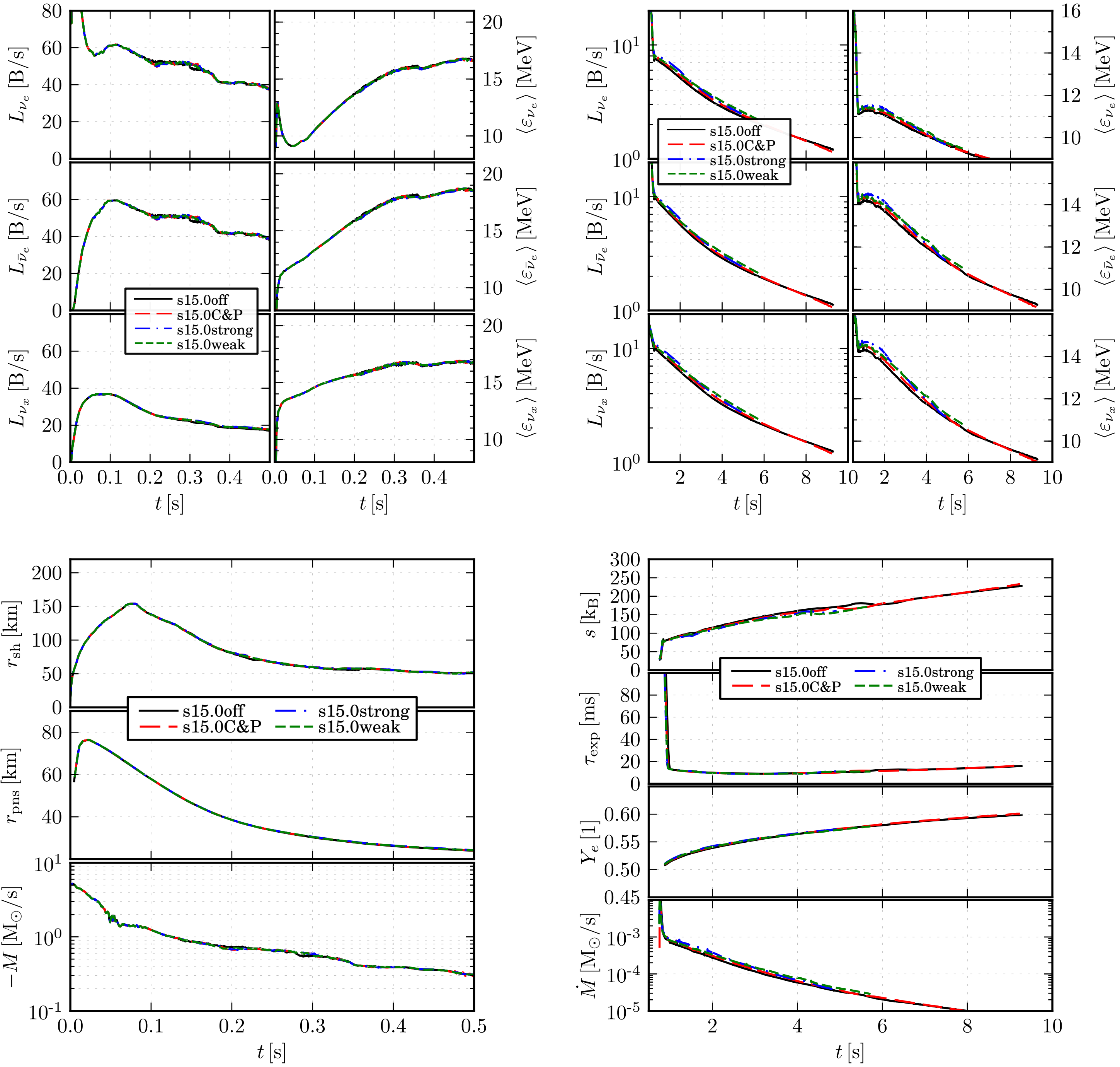

Figure 6.2: The upper panels show the neutrino signal, in the *upper left* panel for the accretion phase, the first 500ms, and in the *upper right* panel for the subsequent proto neutron star cooling evolution. The lower panels show the hydrodynamical evolution, again in the *lower left* panel for the first 500ms and in the *lower right* panel for the cooling phase.

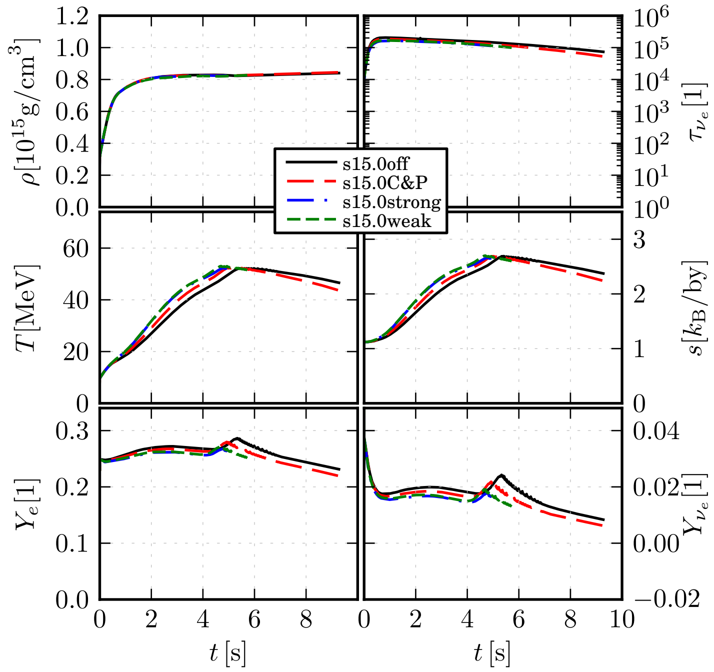

Figure 6.3: Central hydrodynamical values, material density ρ, temperature T, electron fraction Y_e, electron neutrino optical depth τ_{ν_e}, entropy per baryon s and net electron neutrino per baryon fraction Y_{ν_e}.

Table 6.3: Time integrated spectral parameters for the g_A quenching simulations, up to the common first 4.7 seconds of evolution. Listed are mean energies $\langle\varepsilon\rangle$, pinching parameter p, total number N and total energy E for each neutrino type. The pinching parameter was inferred according to the procedure described in Section 3.5. Note that N_{ν_x} and E_{ν_x} are for only one of the four heavy lepton neutrino kinds, i.e. the total emitted energy is $E_{\nu_e} + E_{\bar{\nu}_e} + 4E_{\nu_x}$.

Model	$\langle\varepsilon\rangle_{\nu_e}$	$\langle\varepsilon\rangle_{\bar{\nu}_e}$	$\langle\varepsilon\rangle_{\nu_x}$	p_{ν_e}	$p_{\bar{\nu}_e}$	p_{ν_x}	N_{ν_e}	$N_{\bar{\nu}_e}$	N_{ν_x}	E_{ν_e}	$E_{\bar{\nu}_e}$	E_{ν_x}
	[MeV]			[1]			[10^{57}]			[B]		
s15.0off	12.0	14.8	14.1	0.95	0.96	1.00	2.69	2.02	1.63	51.8	47.8	36.8
s15.0C&P	12.0	14.8	14.2	0.95	0.96	1.00	2.74	2.06	1.69	52.8	48.7	38.3
s15.0weak	12.0	14.8	14.2	0.95	0.96	1.00	2.77	2.08	1.72	53.5	49.5	39.1
s15.0strong	12.0	14.9	14.3	0.95	0.96	0.99	2.79	2.10	1.73	53.9	49.9	39.7

6.2 Summary

The elaborate g_A quenching treatment turned out to be unimportant, especially for the early phase relevant for the supernovae explosion, and for proto neutron star calculations at least up to the point we were able to simulate. Differences might appear in the late phase of the cooling signal.

On the bright side, these results prove that our setup and numerical scheme are stable and not influenced in a chaotic way by small changes in (at least these) input parameters.

This is especially striking due to the fact that the radial grid of our Eulerian code had to be adapted to the contracting proto neutron star more than ten times for each simulation. This was done independently each time and with grids adapted to the current profiles found at the moment the refinement became necessary. The lack of a big difference in the simulation outcomes is therefore very reassuring that these numerical issues do not seem to make any impact on the resulting neutrino signal.

7 Conclusion

In this thesis we studied the neutrino signal of core-collapse events and their newly formed proto neutron stars with detailed radiation-hydrodynamical simulations. In the first part, as a study of the pre-explosion neutrino signal, a large number of progenitor models for three different high density equations of state were evolved through gravitational collapse, the formation of a proto neutron star and a subsequent phase of half a second of accretion.

We could confirm that the neutrino signal of the first 100ms has a very generic shape. A possible observation of that phase with existing or future neutrino detectors could thus help in determining the neutrino mass hierarchy, as was already laid out in the work by Serpico et al. (2012) in which a number of models simulated for this thesis were used.

In contrast to claims made by O'Connor and Ott (2013), we do not find a very clear signature of the high density equation of state in the neutrino signal, which seems to disappear when sufficiently sophisticated neutrino opacities are taken into account. These include neutrino nucleon interactions allowing for energy exchange reactions by nucleon-recoil and neutrino-neutrino pair interactions.

For the first time, also the genuinely multidimensional effect of convection within the proto neutron star's core could also be approximated in spherically symmetric simulations with a detailed neutrino transport, by borrowing a scheme from stellar evolution. This so-called mixing length theory introduces artificial energy and composition fluxes that attempt to mimic the efficient mixing of matter by the multidimensional flows that would develop in reality. While truly multidimensional simulations with sufficiently advanced neutrino physics are indeed possible and used nowadays, they are computationally very costly, require large supercomputers and are therefore only able to simulate the early phase in a tolerable time span.[1] Sadly, simulating the tens of seconds of proto neutron star cooling in full dimensionality is inconceivable, today.

One therefore has to resort to an approximative modelling of the important and genuinely multidimensional effect of convection. We could confirm that our scheme results in a neutrino signal that is in much better agreement with true multidimensional simulations of the early phase. During this early, accretion dominated phase, its influence is to zeroth order a larger neutron star, correspondingly

---

[1] Even the spherically symmetric simulations done for this thesis require an appreciable amount of computation. We estimate that a single cooling simulation for about 10s requires $\mathcal{O}(10^{15})$ double-precision floating point operations. Even though parallelism was exploited as much as feasible in an individual calculation step, one cannot parallelise over the time domain itself. This results in run times of several months at least.

enlarged neutrino luminosities and somewhat lowered mean neutrino energies.

An omission in the neutrino opacities formulated by Burrows and Sawyer (1999) that is used by our simulation code was recently addressed by Martínez-Pinedo et al. (2012). There, the energy shift arising from the difference in neutron and proton background interaction potential in the high density regime within the proto neutron star was neglected for the neutrino nucleon cross sections. As expected already by Martínez-Pinedo et al. (2012), we found that this omission is not crucial during the accretion phase.

In the subsequent chapter, we continued this accretion phase for an even longer time, in order to follow core-collapse events that fail to produce a viable explosion up to the point where the neutron star must form a black hole. We could demonstrate that our simulations are in rather good agreement with published models in full general relativity – even though we only make use of a pseudo-Newtonian code that models the most important general relativistic effects by a modified, TOV-like gravitational potential (Marek et al., 2006).

Previously published results with a comparably accurate neutrino transfer scheme (e.g. Fischer et al., 2009; Sumiyoshi et al., 2008) found very high (rms-) mean neutrino energies, especially close to the moment of black hole formation. These studies, however, did not take energy exchanging nucleon-recoil into account for the neutrino-nucleon cross sections, neglected the reduction of the neutrino-cross sections by nucleon correlations at high densities, and only in some cases were neutrino-neutrino pair interactions included.

When we do take these effects into account, we find much lower neutrino energies, which sadly make the prospect of detecting such a black hole formation event (Yang and Lunardini, 2011) much more unlikely.

If an event could be detected, however, our predictions for the neutrino signal at the very end of the simulations might be helpful for the idea put forth by Beacom et al. (2001): they suggested to use the expected fast cut-off in the neutrino signal due to the formation of an event horizon to constrain the absolute neutrino masses by time-of-flight measurements. Our prediction of the neutrino signal at the moment of cut-off might be valuable there.

As a genuine improvement over existing work in the literature, we also included the mixing length scheme in these models and investigated the influence the convection within the proto neutron stars core on the black hole formation neutrino signal.

In the final of the main chapters, we artificially exploded a set of models in order to study the proto neutron star cooling phase that will occur after a potential explosion and followed that phase in some cases for more than 10s and until they had lost more than 97% of their energy and lepton number. It was already known that convection in proto neutron star cooling is of great importance, but as we said, truly multidimensional models are computationally out of reach for the foreseeable future. With our mixing length scheme we were able to simulate this phase hydrodynamically, including our very elaborate neutrino transfer treatment. Previous studies such as most recently done by Roberts et al. (2012b) used a diffusion code and could thus not accurately predict the detailed spectral shape of the resulting neutrino signal. We could confirm their prediction that the end of convection after several seconds is marked by a change in neutrino luminosities and could augment this with detailed spectral data that also exhibit a signature of that phenomenon.

For the cooling phase, the influence of the omission of the nucleon potentials is significant, in contrast to the previous topics. The corrected opacities lead to somewhat lowered luminosities and thus a correspondingly longer cooling time scale, and affect electron and anti-electron neutrinos very differently, due to their asymmetric reaction with either neutrons or protons. Not only that, the inclusion of these potentials opens up a new window into the very unconstrained high density physics, as the resulting neutrino signal is now to a much larger extent than previously thought also a function of the equation of state of neutron star matter.

In Martínez-Pinedo et al. (2012) it was even found that the corrected neutrino spectra and luminosities where changed by a large enough amount to eject even slightly neutron rich matter with $Y_e \gtrsim 0.45$ in the very early phase. This would open up the potential again for r-process nucleosynthesis of heavy elements in the neutrino driven wind of cooling proto neutron stars.

However, in none of our simulation can we find $Y_e < 0.5$, even though we also look at similar proto neutron stars and the same high density equation of state. We believe that most probably the omission in the work of Martínez-Pinedo et al. (2012) of weak magnetism in charged current neutrino-nucleon absorption reactions is responsible for this (to a smaller degree it could also be relevant that our neutron stars might have a bit higher temperatures in the mantle after the slightly longer accretion phase).

Moreover, the inclusion of convection with its increased deleptonization and energy loss also results in a boost of the electron neutrino emission, bringing Y_e somewhat up additionally. For r-process nucleosynthesis, though, a neutron rich outflow with $Y_e < 0.5$ is a necessary ingredient.

Nevertheless, with the mentioned increased influence of high density physics also on the neutrino signal, neutron rich outflows might still be found for other neutron star equations of state. This recent development is quite exciting in that it might open up new ways to get at the properties of hot, high density neutron star matter.

A Lorentz Transformations

The equations and output quantities of the simulation code Vertex are formulated in the locally co-moving frame of the fluid. Thus, transformation rules for the relevant quantities, cell-integrated values of moments of the radiation field, are necessary. The calculations are straightforward and for reference purposes only.

A.1 Energy Integrated Moments

A certain frequency integrated moment is defined in some reference frame as an energy ($\tilde{\varepsilon}$) and angle ($\tilde{\mu}$) integral over the particle distribution function in this frame, $\tilde{f}(\tilde{\varepsilon}, \tilde{\mu})$,

$$\tilde{M}_{ij} = \int_0^\infty d\tilde{\varepsilon} \int_{-1}^1 d\tilde{\mu}\, \tilde{\varepsilon}^i \tilde{\mu}^j\, \tilde{f}(\tilde{\varepsilon}, \tilde{\mu}). \tag{A.1}$$

The Lorentz transformation for $(\tilde{\varepsilon}, \tilde{\mu})$ to the corresponding variables in another frame (ε, μ), with relative velocity β, Lorentz factor $\gamma = (1 - \beta^2)^{-1/2}$, are

$$\tilde{\varepsilon} = \gamma\varepsilon(1 + \beta\mu), \tag{A.2}$$

$$\tilde{\mu} = \frac{\mu + \beta}{1 + \beta\mu}. \tag{A.3}$$

and the distribution function is a Lorentz invariant quantity, that is the two distributions are related simply by

$$\tilde{f}(\tilde{\varepsilon}, \tilde{\mu}) = f(\varepsilon, \mu). \tag{A.4}$$

Let us now rewrite Eq. (A.1) in the transformed variables and see if we can express it in terms of moments in the other frame. Insertion yields

$$\tilde{M}_{ij} = \int_0^\infty d\varepsilon \int_{-1}^1 d\mu \left| \det \frac{\partial(\tilde{\varepsilon}, \tilde{\mu})}{\partial(\varepsilon, \mu)} \right| (\gamma\varepsilon(1 + \beta\mu))^i \left(\frac{\mu + \beta}{1 + \beta\mu} \right)^j f(\varepsilon, \mu). \tag{A.5}$$

The necessary Jacobian determinant is given by

$$\det \frac{\partial(\tilde{\varepsilon}, \tilde{\mu})}{\partial(\varepsilon, \mu)} = \frac{1}{\gamma(1 + \beta\mu)}, \tag{A.6}$$

resulting in

$$\tilde{M}_{ij} = \gamma^{i-1} \int_0^\infty d\varepsilon \int_{-1}^1 d\mu \left(1 + \beta\mu \right)^{i-j-1} \left(1 + \frac{\beta}{\mu} \right)^j \varepsilon^i \mu^j\, f(\varepsilon, \mu), \tag{A.7}$$

which can be expressed as a sum of moments by expanding the integration kernel,

$$k_{ij}(\mu,\beta) = \Bigl(1+\beta\mu\Bigr)^{i-j-1}\Bigl(1+\frac{\beta}{\mu}\Bigr)^{j}. \tag{A.8}$$

Setting $\beta\mu = x$ and $\beta/\mu = y$ and with

$$(1+x)^N(1+y)^M = \sum_{n,m}^{\infty}\binom{N}{n}\binom{M}{m}x^n y^m, \tag{A.9}$$

where for $|x| < 1$, the expression holds also for negative (real even) N, M if the generalized binomial coefficient

$$\binom{N}{n} := \frac{N(N-1)\dots(N-n+1)}{n!} \tag{A.10}$$

is used, it follows that

$$k_{ij}(\mu,\beta) = \sum_{n=0}\sum_{m=0}\binom{i-j-1}{n}\binom{j}{m}\beta^{n+m}\mu^{n-m}. \tag{A.11}$$

Note that for $i-j-1=0$ the n-sum collapses to

$$k_{j+1,j}(\mu,\beta) = \sum_{m=0}\binom{j}{m}\beta^m\mu^{-m}, \tag{A.12}$$

and the m-sum likewise for $j=0$ to

$$k_{i,0}(\mu,\beta) = \sum_{n=0}\binom{i-1}{n}\beta^n\mu^n, \tag{A.13}$$

Note that Eq. (A.11)-(A.13) are finite sums except when $i-j-1<0$ or $j<0$. Integration yields the transformation rules for a general moment $\tilde{M}_{ij}$ expressed in moments of another frame,

$$\begin{aligned}\tilde{M}_{ij} = \gamma^{i-1}\int_0^\infty d\varepsilon \int_{-1}^{1} d\mu\, k_{ij}(\mu,\beta)\varepsilon^i\mu^j\, f(\varepsilon,\mu)\\ = \gamma^{i-1}\sum_{n=0}\sum_{m=0}\binom{i-j-1}{n}\binom{j}{m}\beta^{n+m}M_{i,\,j+n-m}.\end{aligned} \tag{A.14}$$

again, collapsing for $i-j-1=0$ to

$$\tilde{M}_{j+1,\,j}(\mu,\beta) = \gamma^j\sum_{m=0}\binom{j}{m}\beta^m M_{i,\,j-m}, \tag{A.15}$$

and for $j=0$ to

$$M_{i,0}(\mu,\beta) = \gamma^{i-1}\sum_{n=0}\binom{i-1}{n}\beta^n M_{i,\,j+n}. \tag{A.16}$$

In $\mathcal{O}(\beta)$ this simplifies considerably, as $\gamma^{i-1}\beta^{n+m} \simeq \beta^{n+m} + \mathcal{O}(\beta^{n+m+2})$ only terms with $n + m \leq 1$ survive,

$$\tilde{M}_{ij} = M_{ij} + j\beta M_{i,\,j-1} + (i - j - 1)\beta M_{i,\,j+1} + \mathcal{O}(\beta^2). \tag{A.17}$$

Using,

$$J = M_{03}, \qquad \mathcal{J} = M_{02}, \tag{A.18}$$
$$H = M_{13}, \qquad \mathcal{H} = M_{12}, \tag{A.19}$$
$$K = M_{23}, \qquad \mathcal{K} = M_{22}, \tag{A.20}$$

we recover the explicit transformation of these first few commonly used moments as

$$\tilde{J} = \gamma^2(J + 2\beta H + \beta^2 K) \qquad \simeq J + 2\beta H, \tag{A.21}$$
$$\tilde{H} = \gamma^2((1 + \beta^2)H + \beta(J + K)) \qquad \simeq H + \beta(J + K), \tag{A.22}$$
$$\tilde{K} = \gamma^2(K + 2\beta H + \beta^2 J) \qquad \simeq K + 2\beta H, \tag{A.23}$$
$$\tilde{\mathcal{J}} = \gamma(\mathcal{J} + \beta\mathcal{H}) \qquad \simeq \mathcal{J} + \beta\mathcal{H}, \tag{A.24}$$
$$\tilde{\mathcal{H}} = \gamma(\mathcal{H} + \beta\mathcal{J}) \qquad \simeq \mathcal{H} + \beta\mathcal{J}, \tag{A.25}$$

where the approximate expressions are correct to $\mathcal{O}(\beta)$. Only the case for $\tilde{\mathcal{K}}$ is a bit more troublesome due to the fact that it has the rational function

$$k_{22}(\mu, \beta)\mu^2 = \frac{(\mu + \beta)^2}{1 + \beta\mu} \tag{A.26}$$

as a kernel, and therefore its series representation for the exact transformation does not terminate, instead it is

$$\begin{aligned} \tilde{\mathcal{K}} &= \gamma \sum_{n=0}^{\infty} \sum_{m=0}^{2} (-1)^n \binom{2}{m} \beta^{n+m} M_{2+n-m,2} \\ &\simeq \mathcal{K} + \beta(2\mathcal{H} - M_{32}) \end{aligned} \tag{A.27}$$

A.2 Energy Binned Quantities

The situation is considerably more complex if we want to transform the energy dependent (spectral) quantities, in our finite volume code these are represented as integrals over a particular range of neutrino energy,

$$\tilde{B}_{tij} = \int_{\tilde{\varepsilon}_t}^{\tilde{\varepsilon}_{t+1}} d\tilde{\varepsilon} \int_{-1}^{1} d\tilde{\mu}\, \tilde{\varepsilon}^i \tilde{\mu}^j\, \tilde{f}(\tilde{\varepsilon}, \tilde{\mu}). \tag{A.28}$$

From these, the frequency integrated moments are then recovered by summation, as

$$\tilde{M}_{ij} = \sum_t B_{tij}. \tag{A.29}$$

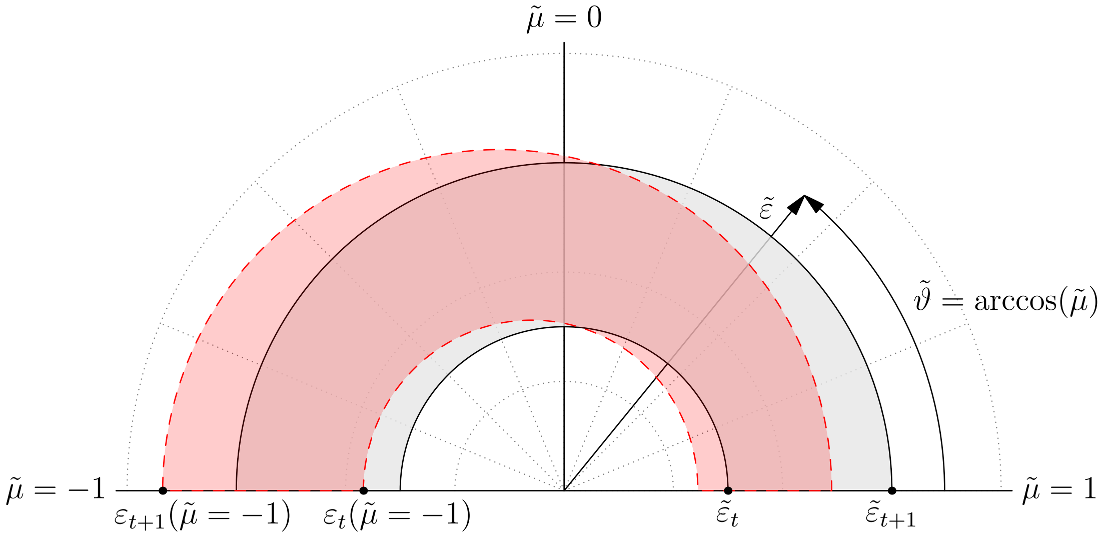

Figure A.1: The boosted shape of an energy bin, shown in polar coordinates with $\cos(\tilde{\vartheta}) = \tilde{\mu}$, the forward direction is right. The grey area is what the current frame takes as the integration domain for $\tilde{B}_{tij}$, while the red shape is the integration domain used in B_{tij}'s frame, travelling with $\beta = 0.2$ relative to the other.

Now, the Lorentz transformation also changes the domain of integration, expressing the bin B_{tij} in the boosted variables results in

$$\tilde{B}_{tij} = \gamma^{j-1} \int_{-1}^{1} d\mu \int_{\gamma(1+\beta\mu)\varepsilon_t}^{\gamma(1+\beta\mu)\varepsilon_{t+1}} d\varepsilon \, K_{ij}(\mu, \beta) f(\varepsilon, \mu). \tag{A.30}$$

where the shape of the regular domain of integration in $\tilde{B}$'s frame appears distorted in the other frame, confer to Figure A.1 for a visualization. Let us define a shape function

$$\chi_t(\mu, \beta, \varepsilon) = \begin{cases} 1 & \text{if } \gamma(1+\beta\mu)\varepsilon_t < \varepsilon < \gamma(1+\beta\mu)\varepsilon_{t+1}, \\ 0 & \text{else.} \end{cases} \tag{A.31}$$

such that

$$\tilde{B}_{tij} = \gamma^{i-1} \int_{-1}^{1} d\mu \int_{0}^{\infty} d\varepsilon \, \chi_t(\mu, \beta, \varepsilon) K_{ij}(\mu, \beta) f(\varepsilon, \mu). \tag{A.32}$$

and use it to split-up the integral in the same domains $D_u = [-1, 1] \times [\varepsilon_u, \varepsilon_{u+1}]$ we use for the bins in our frame of reference,

$$\tilde{B}_{tij} = \gamma^{i-1} \sum_u \int_{D_u} \mathrm{d}\mu \mathrm{d}\varepsilon \, \chi_t(\mu, \beta, \varepsilon) K_{ij}(\mu, \beta) f(\varepsilon, \mu) \tag{A.33}$$

It will be futile to try to expand the discontinuous χ_t in the kernel in a power series. However, $f(\varepsilon, \mu)$ is assumed to be and k_{ij} actually is a smooth function on $D_u \backslash \partial D_u$. A power series approximation is thus justified. Taking $\{H_p^u(\varepsilon, \mu) : p \in \mathbb{N}\}$ as a suitable set of orthogonal polynomials on each of the domains D_u, there should be coefficients f^u_{ijp} such that for $(\varepsilon, \mu) \in D_u$,

$$K_{ij}(\mu, \beta) f(\varepsilon, \mu) = \sum_{p=0} f^u_{ijp} H^u_p(\varepsilon, \mu) \tag{A.34}$$

and where we can get at these coefficients by projection,

$$f^u_{ijp} = \iint_{D_u} d\varepsilon d\mu \, K_{ij}(\mu, \beta) f(\varepsilon, \mu) H^u_p(\varepsilon, \mu). \tag{A.35}$$

Using the explicit polynomial form of the H^u_p itself,

$$H^u_p(\varepsilon, \mu) = \sum_{q,r} h^u_{pqr} \varepsilon^q \mu^r, \tag{A.36}$$

we can recover an explicit series for the coefficients after inserting our own moment expansion from which we started. It follows immediately that

$$f^u_{ijp} = \sum_{n,m,q,r} \binom{i-j-1}{n} \binom{j}{m} \beta^{n+m} h^u_{pqr} \tilde{B}_{t,q,r+n-m}. \tag{A.37}$$

Inserting this into Eq. (A.33),

$$\tilde{B}_{tij} = \gamma^{i-1} \sum_{u,p} f^u_{ijp} \iint_{D_u} d\varepsilon d\mu \, \chi_t(\mu, \beta, \varepsilon) H^u_p(\varepsilon, \mu) \tag{A.38}$$

Therefore, given the overlap integral of χ_t over H^u_n,

$$\chi^u_{tp}(\beta) = \iint_{D_u} d\varepsilon d\mu \, \chi_t(1, \beta, \varepsilon) H^u_p(\varepsilon, \mu) \tag{A.39}$$

we finally end up with

$$\tilde{B}_{tij} = \gamma^{i-1} \sum_{u,p,n,m,q,r} \binom{i-j-1}{n} \binom{j}{m} \chi^u_{tp}(\beta) h^u_{pqr} \beta^{n+m} \tilde{B}_{t,q,r+n-m}. \tag{A.40}$$

In practice, one avoids transformations of spectral quantities wherever possible due to this complexity, and we will not try to put this formal result into an explicit one.

B Thermodynamic derivatives for the Ledoux criterion

Stability against small radial perturbations of a hydrostatic configuration is given when Ledoux's criterion is met,

$$C_{\mathrm{led}} = \left(\frac{\partial\rho}{\partial s}\right)_{Y_e,p} \frac{\mathrm{d}s}{\mathrm{d}r} + \left(\frac{\partial\rho}{\partial Y_e}\right)_{s,p} \frac{\mathrm{d}Y_e}{\mathrm{d}r} \geq 0. \tag{B.1}$$

For this, we need the thermodynamic derivatives $(\partial\rho/\partial s)_{Y_e,p}$ and $(\partial\rho/\partial Y_e)_{s,p}$. Supernova equation of state tables (or routines) are usually provided as functions of ρ, T, and Y_e. We need to convert these derivatives into derivatives of ρ, T, and Y_e.

B.1 First derivative

Luckily, one of the constraints of the derivative, $dY_e = 0$, is expressed in the natural variables already, therefore throughout this section $dY_e = 0$ is implicitly assumed (e.g. when taking total derivatives). It is convenient to look at the inverse of the first derivative, $(\partial s/\partial\rho)_{Y,p}$. Regardless of the choice of variables (ρ, Y_e, p) or (ρ, T, Y_e), ds must be the same, therefore it must be that

$$ds = \left(\frac{\partial s}{\partial\rho}\right)_{Y_e,p} d\rho = \left(\frac{\partial s}{\partial\rho}\right)_{T,Y_e} d\rho + \left(\frac{\partial s}{\partial T}\right)_{\rho,Y_e} dT \tag{B.2}$$

using $dY_e = 0$. Taking $d/d\rho$ we end up with

$$\left(\frac{\partial s}{\partial\rho}\right)_{Y_e,p} = \left(\frac{\partial s}{\partial\rho}\right)_{T,Y_e} + \left(\frac{\partial s}{\partial T}\right)_{\rho,Y_e} \left(\frac{\partial T}{\partial\rho}\right)_{Y_e,p} \tag{B.3}$$

Still missing is $(\partial T/\partial\rho)_{Y_e,p}$, which however is already in the natural variables we want and therefore easily obtainable when looking at

$$dp = 0 = \left(\frac{\partial p}{\partial\rho}\right)_{T,Y_e} d\rho + \left(\frac{\partial p}{\partial T}\right)_{\rho,Y_e} dT \tag{B.4}$$

$$0 = \left(\frac{\partial p}{\partial\rho}\right)_{T,Y_e} + \left(\frac{\partial p}{\partial T}\right)_{\rho,Y_e} \left(\frac{\partial T}{\partial\rho}\right)_{Y_e,p} \tag{B.5}$$

So we find

$$\left(\frac{\partial s}{\partial\rho}\right)_{Y_e,p} = \left(\frac{\partial s}{\partial\rho}\right)_{T,Y_e} - \left(\frac{\partial s}{\partial T}\right)_{\rho,Y_e} \frac{\left(\frac{\partial p}{\partial\rho}\right)_{T,Y_e}}{\left(\frac{\partial p}{\partial T}\right)_{\rho,Y_e}} \tag{B.6}$$

B.2 Second derivative

The second derivative is more painful, as neither s nor p are natural variables of the equation of state, while still $ds = 0$ and $dp = 0$ has to be obeyed simultaneously. Thus

$$\begin{aligned} ds &= \left(\frac{\partial s}{\partial \rho}\right)_{T,Y_e} d\rho + \left(\frac{\partial s}{\partial T}\right)_{\rho,Y_e} dT + \left(\frac{\partial s}{\partial Y_e}\right)_{\rho,Y_e} dY_e &&= 0, && \text{(B.7)} \\ dp &= \left(\frac{\partial p}{\partial \rho}\right)_{T,Y_e} d\rho + \left(\frac{\partial p}{\partial T}\right)_{\rho,Y_e} dT + \left(\frac{\partial p}{\partial Y_e}\right)_{\rho,Y_e} dY_e &&= 0, && \text{(B.8)} \end{aligned}$$

Solving equations (B.7) and (B.8) for dT gives

$$\begin{aligned} &\frac{1}{\left(\frac{\partial s}{\partial T}\right)}\left(\left(\frac{\partial s}{\partial \rho}\right)\left(\frac{\partial \rho}{\partial Y_e}\right)_{s,p} + \left(\frac{\partial s}{\partial Y_e}\right)\right) = \\ &\frac{1}{\left(\frac{\partial p}{\partial T}\right)}\left(\left(\frac{\partial p}{\partial \rho}\right)\left(\frac{\partial \rho}{\partial Y_e}\right)_{s,p} + \left(\frac{\partial p}{\partial Y_e}\right)\right) \end{aligned} \tag{B.9}$$

where the constraints on the partial derivatives in the natural variables have been omitted for brevity (i.e. $(\partial s/\partial T) \equiv (\partial s/\partial T)_{\rho,Y_e}$). We just have to solve for $(\partial\rho/\partial Y_e)_{s,p}$, resulting in

$$\left(\frac{\partial \rho}{\partial Y_e}\right)_{s,p} = \frac{\frac{(\partial p/\partial Y_e)}{(\partial p/\partial T)} - \frac{(\partial s/\partial Y_e)}{(\partial s/\partial T)}}{\frac{(\partial s/\partial \rho)}{(\partial s/\partial T)} - \frac{(\partial p/\partial \rho)}{(\partial p/\partial T)}} \tag{B.10}$$

B.3 Using the speed of sound / adiabatic index

The Ledoux criterion can also be expressed in simple radial gradients of the primitive variables and the local speed of sound by

$$C_{\mathrm{led}} = \frac{\mathrm{d}\rho}{\mathrm{d}r} - \frac{1}{c_s^2}\frac{\mathrm{d}p}{\mathrm{d}r}, \tag{B.11}$$

with the speed of sound as

$$c_s = \sqrt{\Gamma \frac{p}{\rho}}, \tag{B.12}$$

and there, the adiabatic index

$$\Gamma = \left(\frac{\partial \log p}{\partial \log \rho}\right)_{s,Y_e} = \frac{\rho}{p}\left(\frac{\partial p}{\partial \rho}\right)_{s,Y_e}. \tag{B.13}$$

This is very convenient, as the derivatives in the primitive variables ρ and p can be directly evaluated in our code and c_s is already tabulated in all EoS we use.

A derivation of Eq. (B.11) follows. Using (B.12) and (B.13) the right hand side becomes

$$\frac{\mathrm{d}\rho}{\mathrm{d}r} - \left(\frac{\partial \rho}{\partial p}\right)_{s,Y_e} \frac{\mathrm{d}p}{\mathrm{d}r} \tag{B.14}$$

The radial gradient of p can be rewritten as

$$\frac{\mathrm{d}p}{\mathrm{d}r} = \left(\frac{\partial p}{\partial s}\right)_{\rho,Y_e} \frac{\mathrm{d}s}{\mathrm{d}r} + \left(\frac{\partial p}{\partial \rho}\right)_{s,Y_e} \frac{\mathrm{d}\rho}{\mathrm{d}r} + \left(\frac{\partial p}{\partial Y_e}\right)_{s,\rho} \frac{\mathrm{d}Y_e}{\mathrm{d}r}. \tag{B.15}$$

Inserting into (B.14) yields

$$-\left(\frac{\partial \rho}{\partial p}\right)_{s,Y_e} \left(\frac{\partial p}{\partial s}\right)_{\rho,Y_e} \frac{\mathrm{d}s}{\mathrm{d}r} - \left(\frac{\partial \rho}{\partial p}\right)_{s,Y_e} \left(\frac{\partial p}{\partial Y_e}\right)_{s,\rho} \frac{\mathrm{d}Y_e}{\mathrm{d}r}. \tag{B.16}$$

Using the triple product rule,

$$\left(\frac{\partial x}{\partial y}\right)_z \left(\frac{\partial y}{\partial z}\right)_x \left(\frac{\partial z}{\partial x}\right)_y = -1, \tag{B.17}$$

we recover the right hand side of Eq. (B.1),

$$\left(\frac{\partial \rho}{\partial s}\right)_{Y,p} \frac{\mathrm{d}s}{\mathrm{d}r} + \left(\frac{\partial \rho}{\partial Y}\right)_{s,p} \frac{\mathrm{d}Y}{\mathrm{d}r} \tag{B.18}$$

Bibliography

Abramowitz, M., Stegun, I. A., editors (**1970**). *Handbook Of Mathematical Functions.* U.S. Department of Commerce. Unaltered, unabridged republication of #55, National Bureau of Standards - Applied Mathematics Series (1964), corrected edition. ISBN 0-486-61272-4.

Antoniadis, J., Freire, P. C. C., Wex, N., Tauris, T. M., Lynch, R. S., van Kerkwijk, M. H., Kramer, M., Bassa, C., Dhillon, V. S., Driebe, T., Hessels, J. W. T., Kaspi, V. M., Kondratiev, V. I., Langer, N., Marsh, T. R., McLaughlin, M. A., Pennucci, T. T., Ransom, S. M., Stairs, I. H., van Leeuwen, J., Verbiest, J. P. W., Whelan, D. G. (**2013**). A Massive Pulsar in a Compact Relativistic Binary. *Science*, volume 340, p. 448. doi:10.1126/science.1233232.

Arnett, W. D., Bahcall, J. N., Kirshner, R. P., Woosley, S. E. (**1989**). Supernova 1987A. *Annual Review of Astronomy and Astrophysics*, volume 27, pp. 629–700. doi:10.1146/annurev.aa.27.090189.003213.

Baade, W., Zwicky, F. (**1934**). Remarks on super-novae and cosmic rays. *Phys. Rev.*, volume 46(1), pp. 76–77. doi:10.1103/PhysRev.46.76.2.

Baumgarte, T. W., Janka, H.-T., Keil, W., Shapiro, S. L., Teukolsky, S. A. (**1996a**). Delayed Collapse of Hot Neutron Stars to Black Holes via Hadronic Phase Transitions. *The Astrophysical Journal*, volume 468, p. 823. doi:10.1086/177738.

Baumgarte, T. W., Shapiro, S. L., Teukolsky, S. A. (**1996b**). Computing the Delayed Collapse of Hot Neutron Stars to Black Holes. *The Astrophysical Journal*, volume 458, p. 680. doi:10.1086/176849.

Beacom, J. F. (**2010**). The Diffuse Supernova Neutrino Background. *Annual Review of Nuclear and Particle Science*, volume 60, pp. 439–462. doi:10.1146/annurev.nucl.010909.083331.

Beacom, J. F., Boyd, R. N., Mezzacappa, A. (**2001**). Black hole formation in core-collapse supernovae and time-of-flight measurements of the neutrino masses. *Phys. Rev. D*, volume 63, p. 073011. doi:10.1103/PhysRevD.63.073011.

Bethe, H. A. (**1990**). Supernova mechanisms. *Reviews of Modern Physics*, volume 62, pp. 801–866.

Bruenn, S. W. (**1985**). Stellar core collapse – numerical model and infall epoch. *The Astrophysical Journal Supplement Series*, volume 58, pp. 771–841. doi:10.1086/191056.

Bruenn, S. W., Dineva, T. (**1996**). The Role of Doubly Diffusive Instabilities in the Core-Collapse Supernova Mechanism. *The Astrophysical Journal Letters*, volume 458, pp. L71+. doi:10.1086/309921.

Bruenn, S. W., Mezzacappa, A. (**1997**). Ion screening effects and stellar collapse. *Physical Review D*, volume 56, pp. 7529–7547. doi:10.1103/PhysRevD.56.7529.

Bruenn, S. W., Raley, E. A., Mezzacappa, A. (**2004**). Fluid Stability Below the Neutrinospheres of Supernova Progenitors and the Dominant Role of Lepto-Entropy Fingers. *arXiv:astro-ph/0404099*.

Buras, R., Janka, H.-T., Keil, M. T., Raffelt, G. G., Rampp, M. (**2003a**). Electron neutrino pair annihilation: A new source for muon and tau neutrinos in supernovae. *The Astrophysical Journal*, volume 587, pp. 320–326. doi:10.1086/368015.

Buras, R., Rampp, M., Janka, H.-T., Kifonidis, K. (**2003b**). Improved Models of Stellar Core Collapse and Still No Explosions: What Is Missing? *Physical Review Letters*, volume 90(24), pp. 241101–+. doi:10.1103/PhysRevLett.90.241101.

Buras, R., Janka, H.-T., Rampp, M., Kifonidis, K. (**2006a**). Two-dimensional hydrodynamic core-collapse supernova simulations with spectral neutrino transport. II. Models for different progenitor stars. *Astronomy & Astrophysics*, volume 457, pp. 281–308. doi:10.1051/0004-6361:20054654.

Buras, R., Rampp, M., Janka, H.-T., Kifonidis, K. (**2006b**). Two-dimensional hydrodynamic core-collapse supernova simulations with spectral neutrino transport. I. Numerical method and results for a 15 $M_\odot$ star. *Astronomy & Astrophysics*, volume 447, pp. 1049–1092. doi:10.1051/0004-6361:20053783.

Burrows, A., Fryxell, B. A. (**1992**). An instability in neutron stars at birth. *Science*, volume 258, pp. 430–434. doi:10.1126/science.258.5081.430.

Burrows, A., Fryxell, B. A. (**1993**). A Convective Trigger for Supernova Explosions. *The Astrophysical Journal Letters*, volume 418, p. L33. doi:10.1086/187109.

Burrows, A., Lattimer, J. M. (**1986**). The birth of neutron stars. *The Astrophysical Journal*, volume 307, pp. 178–196. doi:10.1086/164405.

Burrows, A., Sawyer, R. F. (**1998**). Effects of correlations on neutrino opacities in nuclear matter. *Physical Review C*, volume 58, pp. 554–571. doi:10.1103/PhysRevC.58.554.

Burrows, A., Sawyer, R. F. (**1999**). Many–body corrections to charged–current neutrino absorption rates in nuclear matter. *Physical Review C*, volume 59, pp. 510–514. doi:10.1103/PhysRevC.59.510.

Burrows, A., Mazurek, T. J., Lattimer, J. M. (**1981**). The deleptonization and heating of proton-neutron stars. *The Astrophysical Journal*, volume 251, pp. 325–336. doi:10.1086/159467.

Carter, G. W., Prakash, M. (**2002**). The quenching of the axial coupling in nuclear and neutron-star matter. *Physics Letters B*, volume 525, pp. 249–254. doi:10.1016/S0370-2693(01)01452-6.

Cernohorsky, J. (**1994**). Symmetries in neutrino-electron scattering. *The Astrophysical Journal*, volume 433, pp. 247–249. doi:10.1086/174639.

Chadwick, J. (**1932**). Possible Existence of a Neutron. *Nature*, volume 129, pp. 312–+. doi:10.1038/129312a0.

Colella, P., Woodward, P. R. (**1984**). The Piecewise Parabolic Method (PPM) for Gas-Dynamical Simulations. *Journal of Computational Physics*, volume 54, pp. 174–201. doi:10.1016/0021-9991(84)90143-8.

Colgate, S. A., White, R. H. (**1966**). The Hydrodynamic Behavior of Supernovae Explosions. *The Astrophysical Journal*, volume 143, pp. 626–+.

Dasgupta, B., Dighe, A., Raffelt, G. G., Smirnov, A. Y. (**2009**). Multiple Spectral Splits of Supernova Neutrinos. *Physical Review Letters*, volume 103(5), 051105. doi:10.1103/PhysRevLett.103.051105.

Demorest, P. B., Pennucci, T., Ransom, S. M., Roberts, M. S. E., Hessels, J. W. T. (**2010**). A two-solar-mass neutron star measured using Shapiro delay. *Nature*, volume 467, pp. 1081–1083. doi:10.1038/nature09466.

Duan, H., Fuller, G. M., Qian, Y.-Z. (**2010**). Collective Neutrino Oscillations. *Annual Review of Nuclear and Particle Science*, volume 60, pp. 569–594. doi:10.1146/annurev.nucl.012809.104524.

Fischer, T., Liebendörfer, M., Mezzacappa, A. (**2007**). The expected neutrino signal from the formation of black holes via protoneutron star collapse. *Journal of Physics Conference Series*, volume 66(1), 012043. doi:10.1088/1742-6596/66/1/012043.

Fischer, T., Whitehouse, S. C., Mezzacappa, A., Thielemann, F.-K., Liebendörfer, M. (**2009**). The neutrino signal from protoneutron star accretion and black hole formation. *Astronomy & Astrophysics*, volume 499, pp. 1–15. doi:10.1051/0004-6361/200811055.

Fischer, T., Whitehouse, S. C., Mezzacappa, A., Thielemann, F., Liebendörfer, M. (**2010**). Protoneutron star evolution and the neutrino-driven wind in general relativistic neutrino radiation hydrodynamics simulations. *Astronomy & Astrophysics*, volume 517, pp. A80+. doi:10.1051/0004-6361/200913106.

Fryer, C. L., Warren, M. S. (**2002**). Modeling Core–Collapse Supernovae in Three Dimensions. *The Astrophysical Journal Letters*, volume 574, pp. L65–L68. doi:10.1086/342258.

Fryxell, B., Müller, E., Arnett, W. (**1989**). Hydrodynamics and nuclear burning. preprint MPA–449, Max Planck Institut für Astrophysik, Garching.

Fryxell, B., Olson, K., Ricker, P., Timmes, F. X., Zingale, M., Lamb, D. Q., MacNeice, P., Rosner, R., Truran, J. W., Tufo, H. (**2000**). FLASH: An Adaptive Mesh Hydrodynamics Code for Modeling Astrophysical Thermonuclear Flashes. *The Astrophysical Journal Supplement Series*, volume 131, pp. 273–334. doi:10.1086/317361.

Fuller, G. M., Meyer, B. S. (**1995**). Neutrino Capture and Supernova Nucleosynthesis. *The Astrophysical Journal*, volume 453, p. 792. doi:10.1086/176442.

Hannestad, S., Raffelt, G. (**1998**). Supernova neutrino opacity from nucleon–nucleon bremsstrahlung and related processes. *The Astrophysical Journal*, volume 507, pp. 339–352. doi:10.1086/306303.

Herant, M., Benz, W., Hix, W. R., Fryer, C. L., Colgate, S. A. (**1994**). Inside the supernova: A powerful convective engine. *The Astrophysical Journal*, volume 435, pp. 339–361. doi:10.1086/174817.

Hewish, A., Bell, S. J., Pilkington, J. D. H., Scott, P. F., Collins, R. A. (**1968**). Observation of a Rapidly Pulsating Radio Source. *Nature*, volume 217, pp. 709–713. doi:10.1038/217709a0.

Horowitz, C. J. (**1997**). Neutrino trapping in a supernova and the screening of weak neutral currents. *Physical Review D*, volume 55, pp. 4577–4581. doi:10.1103/PhysRevD.55.4577.

Horowitz, C. J. (**2002**). Weak magnetism for antineutrinos in supernovae. *Physical Review D*, volume 65(4), pp. 043001–+. doi:10.1103/PhysRevD.65.043001.

Horowitz, C. J., Li, G. (**1999**). Nucleosynthesis in supernovae. *Phys. Rev. Lett.*, volume 82(26), pp. 5198–5201. doi:10.1103/PhysRevLett.82.5198.

Hüdepohl, L., Müller, B., Janka, H., Marek, A., Raffelt, G. G. (**2010**). Neutrino Signal of Electron-Capture Supernovae from Core Collapse to Cooling. *Physical Review Letters*, volume 104(25), pp. 251101–+. doi:10.1103/PhysRevLett.104.251101.

Janka, H.-T. (**1999**). unpublished.

Janka, H.-T., Hillebrandt, W. (**1989**). Neutrino Emission from Type II Supernovae - an Analysis of the Spectra. *Astronomy & Astrophysics*, volume 224, pp. 49–56.

Janka, H.-T., Müller, E. (**1996**). Neutrino heating, convection, and the mechanism of Type–II supernova explosions. *Astronomy & Astrophysics*, volume 306, pp. 167–+.

Janka, H.-T., Hanke, F., Hüdepohl, L., Marek, A., Müller, B., Obergaulinger, M. (**2012**). Core-collapse supernovae: Reflections and directions. *Progress of Theoretical and Experimental Physics*, volume 2012(1), 01A309. doi:10.1093/ptep/pts067.

Keil, M. T., Raffelt, G. G., Janka, H.-T. (**2003**). Monte Carlo Study of Supernova Neutrino Spectra Formation. *The Astrophysical Journal*, volume 590, pp. 971–991. doi:10.1086/375130.

Keil, W. (**1997**). *Konvektive Instabilitäten in entstehenden Neutronensternen*. Ph.D. thesis, Technische Universität München.

Keil, W., Janka, H. (**1995**). Hadronic phase transitions at supranuclear densities and the delayed collapse of newly formed neutron stars. *Astronomy & Astrophysics*, volume 296, pp. 145–+.

Keil, W., Janka, H.-T., Raffelt, G. (**1995**). Reduced neutrino opacities and the SN 1987A signal. *Physical Review D*, volume 51, pp. 6635–6646. doi:10.1103/PhysRevD.51.6635.

Keil, W., Janka, H.-T., Mueller, E. (**1996**). Ledoux Convection in Protoneutron Stars—A Clue to Supernova Nucleosynthesis? *The Astrophysical Journal Letters*, volume 473, pp. L111+. doi:10.1086/310404.

Kifonidis, K., Plewa, T., Janka, H.-T., Müller, E. (**2003**). Non–spherical core collapse supernovae. I. Neutrino–driven convection, Rayleigh–Taylor instabilities, and the formation and propagation of metal clumps. *Astronomy & Astrophysics*, volume 408, pp. 621–649. doi:10.1051/0004-6361:20030863.

Langanke, K., Martínez–Pinedo, G., Sampaio, J. M., Dean, D. J., Hix, W. R., Messer, O. E., Mezzacappa, A., Liebendörfer, M., Janka, H.-T., Rampp, M. (**2003**). Electron capture rates on nuclei and implications for stellar core collapse. *Physical Review Letters*, volume 90(24), pp. 241102–+. doi:10.1103/PhysRevLett.90.241102.

Langanke, K., Martínez-Pinedo, G., Müller, B., Janka, H.-T., Marek, A., Hix, W. R., Juodagalvis, A., Sampaio, J. M. (**2008**). Effects of Inelastic Neutrino-Nucleus Scattering on Supernova Dynamics and Radiated Neutrino Spectra. *Physical Review Letters*, volume 100(1), pp. 011101–+. doi:10.1103/PhysRevLett.100.011101.

Lattimer, J. M. (**2006**). Constraints on the Dense Matter Equation of State from Observations. In *American Institute of Physics Conference Series*, pp. 155–162. doi:10.1063/1.2234397.

Lattimer, J. M., Prakash, M. (**2007**). Neutron star observations: Prognosis for equation of state constraints. *Physics Reports*, volume 442, pp. 109–165. doi:10.1016/j.physrep.2007.02.003.

Lattimer, J. M., Swesty, F. D. (**1991**). A generalized equation of state for hot, dense matter. *Nuclear Physics A*, volume 535, pp. 331–376. doi:10.1016/0375-9474(91)90452-C.

Lattimer, J. M., Pethick, C. J., Ravenhall, D. G., Lamb, D. Q. (**1985**). Physical properties of hot, dense matter: The general case. *Nuclear Physics A*, volume 432, pp. 646–742. doi:10.1016/0375-9474(85)90006-5.

Liebendörfer, M., Messer, O. E. B., Mezzacappa, A., Bruenn, S. W., Cardall, C. Y., Thielemann, F.-K. (**2004**). A Finite Difference Representation of Neutrino Radiation Hydrodynamics in Spherically Symmetric General Relativistic Space-time. *The Astrophysical Journal Supplement Series*, volume 150, pp. 263–316. doi:10.1086/380191.

Liebendörfer, M., Rampp, M., Janka, H.-T., Mezzacappa, A. (**2005**). Supernova Simulations with Boltzmann Neutrino Transport: A Comparison of Methods. *The Astrophysical Journal*, volume 620, pp. 840–860. doi:10.1086/427203.

Malek, M., Morii, M., Fukuda, S., Fukuda, Y., Ishitsuka, M., Itow, Y., Kajita, T., Kameda, J., Kaneyuki, K., Kobayashi, K., Koshio, Y., Miura, M., Moriyama, S., Nakahata, M., Nakayama, S., Namba, T., Okada, A., Ooyabu, T., Saji, C., Sakurai, N., Shiozawa, M., Suzuki, Y., Takeuchi, H., Takeuchi, Y., Totsuka, Y., Yamada, S., Desai, S., Earl, M., Kearns, E., Messier, M. D., Stone, J. L., Sulak, L. R., Walter, C. W., Goldhaber, M., Barszczak, T., Casper, D., Gajewski, W., Kropp, W. R., Mine, S., Liu, D. W., Smy, M. B., Sobel, H. W., Vagins, M. R., Gago, A., Ganezer, K. S., Keig, W. E., Ellsworth, R. W., Tasaka, S., Kibayashi, A., Learned, J. G., Matsuno, S., Takemori, D., Hayato, Y., Ishii, T., Kobayashi, T., Maruyama, T., Nakamura, K., Obayashi, Y., Oyama, Y., Sakuda, M., Yoshida, M., Kohama, M., Iwashita, T., Suzuki, A. T., Ichikawa, A., Inagaki, T., Kato, I., Nakaya, T., Nishikawa, K., Haines, T. J., Dazeley, S., Hatakeyama, S., Svoboda, R., Blaufuss, E., Goodman, J. A., Guillian, G., Sullivan, G. W., Turcan, D., Scholberg, K., Habig, A., Ackermann, M., Hill, J., Jung, C. K., Martens, K., Mauger, C., McGrew, C., Sharkey, E., Viren, B., Yanagisawa, C., Toshito, T., Mitsuda, C., Miyano, K., Shibata, T., Kajiyama, Y., Nagashima, Y., Nitta, K., Takita, M., Kim, H. I., Kim, S. B., Yoo, J., Okazawa, H., Ishizuka, T., Etoh, M., Gando, Y., Hasegawa, T., Inoue, K., Ishihara, K., Shirai, J., Suzuki, A., Koshiba, M., Hatakeyama, Y., Ichikawa, Y., Koike, M., Nishijima, K., Ishino, H., Nishimura, R., Watanabe, Y., Kielczewska, D., Berns, H. G., Boyd, S. C., Stachyra, A. L., Wilkes, R. J. (**2003**). Search for Supernova Relic Neutrinos at Super-Kamiokande. *Physical Review Letters*, volume 90(6), 061101. doi:10.1103/PhysRevLett.90.061101.

Marek, A. (**2007**). *Multi-dimensional simulations of core-collapse supernovae with different equations of state for hot proto-neutron stars*. Ph.D. thesis, Technische Universität München. `http://nbn-resolving.de/urn/resolver.pl?urn:nbn:de:bvb:91-diss-20070424-604499-0-1`.

Marek, A., Janka, H.-T. (**2009**). Delayed Neutrino-Driven Supernova Explosions Aided by the Standing Accretion-Shock Instability. *The Astrophysical Journal*, volume 694, pp. 664–696. doi:10.1088/0004-637X/694/1/664.

Marek, A., Dimmelmeier, H., Janka, H.-T., Müller, E., Buras, R. (**2006**). Exploring the relativistic regime with newtonian hydrodynamics: an improved effective gravitational potential for supernova simulations. *Astronomy & Astrophysics*, volume 445, pp. 273–289. doi:10.1051/0004-6361:20052840.

Marek, A., Janka, H.-T., Müller, E. (**2009**). Equation-of-state dependent features in shock-oscillation modulated neutrino and gravitational-wave signals from supernovae. *Astronomy & Astrophysics*, volume 496, pp. 475–494. doi:10.1051/0004-6361/200810883.

Martínez-Pinedo, G., Fischer, T., Lohs, A., Huther, L. (**2012**). Charged-Current Weak Interaction Processes in Hot and Dense Matter and its Impact on the Spectra of Neutrinos Emitted from Protoneutron Star Cooling. *Physical Review Letters*, volume 109(25), 251104. doi:10.1103/PhysRevLett.109.251104.

Mayle, R., Wilson, J. R. (**1988**). Supernovae from collapse of oxygen-magnesium-neon cores. *The Astrophysical Journal*, volume 334, pp. 909–926. doi:10.1086/166886.

Menéndez, J., Gazit, D., Schwenk, A. (**2011**). Chiral Two-Body Currents in Nuclei: Gamow-Teller Transitions and Neutrinoless Double-Beta Decay. *Physical Review Letters*, volume 107(6), 062501. doi:10.1103/PhysRevLett.107.062501.

Mezzacappa, A., Bruenn, S. W. (**1993a**). Stellar core collapse – a boltzmann treatment of neutrino–electron scattering. *The Astrophysical Journal*, volume 410, pp. 740–760. doi:10.1086/172791.

Mezzacappa, A., Bruenn, S. W. (**1993b**). Type II supernovae and Boltzmann neutrino transport - The infall phase. *The Astrophysical Journal*, volume 405, pp. 637–668. doi:10.1086/172394.

Müller, E., Janka, H.-T. (**1994**). Multi-Dimensional Simulations of Neutrino-Driven Supernovae. In G. Klare, editor, *Reviews in Modern Astronomy*, volume 7 of *Reviews in Modern Astronomy*, pp. 103–128.

Müller, B. (**2009**). *Multi-Dimensional Relativistic Simulations of Core-Collapse Supernovae with Energy-Dependent Neutrino Transport*. Ph.D. thesis, Technische Universität München. `http://nbn-resolving.de/urn/resolver.pl?urn:nbn:de:bvb:91-diss-20090519-800389-1-1`.

Nakazato, K., Sumiyoshi, K., Suzuki, H., Yamada, S. (**2008**). Oscillation and future detection of failed supernova neutrinos from a black-hole-forming collapse. *Physical Review D*, volume 78(8), 083014. doi:10.1103/PhysRevD.78.083014.

Nakazato, K., Sumiyoshi, K., Suzuki, H., Yamada, S. (**2009**). Erratum: Oscillation and future detection of failed supernova neutrinos from a black-hole-forming collapse [Phys. Rev. D 78, 083014 (2008)]. *Physical Review D*, volume 79(6), 069901. doi:10.1103/PhysRevD.79.069901.

O'Connor, E., Ott, C. D. (**2011**). Black Hole Formation in Failing Core-Collapse Supernovae. *The Astrophysical Journal*, volume 730, 70. doi:10.1088/0004-637X/730/2/70.

O'Connor, E., Ott, C. D. (**2013**). The Progenitor Dependence of the Pre-explosion Neutrino Emission in Core-collapse Supernovae. *The Astrophysical Journal*, volume 762, 126. doi:10.1088/0004-637X/762/2/126.

Pons, J. A., Miralles, J. A., Ibanez, J. M. A. (**1998**). Legendre expansion of the $\nu\bar{\nu} \rightleftharpoons e^+e^-$ kernel: Influence of high order terms. *Astronomy & Astrophysics Supplement*, volume 129, pp. 343–351. doi:10.1051/aas:1998189.

Pons, J. A., Reddy, S., Prakash, M., Lattimer, J. M., Miralles, J. A. (**1999**). Evolution of Proto-Neutron Stars. *The Astrophysical Journal*, volume 513, pp. 780–804. doi:10.1086/306889.

Pons, J. A., Steiner, A. W., Prakash, M., Lattimer, J. M. (**2001**). Evolution of Proto-Neutron Stars with Quarks. *Physical Review Letters*, volume 86, pp. 5223–5226. doi:10.1103/PhysRevLett.86.5223.

Qian, Y.-Z., Woosley, S. E. (**1996**). Nucleosynthesis in Neutrino-Driven Winds. I. The Physical Conditions. *The Astrophysical Journal*, volume 471(1), pp. 331–351. doi:10.1086/177973.

Raffelt, G. (**2001**). Mu- and tau-neutrino spectra formation in supernovae. *The Astrophysical Journal*, volume 561(2), pp. 890–914. doi:10.1086/323379.

Rampp, M., Janka, H.-T. (**2002**). Radiation hydrodynamics with neutrinos. variable eddington factor method for core–collapse supernova simulations. *Astronomy & Astrophysics*, volume 396, pp. 361–392. doi:10.1051/0004-6361:20021398.

Reddy, S., Prakash, M., Lattimer, J. M. (**1998**). Neutrino interactions in hot and dense matter. *Physical Review D*, volume 58(1), pp. 013009–+. doi:10.1103/PhysRevD.58.013009.

Reddy, S., Prakash, M., Lattimer, J. M., Pons, J. A. (**1999**). Effects of strong and electromagnetic correlations on neutrino interactions in dense matter. *Physical Review C*, volume 59, pp. 2888–2918. doi:10.1103/PhysRevC.59.2888.

Roberts, L. (**2012c**). Neutrino interactions near the neutrino sphere in proto neutron stars, `http://stellarcollapse.org/media/micra2013/Luke_Roberts.pdf`. In *MICRA 2013 – Microphysics in Computational Relativistic Astrophysics*.

Roberts, L. F. (**2012**). A New Code for Proto-neutron Star Evolution. *The Astrophysical Journal*, volume 755, 126. doi:10.1088/0004-637X/755/2/126.

Roberts, L. F., Reddy, S., Shen, G. (**2012a**). Medium modification of the charged-current neutrino opacity and its implications. *Physical Review C*, volume 86(6), 065803. doi:10.1103/PhysRevC.86.065803.

Roberts, L. F., Shen, G., Cirigliano, V., Pons, J. A., Reddy, S., Woosley, S. E. (**2012b**). Protoneutron Star Cooling with Convection: The Effect of the Symmetry Energy. *Physical Review Letters*, volume 108(6), 061103. doi:10.1103/PhysRevLett.108.061103.

Sarikas, S., Raffelt, G. G., Hüdepohl, L., Janka, H.-T. (**2012a**). Suppression of self-induced flavor conversion in the supernova accretion phase. *Phys. Rev. Lett.*, volume 108, p. 061101. doi:10.1103/PhysRevLett.108.061101.

Sarikas, S., Tamborra, I., Raffelt, G., Hüdepohl, L., Janka, H.-T. (**2012b**). Supernova neutrino halo and the suppression of self-induced flavor conversion. *Phys. Rev. D*, volume 85(11), 113007. doi:10.1103/PhysRevD.85.113007.

Serpico, P. D., Chakraborty, S., Fischer, T., Hüdepohl, L., Janka, H.-T., Mirizzi, A. (**2012**). Probing the neutrino mass hierarchy with the rise time of a supernova burst. *Phys. Rev. D*, volume 85(8), 085031. doi:10.1103/PhysRevD.85.085031.

Shen, H., Toki, H., Oyamatsu, K., Sumiyoshi, K. (**1998a**). Relativistic equation of state of nuclear matter for supernova and neutron star. *Nucl. Phys. A*, volume 637, pp. 435–450. doi:10.1016/S0375-9474(98)00236-X.

Shen, H., Toki, H., Oyamatsu, K., Sumiyoshi, K. (**1998b**). Relativistic equation of state of nuclear matter for supernova explosion. *Progress of Theoretical Physics*, volume 100, pp. 1013–1031. doi:10.1143/PTP.100.1013.

Shen, H., Toki, H., Oyamatsu, K., Sumiyoshi, K. (**2011**). Relativistic Equation of State for Core-collapse Supernova Simulations. *The Astrophysical Journal Supplement Series*, volume 197, 20. doi:10.1088/0067-0049/197/2/20.

Steiner, A. W., Hempel, M., Fischer, T. (**2013**). Core-collapse Supernova Equations of State Based on Neutron Star Observations. *The Astrophysical Journal*, volume 774, 17. doi:10.1088/0004-637X/774/1/17.

Sumiyoshi, K., Yamada, S., Suzuki, H. (**2007**). Dynamics and Neutrino Signal of Black Hole Formation in Nonrotating Failed Supernovae. I. Equation of State Dependence. *The Astrophysical Journal*, volume 667, pp. 382–394. doi:10.1086/520876.

Sumiyoshi, K., Yamada, S., Suzuki, H. (**2008**). Dynamics and Neutrino Signal of Black Hole Formation in Nonrotating Failed Supernovae. II. Progenitor Dependence. *The Astrophysical Journal*, volume 688, pp. 1176–1185. doi:10.1086/592183.

Ugliano, M., Janka, H.-T., Marek, A., Arcones, A. (**2012**). Progenitor-explosion Connection and Remnant Birth Masses for Neutrino-driven Supernovae of Iron-core Progenitors. *The Astrophysical Journal*, volume 757, 69. doi:10.1088/0004-637X/757/1/69.

Wilson, J. R. (**1971**). A Numerical Study of Gravitational Stellar Collapse. *The Astrophysical Journal*, volume 163, pp. 209–+. doi:10.1086/150759.

Wilson, J. R. (**1982**). Convection in core collapse supernovae. *in Proc. Univ. Illinois, Meeting on Numerical Astrophysiscs.*

Wilson, J. R., Mayle, R. (**1988**). Convection in core collapse supernovae. *Physics Reports*, volume 163, pp. 63–78. doi:10.1016/0370-1573(88)90036-1.

Wilson, J. R., Mayle, R. (**1993**). Report on the Progress of Supernova Research by the Livermore Group. *Physics Reports*, volume 227, pp. 97–111. doi:10.1016/0370-1573(93)90059-M.

Woosley, S. E., Weaver, T. A. (**1995**). The Evolution and Explosion of Massive Stars. II. Explosive Hydrodynamics and Nucleosynthesis. *The Astrophysical Journal Supplement Series*, volume 101, p. 181. doi:10.1086/192237.

Woosley, S. E., Wilson, J. R., Mathews, G. J., Hoffman, R. D., Meyer, B. S. (**1994**). The r-process and neutrino-heated supernova ejecta. *The Astrophysical Journal*, volume 433, pp. 229–246. doi:10.1086/174638.

Woosley, S. E., Heger, A., Weaver, T. A. (**2002**). The evolution and explosion of massive stars. *Reviews of Modern Physics*, volume 74, pp. 1015–1071. doi:10.1103/RevModPhys.74.1015.

Yang, L., Lunardini, C. (**2011**). Revealing local failed supernovae with neutrino telescopes. *Physical Review D*, volume 84(6), 063002. doi:10.1103/PhysRevD.84.063002.

Danksagung

Vielen Dank an Alle die diese Arbeit möglich gemacht haben!
Zuerst natürlich meinem Betreuer Hans-Thomas Janka, der mir die Möglichkeit gab an diesem spannenden Teil der Astrophysik zu forschen und sich immer Zeit für Diskussionen und Anregungen genommen hat.
Den anderen aus der Gruppe, besonders Andreas und Bernhard, tausend Dank für ihre Geduld mit mir und die aufmerksame und konstruktive Hilfe bei allen Arten von physikalischen oder technischen Problemen.
Vielen Dank auch den restlichen MPAlern, für ihre Freundlichkeit und ständige Hilfsbereitschaft.
Danke an Manos, mit dem mich besonders die gemeinsame Doktorarbeitszeit verbindet, für seine Nachsichtigkeit mit mir und die vielen gemeinsamen Abende aber auch Kaffeepausen.
Janina, Katharina und Andreas - tausend Dank für das Korrekturlesen, ich hab sicher noch genug Fehler in der Arbeit gelassen.
Meinen Eltern und meiner restlichen Familie für ihre Unterstützung und Rückhalt.
Ganz besonders aber Janina, ohne dich wären die Jahre meiner Doktorarbeit nicht so schön und unvergesslich gewesen. Schön, dass wir uns gefunden haben!